Politecnico di Torino

Department of Mechanical and Aerospace Engineering (DIMEAS)

Master's Degree in Aerospace Engineering

Preliminary stability analysis of a low-speed blended wing unmanned aerial vehicle

Supervisors:
Dr. Stefano Primatesta
Prof. Raffaello Mariani

Candidate:
Andrea Caramazza
292997

Academic year 2022-2023

Summary

Nowadays, environmentally friendly aviation is one of the most challenging topics in the aerospace world. Research about different approaches to improve aircraft efficiency explores every possible aspect of the design process, from particularly aerodynamically efficient shapes to hybrid propulsion systems, with the aim to achieve net-zero emissions in the near future. Green Raven is a student-focused research project of a technological demonstrator platform for a blended wing-body UAV powered via a hybrid/electric motor for sustainable aviation. In this thesis, the stability characteristics of the Green Raven are investigated in order to carry out an assessment of the flying qualities of the design.

The study consists of a series of wind tunnel tests, performed at the L2000 low-speed wind tunnel facility at KTH - Royal Institute of Technology, to gather the data needed to create an updated aerodynamic database of the UAV. A highlight on wind tunnel corrections is provided, regarding wall interference, blockage effects, and support corrections. Data obtained from the wind tunnel test is then corrected using a script developed in MATLAB and the corrected aerodynamics coefficients are obtained.

Acknowledgements

First and foremost, I want to thank Professor R. Mariani for believing in me and allowing me to KTH to work on this research. Furthermore, for the constant availability and support, as well as for the early conversations when the distance from Italy was felt the most. I want to thank Dr. S. Primatesta for his assistance and useful advice, which enabled me to be prepared for any problems that arose throughout my thesis.

Thanks to my father and mother for their unconditional love and constant support over the years, for allowing me to experience all that has shaped me into the person I am today. Thanks to my little sister, who manages to stay close to me despite the 1900 km distance between us.

Thanks to my Nachos, genuine friends on whom I can always rely, for the days of study and celebration throughout the years, and with whom I am confident I will enjoy many more.

Thanks to Davide, a thousand snowy adventures buddy and always ready for a drink of support in times of need. Thanks to Stefano, who has put up with me for over 20 years and with whom I share everything like a brother. Thanks to Andrea, a companion of soccer and other magical moments.

Thanks to Simone, Edoardo, Francesco, Cristiano, Anna, Francesco, Giuseppe, and all of my university friends with whom I shared uncountable hours of classes and study days to make my years at the Politecnico enjoyable.

Thanks to Francesca, Alessandro, Sara, Laura, and all the Intercultura friends with whom I experienced amazing times and realized how vital it is not to overlook the human aspect in each of us.

Thanks to Riccardo, Tommaso, Fatiha, the Francescos, Bea, Jordi, Javi, Leo, and all of the Swedish friends, for all the parties, barbecues, and amazing times we had.

Thanks to my flatmates Sam, Aigars, George, and Giannis for welcoming me like a member of the family, for always making me feel at home, and for their support during difficult times.

Thanks to Asja, for everything we've shared over the years, the good and the bad, for indelibly contributing to my growth, and for the affection that will always be there.

Finally, thanks to Pina, for making all the problems fade away when we are together.

Definition of Terms

Abbreviations

3D	Three dimenisonal
AOA	Angle of attack
BWB	Blended wing body
CAD	Computer-aided desing
CFD	Computational fluid dynamics
CG	Center of gravity
CNC	Computer numerical control
GR	Green Raven
MTOM	Maximum take-off mass
NP	Neutral point
PSP	Pressure sensitive paint
UAV	Unmanned aerial vehicle
WF	Weight fraction
WT	Winf tunnel

Symbols

α	Angle of attack
β	Sideslip angle
b	Wing span
c	Wing chord
C	Wind tunnel cross-section area
C_D	Drag coefficient
C_L	Lift coefficient
C_l	Rolling moment coefficient
C_m	Pitching moment coefficient
C_n	Yawing moment coefficient
C_Y	Side force coefficient
D	Drag
δ_s	Horizontal stabilizer deflection angle
δ	Boundary correction factor
δ_a	Aileron angle
δ_e	Elevator angle
δ_r	Elevator angle
E	Aerodynamic efficiency
ε_s	Solid blockage
ε_t	Total blockage
ε_{wb}	Wake blockage
K_1	Shape factor
M	Pitching moment
n	Yawing moment
l	Rolling moment
L	Lift
λ_3	Body shape factor
q	Dynamic pressure
ρ	Air density
R^2	Coefficient of determination
Re	Reynolds number
S	Wing surface
t	Body maximum thickness
τ_1	Tunnel shape factor
τ_2	Downwash correction factor
V	Volume
Y	Side force

Subscripts

0	at $\alpha = 0°$
α	Angle of attack derivative
β	Sideslip angle derivative
b	Body axis
bu	Buoyancy
c	Corrected value
CG	Center of gravity
g	Geometric
m	Model reference
u	Uncorrected value
up	Upflow
w	Wing; wind axis
x	Axial component in axis system
y	Lateral component in axis system
z	Normal component in axis system

Contents

List of Figures

List of Tables

Chapter 1

Introduction

1.1 Blendend wing body aircraft concept

The blended wing body (BWB) configuration is a promising concept that can provide an increase in aerodynamic efficiency with a consequent decrease in overall emissions. The BWB aircraft concept is a peculiar type of tailless aircraft, as it features an airfoil-shaped body and a fixed-wing configuration, having no clear separation between the fuselage and the wings, as they are smoothly blended as the name suggests. The lift is generated mostly by the body while the wings ensure the balance of the aircraft. This design has the main advantage of reduced drag compared to conventionally shaped aircraft, thanks to a smaller wetted area, and this means that increased fuel efficiency can be achieved. Countering all these benefits, the main reason why this kind of concept is not widely spread across civil aviation is the fact that the stability and control of this kind of aircraft are quite challenging to obtain. Other difficulties that arise are the fitting of pilots and passengers, as the body should be thick enough to accommodate the cabin and thus require a larger wing span to balance out.

One of the first research on this topic was carried out by Nicolas Woyevodsky in the early 1920s when based on his patent[1] the Westland Dreadnought was built but a crash on his first flight test promptly canceled the development of the project. In the following years, a few other attempts to develop a BWB aircraft were made but none of them presented satisfactory enough results. Recently these concept has regained a lot of interest as civil aviation is trying to comply with stricter emission regulations, in fact in 2021 the European Commission set the objective of reaching climate neutrality by 2050, with the intermediate target of at least 55% net reduction in greenhouse gas emissions by 2030 [2]. Among the major players in the aerospace industry, one of the most relevant examples of the potential of this technology is the concept developed by NASA and Boeing in the early 2000s with the Boeing X-48 UAV technology demonstrator, to establish a ground-to-flight database and prove the low-speed controllability of the concept throughout the flight envelope. The prototype, considering all the different variants that had been manufactured, flew a total of 122 flights, completing the flight test program in 2013 and proving the capability of a tailless aircraft to fly on the edge of the low-speed envelope safely [3]. Another example is the NASA N3-X concept aircraft, featuring

a BWB airframe and a fully turboelectric propulsion system, both characteristics to improve fuel economy, lower emission levels, and minimize noise levels over local communities. This concept is still in the early phase of the project, and studies have focused on understanding the flow around the body, the optimum geometry for the nacelles that have to accommodate the new propulsion system, and verifying the noise emissions of the aircraft [4][5][6][7].

1.2 The Green Raven project

To explore the potential of the BWB aircraft configuration for sustainable aviation, the Green Raven project started in 2020. The Green Raven is a student lead applied research, intending to design and build a BWB unmanned aerial vehicle (UAV) powered by a hybrid-electric hydrogen fuel cell. A conceptual design has been completed in 2022 [8] focusing on defining a simple mission and proceeding with the preliminary sizing of the aircraft and an aerodynamic analysis using CFD. The result of this analysis was a UAV with the reference specifications indicated in table 1.1. In figure 4.13 the geometry of the aircraft is illustrated.

Parameter	Value
MTOM	25 kg
Wing span	4 m
Cruise speed	20 m/s

Table 1.1: Green Raven specification

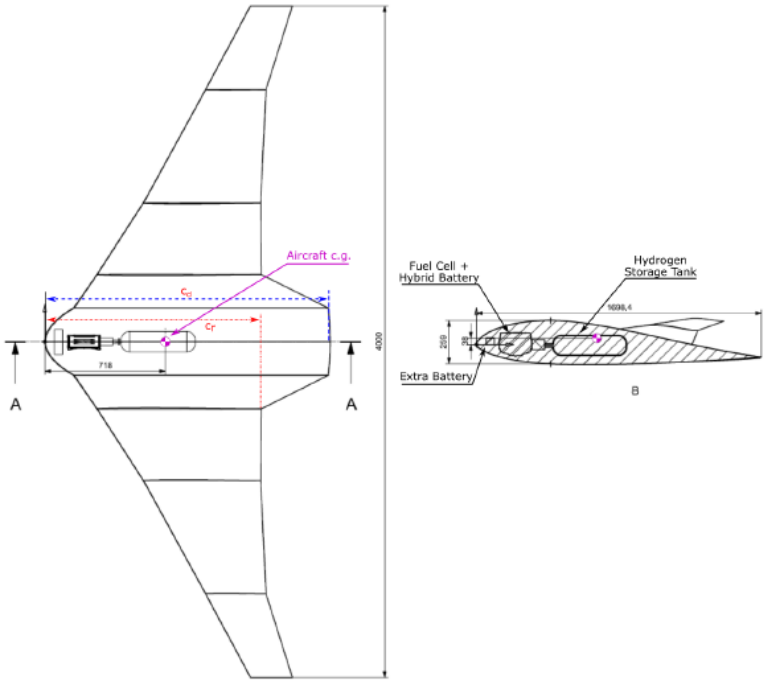

Figure 1.1: Green Raven reference geometry
[8]

Also, details on the power supply system were obtained, demonstrating that for a mission with a target duration of 60 minutes, a 650 W fuel cell with the addition of an 80g hydrogen tank and a 100 Wh lithium-ion battery were sufficient to complete the mission.

1.3 Thesis Outline

Chapter 4 highlights relevant literature about BWB aircraft and relative wind tunnel testing is included in order to point out what kind of results are to be expected from the tests on the Green Raven model. In chapter 2 and 3 a theoretical insight on aircraft stability and wind tunnel correction methodology is provided in order to introduce the main topics that are developed in this work. Chapter 5 contains details about the wind tunnel test setup, specifications of the model, and other relevant details on how the tests were carried out. In chapter 6 details on the raw data and correction applied following the methods described in chapter 3 is presented, along with the results obtained of the corrected coefficients. Also, a comparison between the performances and the effects of the different configurations tested is carried out in this chapter. Finally, in chapter 7, conclusions on the research completed and what possible future developments on the topic can be made are presented.

Chapter 2

Overview on aircraft stability

Studying the static and dynamic stability of an aircraft, as well as estimating its general flight quality plays a fundamental role throughout the development process of a new aircraft. In the earliest stages of the design, it leads to shaping a concept that can achieve adequate control performances and inherently stable characteristics. Later on in the development, these aspects are taken into account when considering compliance with regulatory requirements.

2.1 Static stability

The stability characteristics of an aircraft are usually broken down into parts: the longitudinal stability (symmetric portion), which consists of the motion in the xz plane and with leveled wings, and the lateral-directional stability (asymmetric portion) which considers the movement along the roll, pitch, and yaw axes of the aircraft at a constant elevation angle. This distinction between the two is considered in both static and dynamic analysis. Regarding static stability, however, the results of greatest importance of those associated with the longitudinal analysis [9].

2.1.1 Longitudinal stability

An aircraft is defined as inherently stable when it can recover to an initial condition after an external disturbance modifies its equilibrium state, without any forces being exerted on the body. In this case, the external disturbance can be a vertical gust that increases the angle of attack (AOA) and the response of a stable aircraft involves the generation of a nose-down pitching moment without any intervention from the pilot. Another important definition is that of stable flight, which identifies a flight condition where the resultant force and moment about the center of gravity (CG) are both zero, achieving longitudinal balance, and that requires the pitching moment to be zero. If the pitching moment didn't meet this requirement, the airplane would be subjected to rotational acceleration about the direction of the unbalanced moment.

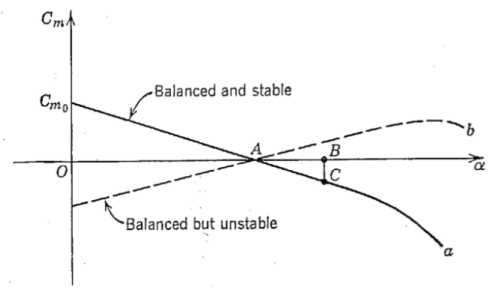

(a) Balanced aircraft

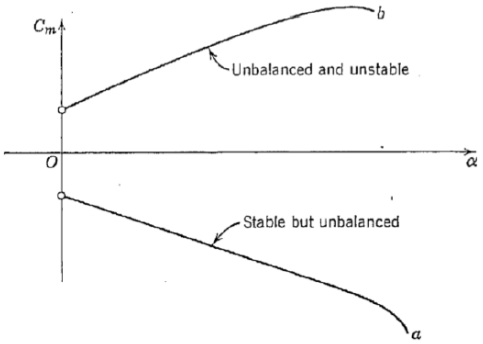

(b) Unbalanced airdraft

Figure 2.1: Pitching moment curves
[9]

From the static analysis, we obtain that to achieve longitudinal static stability the pitching moment variation with the AOA must be negative (positive stiffness), and therefore, to reach an equilibrium condition, the pitching moment at zero angle of attack must be positive.

$$C_{m_\alpha} < 0 \tag{2.1a}$$
$$C_{m_0} > 0 \tag{2.1b}$$

The coefficient in (2.1a) is also called pitch stiffness, and based on the signs of the coefficients in (2.1) we have four possible curves of pitching moment coefficient C_m versus the angle of attack α, as shown in figure 2.1. It's easy to understand that a design can be effective only if the pitching moment curve resembles that of figure 2.1a, in which the signs of C_{m_0} and C_{m_α} are opposite. There's also the possibility of flying an unstable aircraft equipped with an appropriate flight control system (FCS) to artificially stabilize it, but it's never possible to fly an unbalanced aircraft. Thus, the fundamental requirement that limits the aircraft design is to have an aircraft that is simultaneously stable and balanced [9].

Many different configurations with a positive C_{m_0} can achieve the required condition, since a proper choice of the CG location can ensure a negative $\frac{\partial C_m}{\partial \alpha}$, for a balanced and stable flight. In a straight flying-wing configuration, considering the C_{m_0} of conventional airfoil sections shown in figure 2.2, the wing camber would be the parameter that defines the stability characteristics as shown in table 2.1.

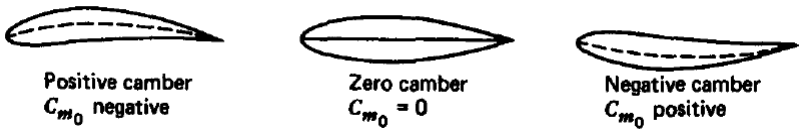

Figure 2.2: C_{m_0} of airfoils sections
[9]

Positive camber	flight not possible at any positive α or C_L
Zero camber	flight at $\alpha = 0$ or $C_L = 0$
Negative camber	flight at $\alpha > 0$ or $C_L > 0$

Table 2.1: Possible camber configurations for flying wings

It can be seen that only the negative camber profile allows for a stable and balanced flight. The same result can be achieved via a trailing edge flap deflected upwards on a symmetrical airfoil. Although the straight-wing tailless configuration is feasible, it's not in general use because the dynamic characteristics tend to be poor, drag and $C_{L_{max}}$ characteristics are not good and the possible CG range is too short. The solution to this problem can be achieved with two different configurations: the traditional wing-tail combination in figure 2.3 and the swept-back wing with twisted tips in figure 2.4.

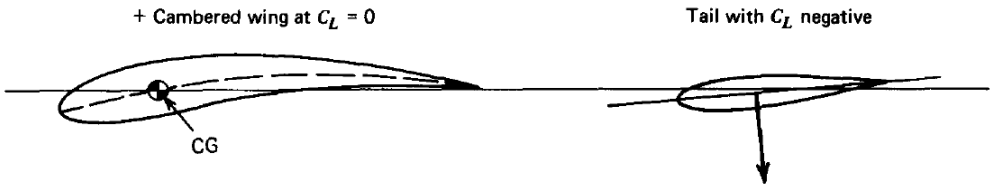

(a) Conventional arrangement

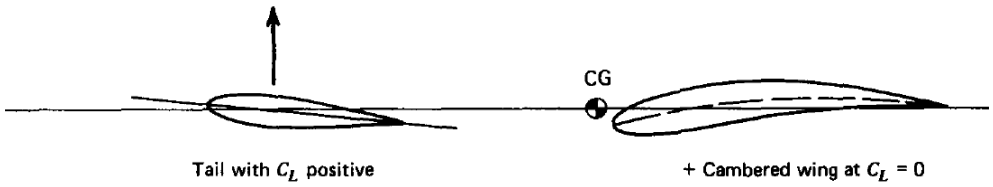

(b) Canard arrangement

Figure 2.3: Wing-tail configurations with positive C_{m_0}
[9]

- **Conventional wing-tail:** in this case, figure 2.3a, since a positive cambered airfoil possesses a negative moment about its aerodynamic center, the positive value of C_{m_0} is achieved with a tail set with a slightly negative incidence.
- **Canard arrangement:** alternatively in figure 2.3b, a small forewing with a positive incidence can be positioned in front of the positive cambered wing.

This particular configuration has the advantage that the small forewing, i.e. canard, produces lift in the same direction as the main wing, alleviating its total load.

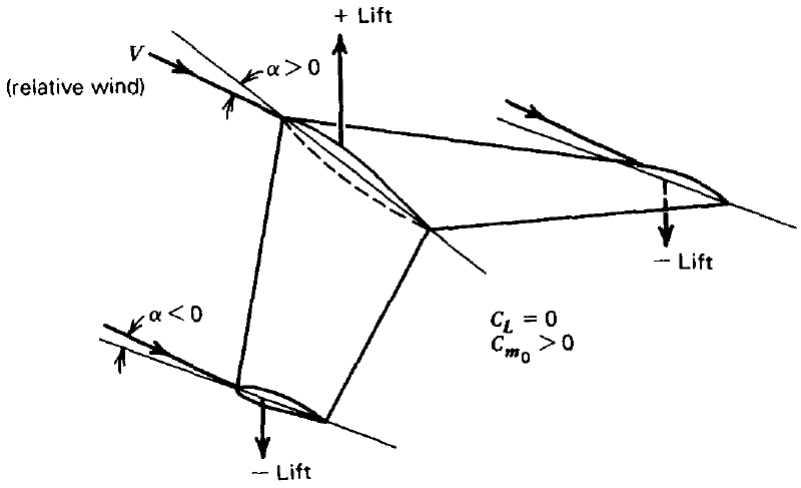

Figure 2.4: Swept back wing with twisted tips
[9]

- **Swept back wing:** in the case in figure 2.4, When the net lift of the wing is zero, its forward part has positive lift while the rear part negative. As a result, the desired positive couple is obtained, similar to the case of the conventional arrangement. An alternative to the swept-back wing is the delta wing.

The major task when performing a longitudinal static stability analysis is to determine the lift L and the pitching moment C_m of the model aircraft, in order to establish the position of the point at which the resultant lift is applied, called *neutral point*. Usually, to estimate lift and pitching moment, the total amount is obtained from the contributions of various parts of the aircraft, such as wing, body, tail, nacelles, and propulsive system. It's possible to consider the pitching moment about the aerodynamic center of a given surface invariant with α and therefore also the aerodynamic moment about that point is constant with α. Based on that consideration, it is possible to write the variation in pitching moment caused by a variation in α as in equation (2.2).

$$C_{m_\alpha} = -C_{L_\alpha}(h_n - h) \tag{2.2}$$

In this equation, the term in brackets indicates the dimensionless distance of the neutral point (NP) from the CG, and it's positive when the CG is in front of the NP. This term is also called static margin K, and it's usually indicated in percentage of the aerodynamic chord, and it's used as a measure of the static stability of the aircraft compared to α variations. It also gives information about

the margin of movement of the CG before reaching the stability limit. As stated before, a positive value of K indicates a stable aircraft, thus this characteristic is sought when designing a new aircraft, but if the static margin is too large while providing a very stable plane, it also causes a slow response to commands, hence reducing its maneuverability and making it more susceptible to control saturation.

2.1.2 Lateral-directional stability

Lateral-directional static stability refers to the aircraft's stability in both roll and yaw motion. When an aircraft experiences a disturbance that causes it to roll or yaw, its lateral-directional static stability determines how quickly it returns to its original roll and yaw attitude. Differently from the case of longitudinal stability, the velocity vector is now considered outside the plane of symmetry, hence the presence of yaw (β) and rolling (ϕ) displacements and the respective forces and moment coefficients C_l, C_m, C_n, respectively roll, pitch, and yaw.

The simplicity of studying the movement about a single axis (y) of the longitudinal problem is not present in this case, as here the rotation analyzed takes place around two different axis (x and z). The moments related to this rotation are cross-coupled, meaning that a roll rotation produces a yawing moment, as well as a rolling moment and a yaw displacement both produce rolling and yawing moments. Also, the roll and yaw controls are cross-coupled, meaning that a deflection of the rudder can produce a non-negligible rolling moment and the deflection of the ailerons can produce a non-negligible yawing moment. Since the gravity vector in leveled flight lies in the plane of symmetry, the CG position is not a dominant parameter for the lateral-directional characteristics as it is for the longitudinal. For this reason, the CG limits are dictated by considerations deriving from the longitudinal stability analysis.

Yaw stiffness (weathercock stability)

Yaw stiffness refers to the stability characteristics along the z axis, meaning that if the aircraft is at a certain sideslip angle β and it encounters crosswinds or other lateral disturbances, it can experience yawing moments that try to restore the symmetric flight condition. The yawing moment N (in the following it will be referred to as n) is positive as shown in figure 2.5 and to achieve yaw stiffness it is required that $\frac{\partial N}{\partial \beta}$ has to be positive.

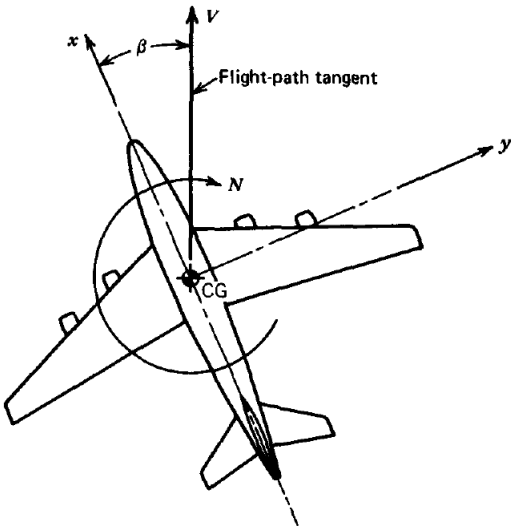

Figure 2.5: Yawing moment and sideslip angle
[10]

It is possible to define the nondimensional coefficient of n in the same way as the lift or drag coefficient:

$$C_n = \frac{n}{\frac{1}{2}\rho V^2 S b} \tag{2.3}$$

Using the non-dimensional coefficient, it is possible to state that in order to satisfy the stability requirement mentioned above, the ratio $\frac{\partial C_n}{\partial \beta}$ has to be positive. This ratio is usually written as $C_{n\beta}$. This parameter is determined by the sum of the contributions of the different components of the aircraft and the ones having the most influence are the vertical tail surfaces and the body, while the wing isn't as important as in the case of $C_{m\alpha}$.

Roll stiffness

Roll stiffness refers to the stability characteristics along the x axis and it is the inherent ability of an aircraft to resist rolling motion and maintain level wings during flight.

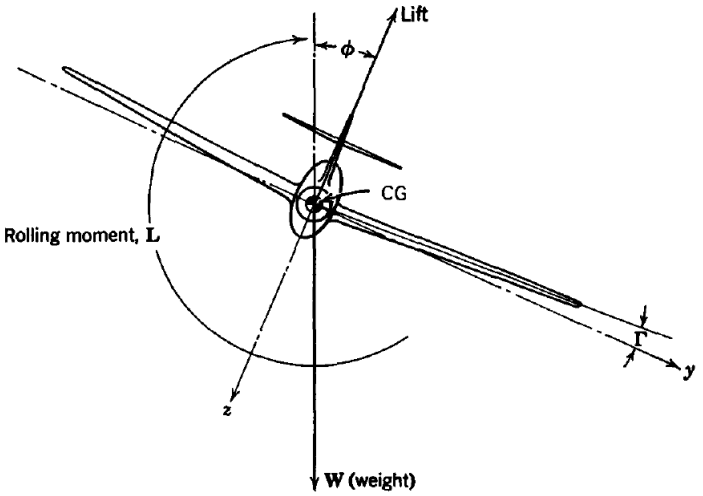

Figure 2.6: Rolling motion and dihedral angle
[9]

There is a fundamental difference in this case compared to yaw and pitch stiffness and it's the fact that the x axis may be coincident with the velocity vector. If they are coincident, no aerodynamic changes occur after a fixed rotation ϕ as shown in figure 2.6, and the aerodynamic field is kept symmetrical with reference to the plane of symmetry. Also, all the resultant forces are kept in the same plane and there is no variation in any aerodynamic coefficient, meaning that in this particular case the roll stiffness $\frac{\partial C_l}{\partial \phi} = C_{l\phi}$ is zero. C_l being the nondimensional coefficient of the rolling moment l as defined in equation 2.4:

$$C_l = \frac{l}{\frac{1}{2}\rho V^2 S b} \tag{2.4}$$

If the x axis and the velocity vector are not coincident, then the roll stiffness is a second-order effect of the derivative $\frac{\partial C_l}{\partial \beta} = C_{l\beta}$. Considering an angle of attack α_x between the x axis and the velocity vector, after a rolling motion determined by the angle ϕ, there is a velocity component that has projections on both the y and z axis, meaning that there is also sideslip and a variation of the angle β. As a consequence, roll stiffness depends on α_x: if α_x is positive then there is roll stiffness and the aircraft tends to keep the wings level. If it is negative, the stiffness is negative and the aircraft tends to roll until the value of C_l equals zero. The case in which α_x is zero was discussed above, resulting in a plane with no preferred roll angle. Considering that an aircraft has no first-order roll stiffness, the tendency to resist rolling motion is achieved thanks to the *dihedral effect*.

Dihedral is the upward angle Γ formed between the wings and the horizontal plane, as shown in figure 2.6. This dihedral angle plays a crucial role in providing roll stability. When an aircraft is in level flight, the wings generate lift. Due to the dihedral angle, each wing produces a slightly different amount of lift. The wing with a higher lift (the wing on the lower side of the dihedral angle) will experience a greater increase in drag compared to the wing with a lower lift. This difference in drag causes a rolling moment, which tends to level the wings and restore the aircraft to its original attitude.

2.2 Dynamic stability

Dynamic stability refers to the inherent ability of an aircraft to maintain a stable flight condition when subjected to disturbances or changes in its flight parameters and it is crucial for safe and efficient aircraft operation. It involves the aircraft's response to various forces and moments acting on it during flight, such as aerodynamic forces, control inputs, and external disturbances. The dynamic response can be either stable, unstable, or neutral depending on its behavior. While studying static stability isn't enough to asses the dynamic behavior of an aircraft, it may give some preliminary insight into what to expect from the dynamic analysis, meaning that neutral or negative static stability always leads to a dynamic stability of the same kind. On the other hand, positive static stability implies that any type of dynamic behavior can be achieved. In figure 2.7 possible dynamic responses of a statically stable aircraft are shown.

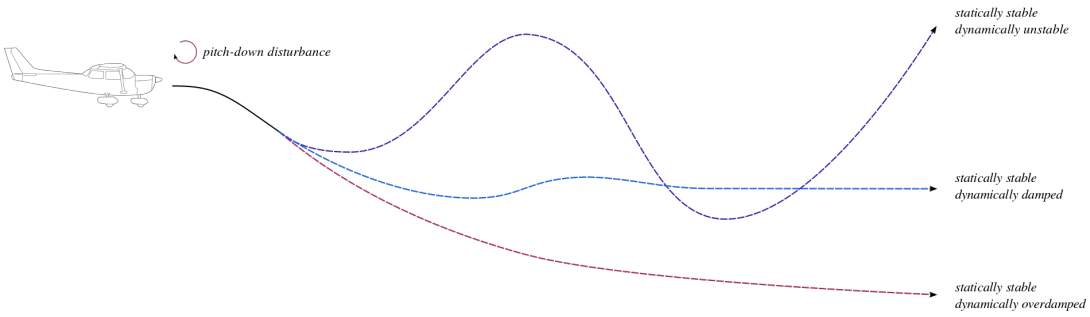

Figure 2.7: Dynamic response of a statically stable aircraft

To properly evaluate the dynamic response to a disturbance the six degrees of freedom equations of motion are used, simplified, and linearized with the help of the small disturbances theory, assuming that the motion of the airplane consists of small deviations about a steady flight condition. This method has been introduced by George H. Bryan [11] and it assumes that the variables in the equations of motion can be replaced by a reference value plus a perturbation or disturbance. This approach will lead to a set of linear differential equations that can be solved by applying eigenanalysis and obtaining the natural modes characterized by their particular frequency and dampening ratio. Further details on how to assess dynamic stability can be easily found in the literature and will not be discussed here, since in this study only the static stability will be analyzed.

Chapter 3

Wind tunnel corrections

3.1 Wind tunnel testing

Wind tunnel testing has been a staple in the development of new aircraft since the very beginning of aviation itself. The need to perform experimental analysis on new designs in order to understand their behavior during flight made the wind tunnel an essential instrument in the first half of the 20th century. With the advent of computational fluid dynamics, cheaper and faster estimations could be made but the effectiveness and precision of wind tunnel tests are still unmatched these days.

Wind tunnels can be divided into different categories based on their characteristics. They can be closed circuits or open circuits, the test section may be open or closed and have slotted walls. Also, many different flow visualization techniques can improve the understanding of the aerodynamics of a body, such as tufts, smoke, dye, pressure-sensitive paint (PSP), and many others; the choice depends on the need of each test. For the closed test section wind tunnels, special attention is needed regarding the data obtained from the test, since it will contain different errors due to the fact that airflow constricted by the walls exerts different forces on the model tested compared to the free air condition. In the following chapter, a more detailed analysis of this problem is completed and different possible solutions are provided.

The airflow in the free air condition is quite different from the finite stream condition that is found inside a closed wind tunnel. Therefore, boundary corrections are needed in order to obtain valid data from the tests. In order to highlight the difference between the two airflow conditions, we can refer to the example from Barlow et al. [12]. In free air conditions, the airflow is not restricted by any kind of constraint, while inside the wind tunnel, the walls are at a finite distance from the test subject, causing interferences on the resultant of forces exerted on the model [13].

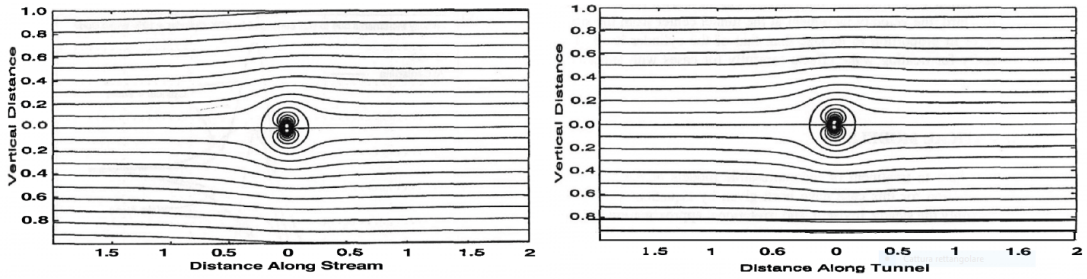

Figure 3.1: Streamline for a cylinder and wake in free air (left) and inside the wind tunnel (right)
[12]

In figure 3.1, it's possible to observe the streamlines of a cylinder and wake, idealized by two elementary flows following the potential flow theory: a doublet and a source [14]. The difference in the curvature of the streamline from the two cases can be clearly seen. Another difference derives from the presence of the actual model, which influences the flow properties upstream. When performing calculations on the data obtained from the wind tunnel, all the effects of the constraints on the flow must be taken into account. Over the years many different methods to estimate boundary corrections have been developed and, depending on each case, it may be better to choose one over the others. Haque et al. [15] explored the differences between the conventional analytical method of corrections, and more advanced CFD and experimental methods, on a generic model of a straight semi-span wing, comparing the results and highlighting the strengths and weaknesses of each one. In the following sections the conventional analytical method for boundary corrections, described by Barlow et al. [12] is thoroughly described.

3.2 Blockage corrections

3.2.1 Solid blockage

The solid blockage is the effect due to the presence of the model in a finite stream, as the area through which the air can flow is smaller compared to the free air condition. The ratio of the frontal area of the test subject to the stream cross-sectional area is zero in free air, while in the wind tunnel, this ratio illustrates the relative size of the model and the test section. The effect is that, by continuity and Bernoulli's equation, the airflow experiences an increase in velocity near the test model and it is a function of model thickness, thickness distribution, and model size, resulting in the overprediction of the surface stresses on the model inside the wind tunnel. In order to correctly evaluate this phenomenon, a blockage coefficient ε_{sb}, as defined in equation (3.1), is used to compute the effective upstream dynamic pressure, in which K_1 is a shape factor that depends on the body thickness-to-chord ratio, τ_1 a tunnel shape factor that depends on the tunnel test-section shape and the model span-to-tunnel-width ratio, V is the wing (or body) total volume and C is the wind tunnel cross-sectional area.

$$\varepsilon_{sb} = \frac{K_1 \tau_1 V}{C^{1.5}} \tag{3.1}$$

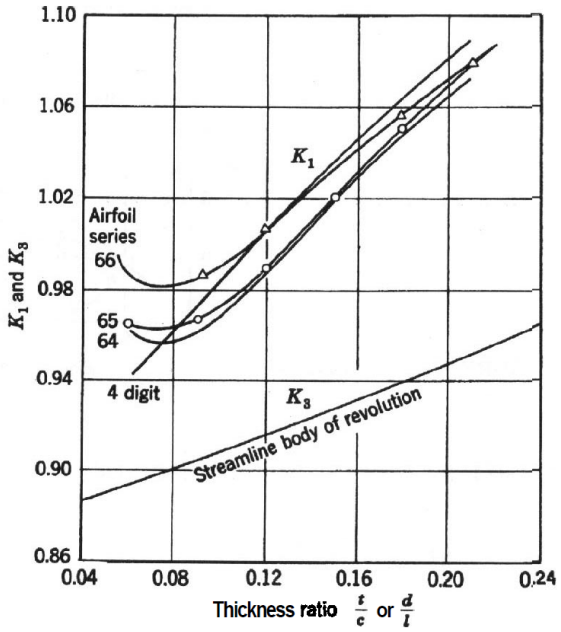

Figure 3.2: Body shape factor K_1 as a functions of thickness for different bodies [12]

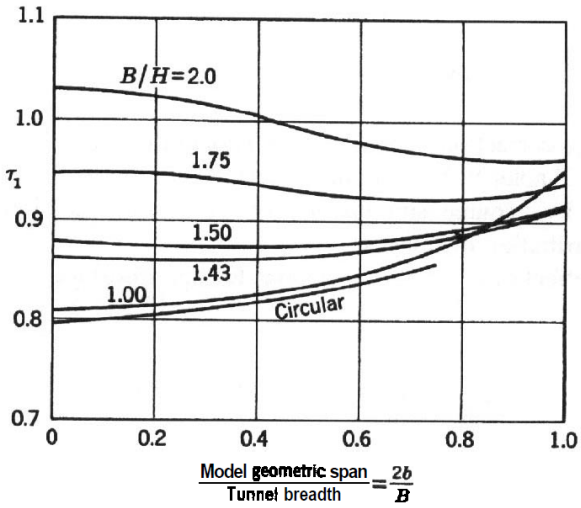

Figure 3.3: Tunnel shape factor τ_1 as a functions of span-to-tunnel-breadth ratio for different tunnel dimensions

[12]

Values for K_1 and τ_1 can be obtained graphically from figures 3.2 and 3.3.

3.2.2 Wake blockage

This effect is akin to solid blockage, but it's caused by the presence of the wake region behind the test model. The mean velocity of the wake will be lower than free stream, hence the velocity outside the wake will increase in order to maintain constant mass flow according to the continuity equation. Because of that, an increase in the measured drag will be experienced by the test model. This effect is proportional to the size of the wake which in turn is a function of the body shape and the ratio of the wake area to the tunnel area.

$$\varepsilon_{wb} = \frac{S}{4C} C_{D,0} + \frac{5S}{4C}(C_{D,u} - C_{D,0} - C_{D,i}) \tag{3.2}$$

In equation (3.2) the wake blockage ratio ε_{wb} is defined, where:

- $C_{D,0}$ is the zero-lift drag coefficient.
- $C_{D,u}$ is the uncorrected drag coefficient.
- $C_{D,i}$ is the induced drag coefficient.

The second term of equation (3.2) is relative to the separate flow condition, and it vanishes for angles below the separation threshold. The total blockage coefficient ε_t can be easily calculated by the sum of the previous two.

$$\varepsilon_t = \varepsilon_{sb} + \varepsilon_{wb} \tag{3.3}$$

Usually, the coefficient values for the model's wings and body are calculated separately and added together.

Using the corrected value of dynamic pressure for blockage effects, the lift coefficient as well as yawing moment, rolling moment, and side force have no further corrections, and thus final corrected values can be obtained from the force data, following the examples in the equation (3.4). Instead, the drag, pitching moment, and angle of attack need further corrections.

$$C_{L,c} = \frac{L_u}{q_c S} \tag{3.4a}$$

$$C_{Y_w,c} = \frac{S_u}{q_c S} \tag{3.4b}$$

$$C_{l,c} = \frac{l_u}{q_c S b} \tag{3.4c}$$

$$C_{n,c} = \frac{n_u}{q_c S c} \tag{3.4d}$$

3.3 Angle of attack corrections

The angle of attack corrections are based on the effect of downwash variation inside the wind tunnel, caused by its walls, acting as a finite boundary and preventing the infinite downwash extension that would exist in free air conditions. The result is a wall-induced AOA $\Delta\alpha$ that can be calculated using equation (3.5), in which δ is a boundary correction factor that depends on the span load distribution, ratio of model span to tunnel width, shape of the test section and whether or not the wing is on the tunnel centerline. It can be easily obtained from figure 3.4

$$\Delta\alpha = \frac{\delta S}{C} C_L(57.3)\ [deg] \tag{3.5}$$

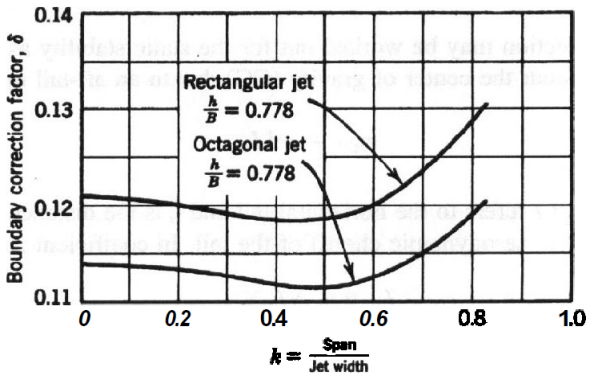

Figure 3.4: Boundary correction factor δ as a function of span-to-jet-width ratio k [12]

Finally, the corrected angle of attack can be obtained with equation (3.6), in which α_g is the geometric angle of attack.

$$\alpha_c = \alpha_g + \Delta\alpha \tag{3.6}$$

3.4 Drag Coefficient corrections

Similarly to angle of attack corrections, drag coefficient corrections result from the variation in downwash. Another correction is due to the buoyancy effect caused by the longitudinal pressure gradient inside the wind tunnel, evaluated following Glauert methodology [16]. The corrected drag coefficient can be evaluated from equation (6.2):

$$C_{D,c} = C_{D,u} + \Delta C_D + \Delta C_{D_{bu}} \tag{3.7}$$

Where $C_{D,u}$ and ΔC_D can be obtained respectively from equation (3.8) and (3.9)

$$C_{D,u} = \frac{D_u}{q_c S} \tag{3.8}$$

$$\Delta C_D = \frac{\delta S}{C} C_L^2 \tag{3.9}$$

The buoyancy drag contribution $\Delta C_{D_b u}$ can be evaluated from equation (3.10) in which λ_3 is a body shape factor that can be obtained from figure 3.5, $\frac{dp}{dl}$ is the longitudinal pressure gradient of the wind tunnel in [pa/m] and t is the body maximum thickness.

$$\Delta C_{D_{bu}} = -\frac{\pi}{4} \lambda_3 t^3 \frac{dp}{dl} \tag{3.10}$$

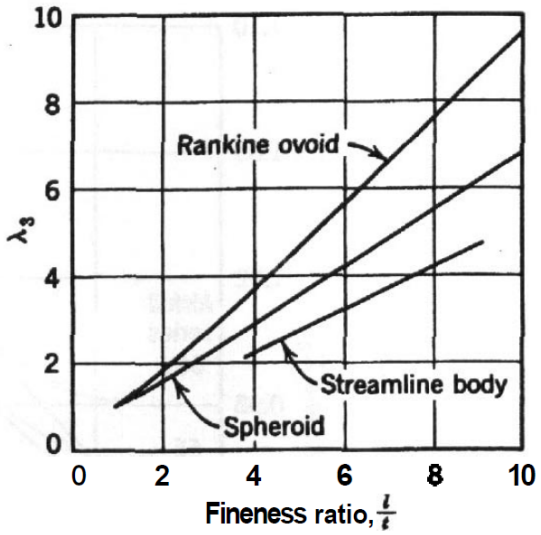

Figure 3.5: Body shape factor λ_3 as a function of the fitness ratio $\frac{l}{t}$ for different body shapes

[12]

3.5 Pitching moment coefficient corrections

The correction for the pitching moment is obtained considering that the amount of upwash at the tail of the model is higher in a closed-test section wind tunnel compared to the wings. This results in a model that appears much more stable compared to the free-air condition. The corrected pitching moment coefficient can be evaluated from equation (3.11):

$$C_{m,CG_c} = C_{m,CG_u} - \Delta C_{m,CG} \tag{3.11}$$

Where C_{m,CG_u} and $\Delta C_{m,CG}$ can be obtained respectively from equation (3.12) and (3.13), in which τ_2 is a downwash correction factor that depends on shape, type and length of the test section, the position of the wing and tail in relation to the tunnel and tail length l_t. τ_2 can be obtained graphically from figure 3.6

$$C_{m,CG_u} = \frac{M_u}{q_c S c} \tag{3.12}$$

$$\Delta C_{m,CG} = \left(\frac{\partial C_{m,CG}}{\partial \delta_s}\right)\left(\frac{S}{C}\right)\delta\tau_2 C_{L,w}(57.3) \tag{3.13}$$

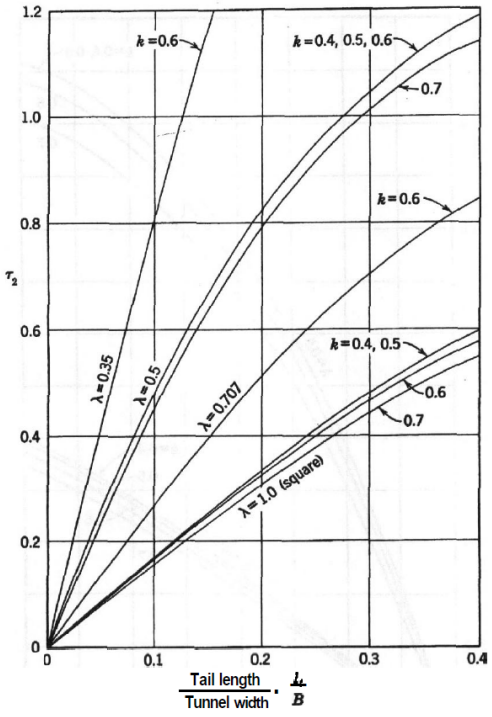

Figure 3.6: Downwash correction factor τ_2 as a functions of tail length l_t and tunnel width B

[12]

3.6 Support Interference

In any wind tunnel, the model needs to be supported in some way and that support will affect the quality of the flow inside the wind tunnel having some drag itself, thus causing what is called support interference. This interference causes a change in the pressure distribution on the model, resulting usually in an upflow effect that affects the accuracy of measured drag and pitching moment, which are critical data when testing a full model. Evaluating support interference is therefore required and there are different methods to complete this task, according to Horsten [17]. The choice depends on costs, accuracy, and implementation effort. Another important aspect to take into account is the setup used for model testing, as different setups may be better suited for different support interference evaluation methods depending on the type of balance used and the wind tunnel instruments. Three main methods can be used to evaluate support corrections:

1. **Experimental methods:** expensive and time-consuming compared to other methods as they often require different configurations to mount the model, often indicated as dummy setups. Support correction may be evaluated by subtraction of the measurement result of the different configurations to obtain the correction for the desired one. This technique is referred by Horsten [17] as Δ *measurements*. An example of this technique is shown in figure 3.7 where the support interference of a sting-mounted model with an internal balance is obtained by the subtraction of the aerodynamic characteristics of various setups.

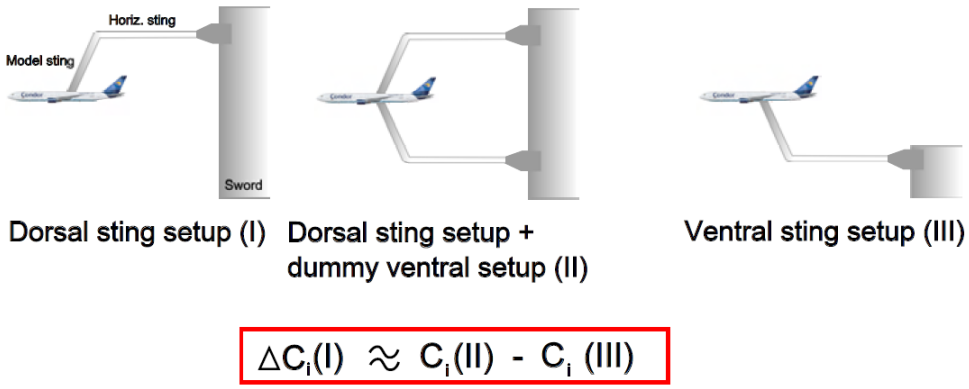

Figure 3.7: Δ measurements technique on sting-mounted model [17]

This technique is not always applicable as some models and tunnels may have problems with the mounting of different setups.

2. **Empirical methods:** these methods employ available data and an example can be the one proposed by Eckert [10] and it focuses on evaluating support interference based on similarities of both geometry (model and support) and test set-up. This method is therefore fast and affordable but its main drawback is that it requires a considerably large database for support interference calculations.

3. **Computational fluid dynamics (CFD):** CFD analyses are becoming more reliable and precise as the available computational power increases over the years, allowing to model complex geometries that are otherwise hard to investigate. There are many different types of simulations that can be performed, for example using vortex-lattice codes as done by Vaucheret [18], methods that rely on the distribution of singularities as demonstrated by Quemard [19] Interference in Large Low-Speed Wind Tunnels and methods that rely on the volumetric discretization of the flow that solves the Navier-Stokes equations as shown by Horsten and Mouton [17][20]. While all these methods can provide satisfactory results, CFD analysis can be time-consuming and computationally hard to perform.

3.7 Flow angularity

In order to collect correct data, the model must be properly aligned with the flow within the wind tunnel. An ideal wind tunnel setup includes a flow parallel to the test section borders, requiring just the external balance to be oriented in order to get lift perpendicular to the ceiling and drag parallel to the ceiling and floor. In reality, the flow is almost never perfectly parallel in the test section, but there is a certain degree of either upflow or downflow (usually referred to upflow) and cross-flow. Upflow effects cause an error in drag measurements and therefore are more critical than cross-flow for a full model. Usually, the procedure is to align the balance to obtain lift and drag in the proper direction and then measure the upflow and apply the proper correction in the data reduction process. In order to align the balance, a series of runs with the model upright and inverted are performed, from zero lift to stall, and the data gathered from the different runs is plotted to obtain lift, polar, and moment, as shown for example in figure A.2 and A.3. For the inverted runs, the negative values obtained are represented as though they were positive, in order to properly compare the two different cases.

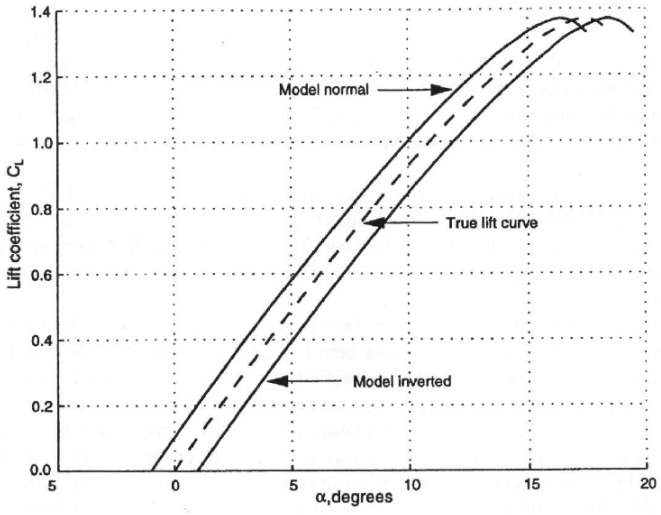

FIGURE 7.21 Upright and inverted C_L versus a curves.

Figure 3.8: Upright and inverted C_L - α curves [12]

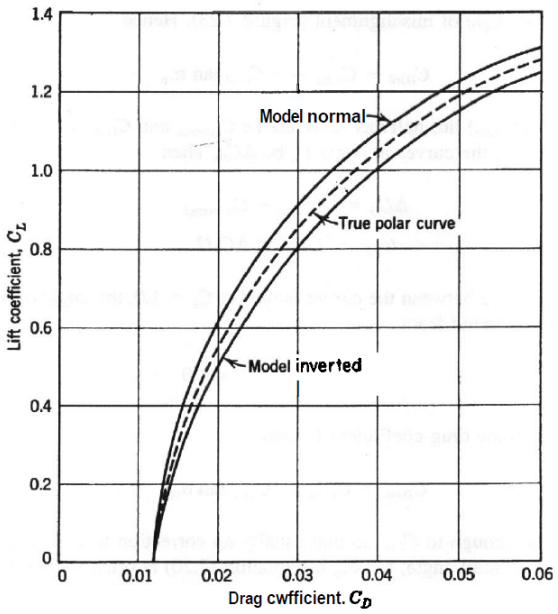

FIGURE 722 Drag polar, C_L versus C_D.

Figure 3.9: Upright and inverted drag polar, C_L vs C_D [12]

In the ideal case, with no upflow in the wind tunnel, the upright and inverted curves would overlap perfectly, while in reality, we can see that there is a certain variation between the two. The angular variation between the lift curves is double the error of the angle of attack setting. This procedure is time-consuming and often the wind tunnel model that is the object of the study is not designed to be tested both upright and inverted, for this reason, a calibration model or wing is used to perform the flow angularity evaluation and then the correction obtain are applied in the data reduction of the model that we need to study.

Chapter 4

Literature review

Modern studies on the BWB concept began around the beginning of the 90s. What sparked the interest in this configuration was an analysis performed by Boeing that showed the evolution of the aerodynamic figure-of-merit (ML/D) with time between the 60s and 90s. The result is shown in figure 4.1, and it's easy to see that the curve is almost flat, meaning that no real progress was made in 30 years on aerodynamic efficiency.

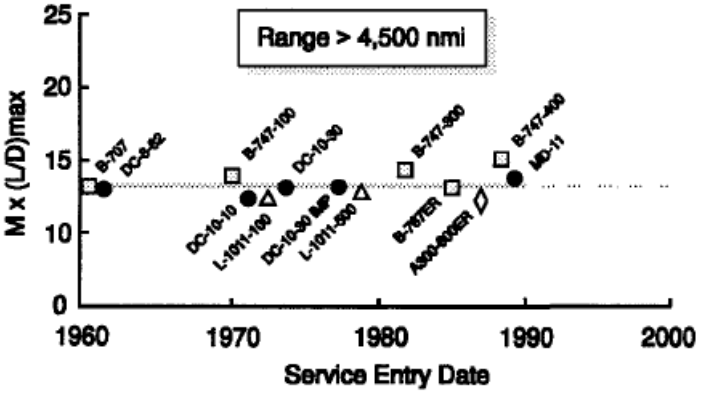

Figure 4.1: Progress in aerodynamic efficiency
[21]

Comparing a BWB aircraft with a conventional configuration one, it was found that while employing the same level of technology it's possible to achieve an increase in lift-to-drag ratio, thanks to a reduced total wetted area, and better fuel consumption. The estimated benefits of a BWB aircraft can be summarized in table 4.1.

Fuel burn	−27%
MTOM	−15%
Operating empty weight	−12%
Total thrust	−27%
Lift/Drag	+20%

Table 4.1: BWB benefits over a traditional aircraft

The improvements in performance potential incentivized NASA Langley to fund Boeing in order to perform the development of a new subsonic aircraft featuring a BWB design. Liebeck et al. [21] performed a feasibility study in 1998 of a BWB subsonic transport airplane for the design mission described in table 4.2.

800 passengers in 3-class seating
7000 nautical mile range
0.85 cruise Mach number
11000-foot takeoff field length
Composite primary structure
Advanced ducted propeller engine technology
2020 entry into service

Table 4.2: Desing mission data

The result of this study is the aircraft shown in figure 4.2

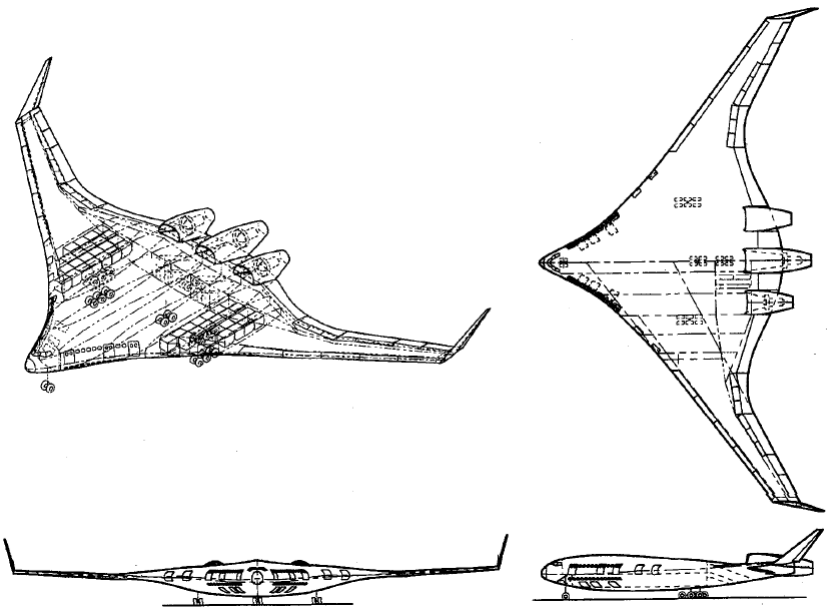

Figure 4.2: BWB aircraft configuration
[21]

The aircraft's construction was meant to be made of composite material, and it had two decks to carry passengers. Aerodynamic performance was improved by using moderately loaded airfoils on the outboard wing to reduce drag and achieve an elliptic span load. In terms of stability, it was discovered that in order to trim the aircraft, a statically unstable aircraft is necessary. Special high-lift systems are not required due to the low wing loading. Still, a leading-edge slat on the outboard wing and trailing edge elevons and stability augmentation and envelope protection systems are necessary. The outboard elevons provide pitch and roll control, but because they are very short-coupled, control blending with the inboard ones is required. Directional stability and control are provided by winglets at the wing tips, with a drag rudder employed for low-speed conditions. A small-scale

model featuring a 17 ft wingspan (BWB-17), dynamically scaled to match the full-scale aircraft flight behavior, was tested to explore low-speed flight mechanics. Thanks to an onboard computer, stability augmentation ensured a successful test flight with satisfactory handling qualities in the normal flight envelope. This study demonstrated the benefits of adopting the blended wing-body configuration over the traditional one, assessing the technical feasibility of this concept.

Wisnoe et al. [22] performed experimental tests on two different iterations of their UiTM Blended Wing body, indicated as Baseline-I and Baseline-II. A representation of the two different configurations is shown in figure 4.3.

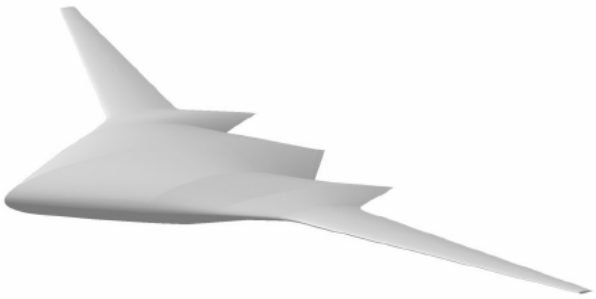

(a) Baseline-I

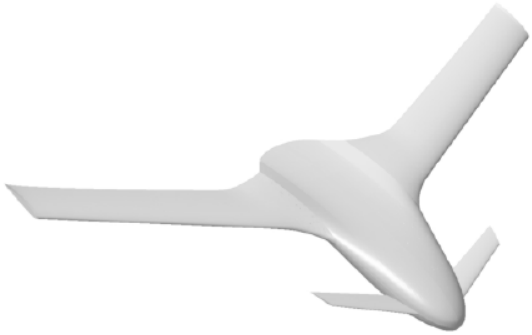

(b) Baseline-II

Figure 4.3: UiTM BWB models
[22][23]

The Baseline-I model features a geometry similar to those presented by Liebeck et al. [21], with elevators mounted at the trailing edges of the wing. Baseline-II is radically different from the previous concept as this now features a pair of canards in front of the wings. The Baseline-I model has been studied both in CFD and wind tunnel [22][24] with a focus on low Mach performances and elevator effectiveness [23]. The wind tunnel setup consisted of a 0.5x0.5 test section suction type wind tunnel, featuring a 3 3-component balance measuring lift and drag forces and pitching moment. For this reason, a half model has been manufactured by CNC machined aluminum, scaled to a 1/6 of the full-scale model. This concept achieved a stall AOA of 35° in the wind tunnel tests, with similar results in CFD, but from flow visualization using tufts, it was observed that at $\alpha = 8°$ the flow was almost completely separated from the wings as it can be seen from figure 4.4.

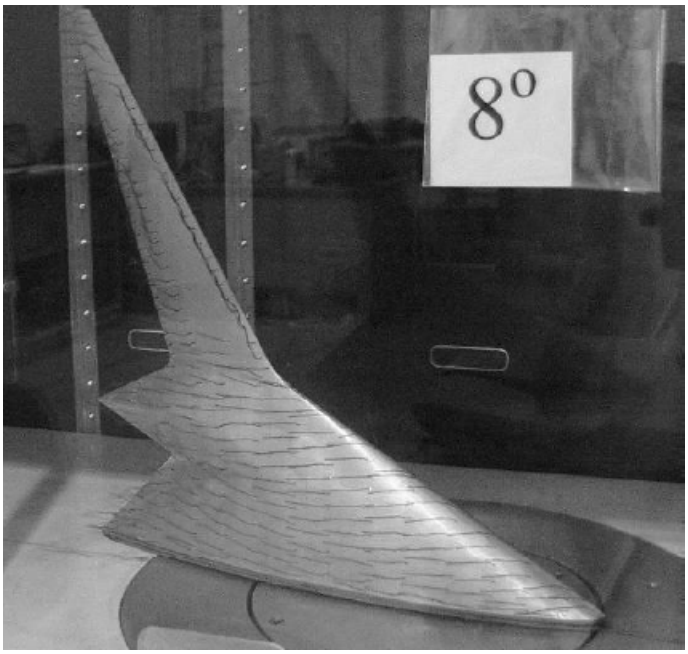

Figure 4.4: Baseline-I flow separation on the wing [24]

The result is that, past that angle of attack, the body generates all the lift until the stall angle is reached. At low AOA, the measured C_D is low, but as soon as the wings stall, it rapidly increases with α, and it was noticed that at higher air speeds (or Reynolds), higher drag coefficients were produced. Analyzing the lift-to-drag ratio, the maximum value was reached for low AOA, where the flow is still attached to both the body and the wings, but the maximum is still quite low compared to other BWB concepts, meaning the efficiency can be improved. Focusing on the pitching moment and elevator efficiency [23] , longitudinal static stability was achieved as the $C_m - \alpha$ curve has a negative slope with a positive value of C_{m_0} but the elevators positioned at the trailing edge of the wings were found to be quite ineffective, as they produced a little variation on lift, drag and pitching moment with different deflections, ranging from $\delta_e = -10°$ to $\delta_e = 10°$. Since the elevator deflections were tested for a fixed value of $\alpha = 3°$, the flow was still attached to the model, it can be said that the low performances of the elevators are probably caused by their position and the overall aerodynamic behavior of the Baseline-I model. For this reason, the Baseline-II model was developed, featuring broader chord wings while maintaining the wing span and a slimmer body. These variations, together with the canards, improved the aerodynamic efficiency. In contrast, the canards in front of the wing managed to have a noticeable impact on lift, drag, and pitching moment, proving their effectiveness.

Another relevant investigation was performed by Vicroy et al. [25] in the frame of the NASA ERA (Environmentally Responsible Aviation) project in collaboration with Boeing. A set of wind tunnel tests on a 5.75% scale model of a BWB twin-engine aircraft were conducted in two different low-speed wind tunnels, the 14 by 22-foot Subsonic Tunnel and the NFAC 40 by 80-foot Tunnel. Pictures of the two setups can be seen in figure 4.5.

(a) 14- by 22-Foot Subsonic Tunnel

(b) NFAC 40- by 80-Foot Tunnel

Figure 4.5: Wind tunnel setups
[25]

The model is a scaled version of the Boeing BWB-0009G configuration and it's made out of aluminum and has a test weight of around 566kg (instruments included). As shown in figure 4.6, it features 13 control surfaces along the trailing edge and has a vertical tail, different from the concepts presented above. The outboard elevons can be split, acting as drag rudders, providing directional control, or can be used as standard elevons. The vertical tails can be deflected and feature ruddervators along the trailing edge.

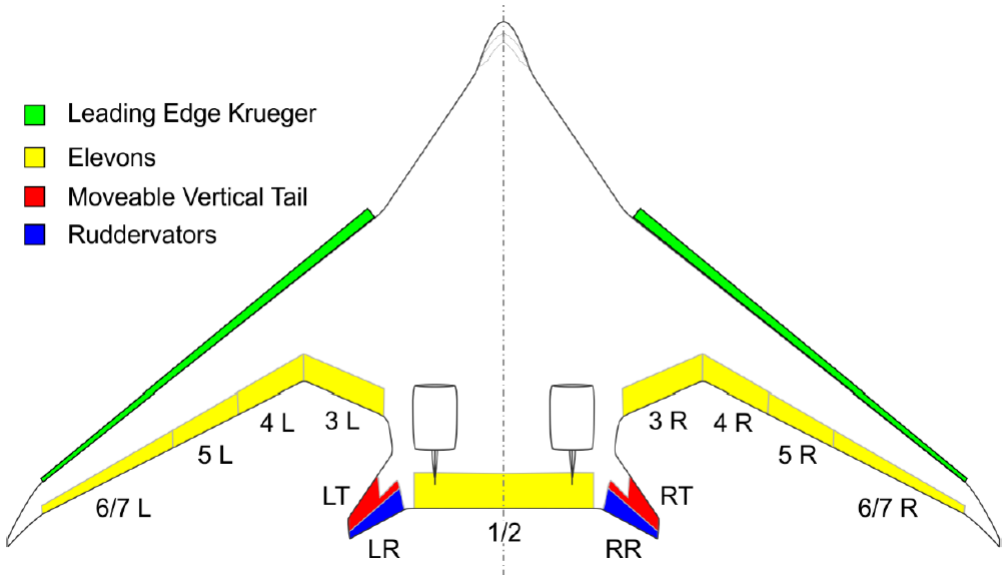

Figure 4.6: Control surfaces on the model
[25]

Wind tunnel corrections were performed on the raw data obtained, using both CFD-based methods and the classic method, illustrated in detail in chapter 3. Corrections for buoyancy, blockage, and stream curvature effect were implemented, but since the CFD model was available only for the 14x22 wind tunnel, the results were corrected primarily using the classic method. Nonetheless, a comparison of the two different methods was carried out for the 14x22 tunnel, since it has the ability to lift the ceiling, it enables the tester to choose between a closed and open test section configuration. The main differences between the two correction approaches can be seen in the corrections on lift and drag at high AOA, however, both methods provide good approximation in matching the closed test results to the open test section ones. Although the CFD method was expected to provide better corrections, in reality, it was found that its performance was non better than the classic approach and sometimes even worse, as can be seen from figure 4.7.

In figure 4.8, 4.9 and 4.10 the results from the wind tunnel are represented in the cruise configuration. AOA was kept under 21° in order to avoid separation and thus large variations in the data. From the $C_m - \alpha$ plot in figure 4.8 it's possible to see that for low angles of attack, a certain degree of longitudinal stability is achieved, while at high angles of attack, the model is completely unstable. From the plots in figure 4.10 it's possible to understand that since both the C_{l_β} and C_{Y_β} derivatives are negative, the requisites for both lateral and sideslip static stability are satisfied. Since the values for the C_{n_β} derivative are slightly positive or negative, depending

on the reference axis (body or stability), we have a neutral directional stability in this case.

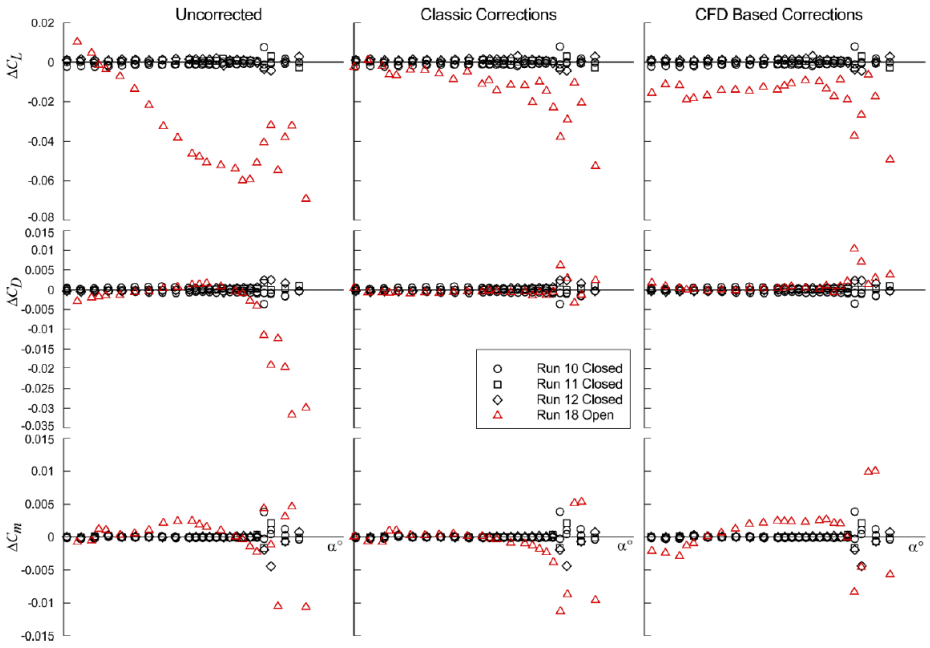

Figure 4.7: Comparison of the difference from the average of the closed test section runs

[25]

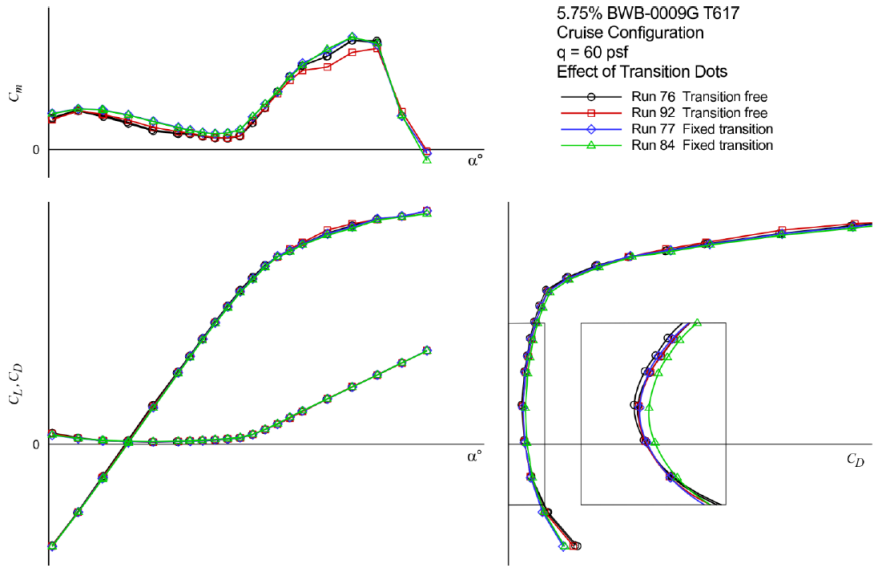

Figure 4.8: Longitudinal force and moment coefficients - cruise configuration [25]

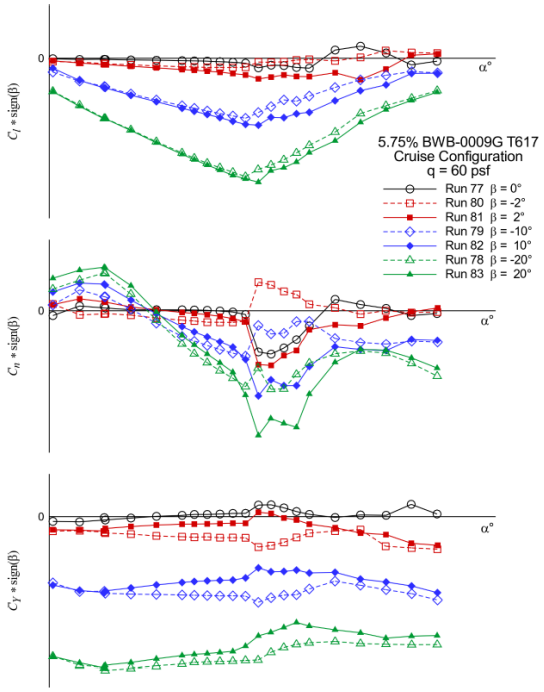

Figure 4.9: Effect of sideslip on the lateral/directional force and moment coefficients - cruise configuration

[25]

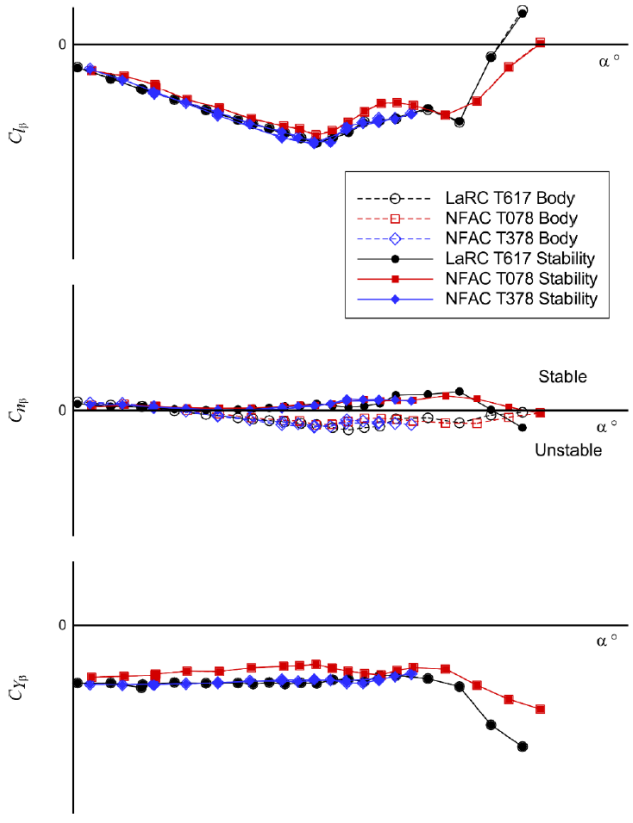

Figure 4.10: Lateral/directional sideslip derivatives - cruise configuration

[25]

A comparison between numerical and wind tunnel data has been carried out by Gryte et al. [26] on the Skywalker X8 Fixed Wing UAV. Numerical data was acquired via CFD simulations using XFLR5, based on the Vortex Lattice Method (VLM), while the wind tunnel data was used to develop an aerodynamic model of the UAV.

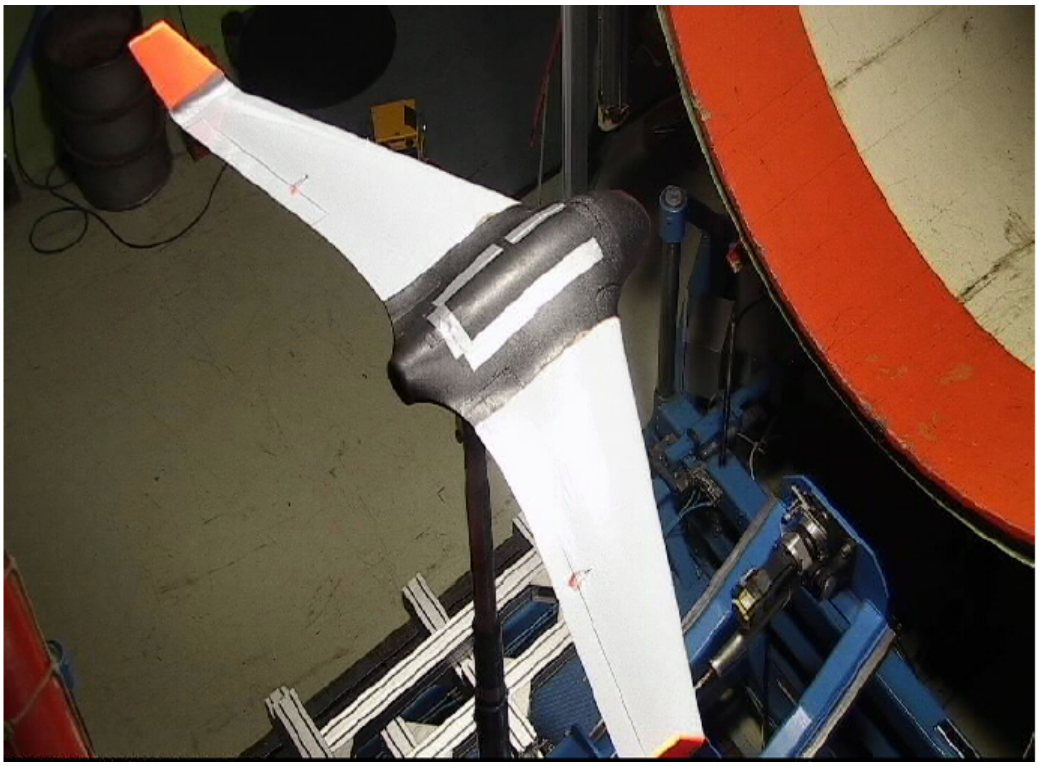

Figure 4.11: Wind tunnel setup of the Skywalker X8 [26]

The UAV was tested at the Czech Aerospace Research Center (VZLU) in Prague with the following test setup: the model has a multi-component strain-gauge mass balance mounted inside, used to measure the forces and moments exerted on it and it presented a hole in the rear section of the fuselage to accommodate the balance. The latter was further connected to a vertical rod that was used to change the angle of attack and the side slip angle by rotating it longitudinally or laterally. The main focus of the experiments was to investigate the behavior around the cruise condition, meaning a reynolds matching cruise speed and $\alpha = \beta = \delta_a = \delta_e = \delta_r = 0$, with the assumption that longitudinal and lateral dynamics are decoupled. The longitudinal dynamics were tested assuming linearity in the angle-of-attack up to the stall of the wing and concentrated on describing the lift, drag, and pitch moment as functions of angle-of-attack and elevator deflection. The tests are run by switching between various angles of attack (α from $-5°$ to $15°$) for various Reynolds numbers and elevator deflections while maintaining a constant aileron and side-slip angle of zero.

The side force, roll moment, and yaw moment expressions as functions of side-slip angle, and aileron deflection, were the main goals of the lateral testing, and linearity in side-slip angle up to the stall of the winglets was assumed. The tests were run by varying the side-slip angles (β from $-15°$ to $15°$) for various Reynolds numbers and control surface deflections while maintaining a constant angle-of-attack of zero. In order to simplify, the assumption of symmetry about the body's x-axis was made. After collecting all the wind tunnel data, it was fitted to the model given by equation 4.1 using a linear regression model. This model is obtained by assuming that Froude-, Mach-, Strouhal- and Reynolds number effects are negligible and that the aircraft's mass and inertia outweigh those of the surrounding air. Another simplification is that for small AOA, lift and pitching moment coefficients are considered linear in α, q, and δ_e and independent of $\beta, p, r, \delta_a, \delta_r$. On the contrary, the yaw and roll coefficients are linear in $\beta, p, r, \delta_a, \delta_r$ and independent of α, q, and δ_e. Regarding the drag coefficient, a linear model couldn't be used because of its quadratic behavior in α. Although lateral and longitudinal dynamics are considered decoupled, one coupling term is considered, with drag force depending on the sideslip angle at low AOA, and because of the symmetry described, it's an even function in the sideslip angle.

$$\begin{bmatrix} C_D \\ C_Y \\ C_L \end{bmatrix} = \begin{bmatrix} C_{D_0} + C_{D_{\alpha 1}}\alpha + C_{D_{\alpha 2}}\alpha^2 + C_{D_{\delta_e}}\delta_e^2 + C_{D_q}\frac{c}{2V_a}q + C_{D_\beta 2}\beta^2 + C_{D_\beta}\beta \\ C_{Y_0} + C_{Y_\beta}\beta + C_{Y_p}\frac{b}{2V_a}p + C_{Y_r}\frac{b}{2V_a}r + C_{Y_{\delta_a}}\delta_a + C_{Y_{\delta_r}}\delta_r \\ C_{L_0} + C_{L_\alpha}\alpha + C_{L_q}\frac{c}{2V_a}q + C_{L_{\delta_e}}\delta_e \end{bmatrix}$$
$$\begin{bmatrix} C_l \\ C_m \\ C_n \end{bmatrix} = \begin{bmatrix} \left(C_{l_0} + C_{l_\beta}\beta + C_{l_p}\frac{b}{2V_a}p + C_{l_r}\frac{b}{2V_a}r + C_{l_{\delta_a}}\delta_a + C_{l_{\delta_r}}\delta_r\right) \\ C_{m_0} + C_{m_\alpha}\alpha + C_{m_q}\frac{b}{2V_a}q + C_{m_{\delta_e}}\delta_e \\ \left(C_{n_0} + C_{n_\beta}\beta + C_{n_{p\frac{b}{2V_a}}}p + C_{n_r}\frac{b}{2V_a}r + C_{n_{\delta_a}}\delta_a + C_{n_{\delta_r}}\delta_r\right) \end{bmatrix} \tag{4.1}$$

The aerodynamic coefficients from both the CFD simulations and the wind tunnel experiments are summarized in table 4.3, along with root mean square error (RMSE) and the coefficient of determination (R^2). From the table, it can be seen that most of the coefficients from the wind tunnel tests have a good fit with the data since most of the R^2 are close to 1. Regarding the stability of the model, from the positive value of C_{m_0} and the negative value of C_{m_α}, it's possible to see that longitudinal stability is achieved, while the positive value of C_{n_β} and the negative values of C_{l_β} and C_{Y_β} indicates that the lateral-directional stability is obtained.

	WT	XFLR5	RMSE	R^2
C_{L_0}	0.0867	0.0477	0.0153	0.996
C_{L_α}	4.02	4.06	0.0153	0.996
$C_{L_{\delta_e}}$	0.278	0.7	0.0153	0.996
C_{L_q}	–	3.87	–	–
C_{D_0}	0.0197	0.0107	0.00262	0.982
C_{D_α}	0.0791	−0.00955	0.00262	0.982
C_{D_α}	1.06	1.1	0.00262	0.982
$C_{D_{\delta_e}}$	0.0633	0.0196	0.00262	0.982
$C_{D_{\beta_2}}$	0.148	0.115	0.00234	0.734
$C_{D_{\beta_1}}$	−0.00584	$-2.34E-19$	0.00234	0.734
C_{m_0}	0.0302	0.00439	0.00576	0.983
C_{m_α}	−0.126	−0.227	0.00576	0.983
$C_{m_{\delta_e}}$	−0.206	−0.325	0.00576	0.983
C_{m_q}	–	−1.3	–	–
C_{Y_0}	0.00316	$1.08E-08$	0.00326	0.991
C_{Y_β}	−0.224	−0.194	0.00326	0.991
$C_{Y_{\delta_a}}$	0.0433	0.0439	0.00326	0.991
C_{Y_p}	–	−0.137	–	–
C_{Y_r}	–	0.0839	–	–
C_{l_0}	0.00413	$1.29E-07$	0.00476	0.953
C_{l_β}	−0.0849	−0.0751	0.00476	0.953
$C_{l_{\delta_a}}$	0.12	0.202	0.00476	0.953
C_{l_p}	–	−0.404	–	–
C_{l_r}	–	0.0555	–	–
C_{n_0}	−0.000471	$1.51E-07$	0.000615	0.98
C_{n_β}	0.0283	0.0312	0.000615	0.98
$C_{n_{\delta_a}}$	−0.00339	−0.00628	0.000615	0.98
C_{n_p}	–	0.00437	–	–
C_{n_r}	–	−0.012	–	–

Table 4.3: Skywalker X8 aerodynamic coefficients

Suewatanakul et al. [8] performed the conceptual design of the Green Raven UAV, obtaining the baseline configuration and geometry of the UAV along with the basic aerodynamic performance parameters. The initial design was carried out by following the methodology described by Raymer [27] and illustrated in figure 4.12 in which the Novel Technology replaces Technology Available, initially indicated by Raymer, and is indicated as a driver for the development of the aircraft at the same level of the Mission Requirements. Mission requirements are indicated by the objective of achieving a 1-hour endurance at 500 m cruise altitude, employing paved runways.

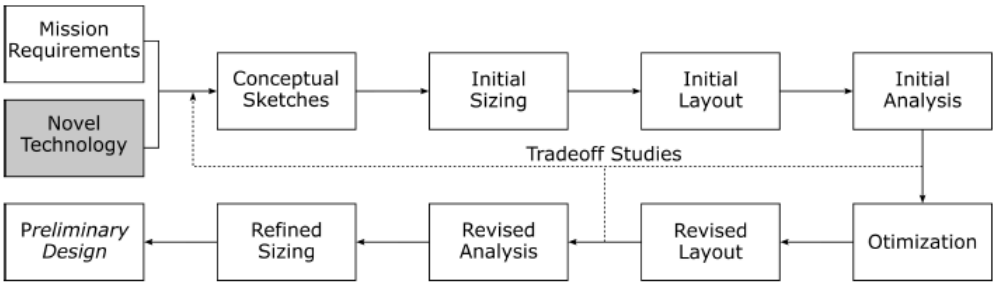

Figure 4.12: Design procedure
[8]

The results from the initial weight estimation process are indicated in table 4.4 and an aerodynamic sizing and analysis followed it. In order to comply with the dimensions and performance requirements, the Martin Hepperle MH104 and the MH61 airfoils, respectively for the body and the wings, were chosen.

Symbol	WF	W [N]
W_{TO}	1.000	245.3
W_{Struct}	0.565	138.65
W_{Sub}	0.075	18.4
W_{Prop}	0.095	23.3
W_{Avion}	0.050	12.3
W_{PL}	0.055	13.5
W_{Energy}	0.160	39.2

Table 4.4: Initial weight sizing

After completing the aerodynamic analysis of the airfoils using XFOIL [28] an iterative procedure in order to define the final UAV configuration was completed, using OpenVSP [29] to optimize the geometry of the blending section and the wing, while the wings shape was optimized using xflr5 [30]. As a result, in table 4.5 the final configuration geometry parameters are listed, and in figure 4.13 a detailed image of the UAV is presented.

Parameter	Value	Unit
Wing span b	4	[m]
Centre chord c_{cl}	1.7	[m]
Root chord c_r	1.29	[m]
Tip chord c_t	0.25	[m]
Aspect ratio AR	5.57	[-]
Planform area S	2.87	$[m^2]$
Average wing sweep Λ_{avg}	30	[◦]
Wing loading W/S	85.5	N/m^2
Oswald efficiency factor e	0.88	[-]

Table 4.5: Final configuration geometry

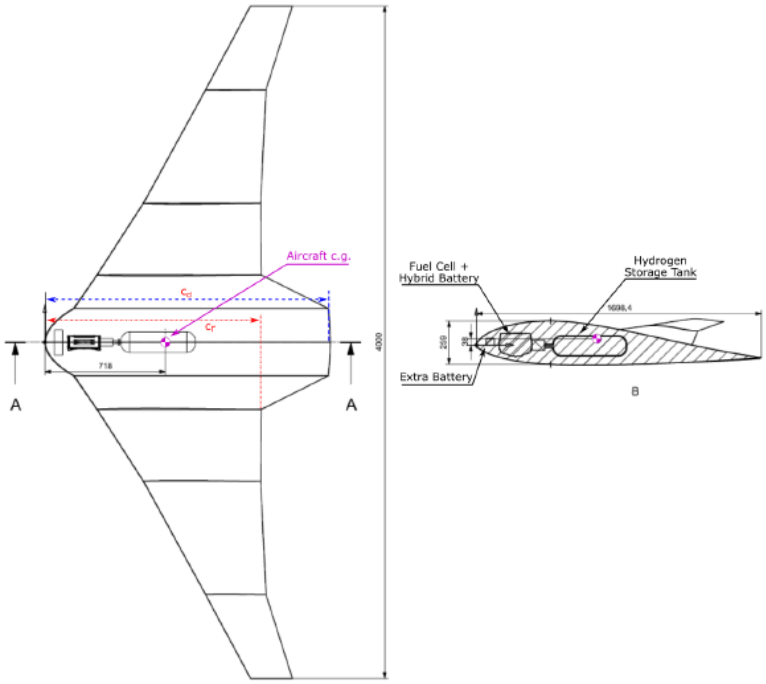

Figure 4.13: Green Raven reference geometry
[8]

Having defined the geometry of the model the aerodynamic performances of the model were studied by performing numerical analysis, with both low and high-fidelity methods. Low-fidelity numerical methods are used to obtain a solution quickly with a low computational cost, at the expense of the solution's precision. In this case, three types of viscous solutions were considered: the vortex lattice method (VLM2), the panel method, and the non-linear lifting line theory (LLT). A high-fidelity analysis was conducted using CFD, employing the commercial software Star-CCM+. A Reynolds-Averaged Navier-Stokes (RANS) model was used in conjunction with the Spalart-Allmaras model turbulence model, which was preferred over the $k-\omega\,SST$ for its more stable convergence of the solution at high AOA. In the following table 4.6, a comparison between the aerodynamic parameters obtained with the different methods is presented.

Parameter	Unit	VLM2	LLT	Panel Method	CFD	Initial sizing
C_{L_α}	$[\circ^{-1}]$	0.068	0.079	0.071	0.068	-
$C_{L_{max}}$	[-]	-	0.90	-	0.789	0.95
α_{max}	$[\circ]$	-	9	-	8.5	-
C_{D_0}	[-]	0.008	0.009	0.009	0.011	0.015
C_{m_0}	[-]	0.004	0.000	0.009	0.002	-
C_{m_α}	$[\circ^{-1}]$	-0.0031	-0.0026	-0.0039	-0.0024	-

Table 4.6: Aerodynamic parameters comparison

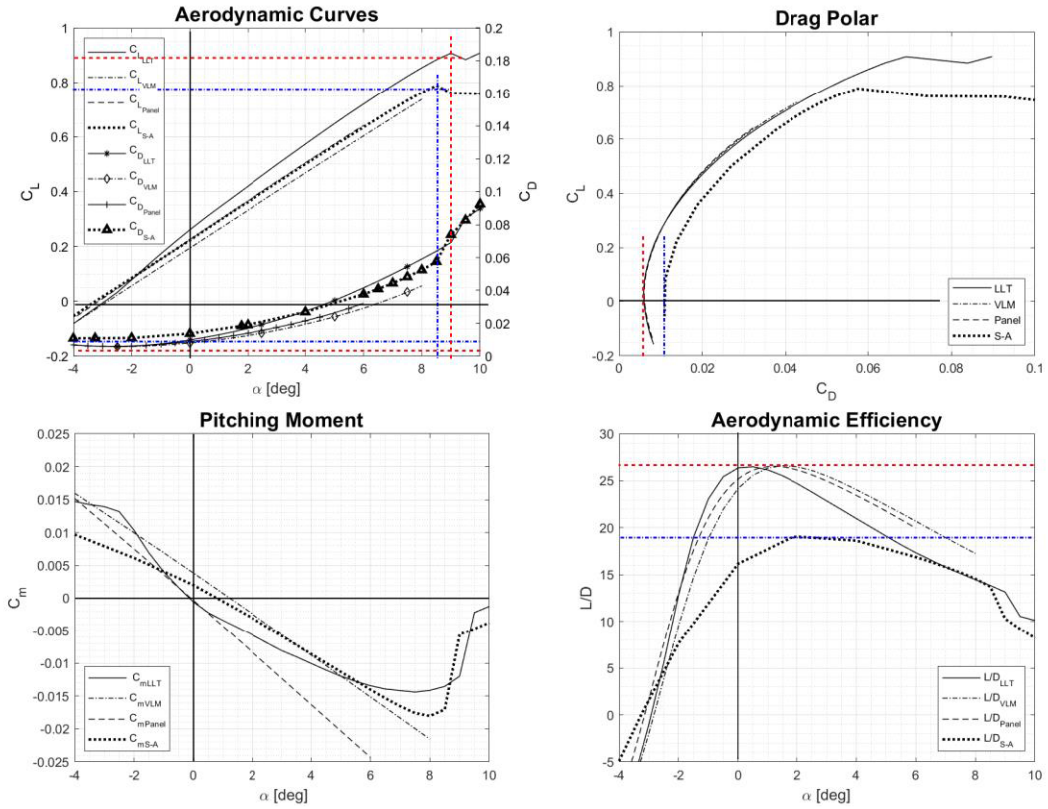

Figure 4.14: Aerodynamic result comparison
[8]

In figure 4.14 lift, drag, pitching moment coefficient, and L/D vs α graphs are illustrated. All data contained in this figure and in the previous table are obtained at the cruise speed of 20 m/s and with an α sweep ranging from $-4°$ to $12°$. As can be seen from the C_L vs α curves, there's a good matching between the different methods, and the same results are obtained for the drag coefficient, with the CFD results displaying the highest values, but this is expected since the low-fidelity methods are known to underpredict drag. Consequentially, in the L/D vs α graph, it can be seen that the curve relative to the CFD results displays the lowest aerodynamic efficiency. Regarding the pitching moment coefficient, results are highly different based upon the method used, although for all of the C_{m_α} is negative, and hence the aircraft is stable. Also, the values of C_{m_0} are slightly different, but all of them are close to zero, guaranteeing a balanced flight at cruise AOA.

Chapter 5

Wind tunnel testing procedure and data gathering

5.1 Model Specifications

The Green Raven model used for these tests is a 37.5% scaled-down version of the full-scale model, featuring a wing span of 1.5 m. It was designed by Filippo Panteri and Lakshmi Narasimhan, students from the Green Raven Project team, and it features 3D printed body parts made out of nylon. Model reference geometry values and weight are listed in table 5.1.

Wing span	$1.5\,m$
Wing area	$0.4\,m^2$
Reference chord	$0.36\,m$
Total weight	$\approx 6\,kg$

Table 5.1: Geometry values

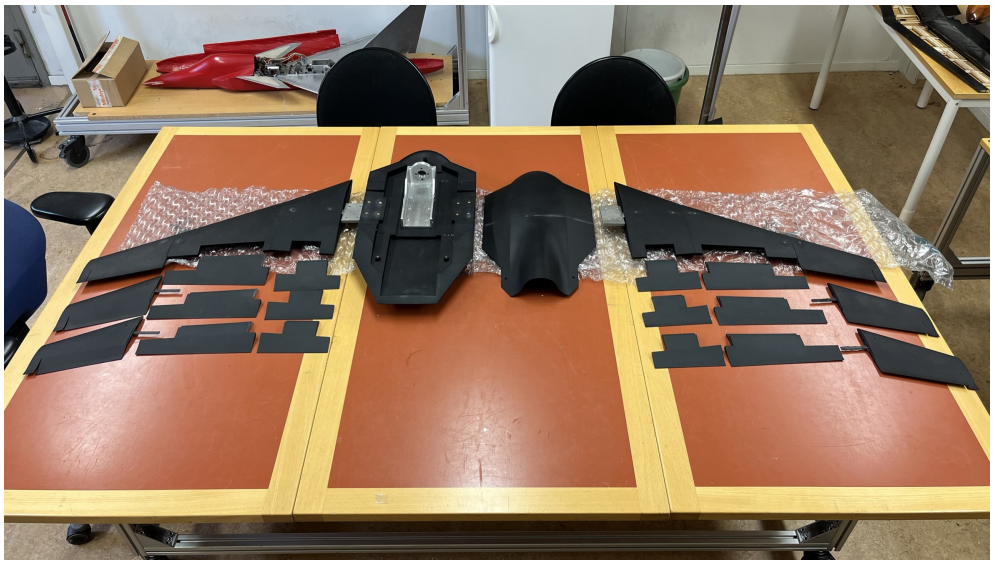

Figure 5.1: Green Raven 3D printed parts

As can be seen from figure 5.1 the model was thoroughly structurally broken down into various components. The model was segmented into two basic sections: its central body and the wing. Each of these portions was further subdivided into subcomponents to facilitate assembly and structural integrity. The center body was divided into upper and lower sections, which were then subdivided into three distinct pieces for the lower area and two distinct components for the upper section. The connection of these components was accomplished with the use of epoxy adhesive, which ensured a secure bond. On the other hand, the core component of the body used a more versatile assembling method, utilizing screws for quick and adaptive reconfiguration. As for the wing construction, it was built with three main pieces, as well as an incorporated spar made of aluminum. The inboard and mid-board elements of the wing were engineered with cut holes to accommodate the control surfaces (flaps). The outer parts, on the other hand, had a fixed-angle control surface (aileron) that could be easily replaced to adjust the angle of attack of the wing. Both the attachment of these components to the spar and the subsequent integration of the spar with the central body were accomplished using a dependable and durable screw-based fastening system. This unified assembly method maintained structural integrity and flexibility, allowing the model to be seamlessly adapted for numerous experimental setups.

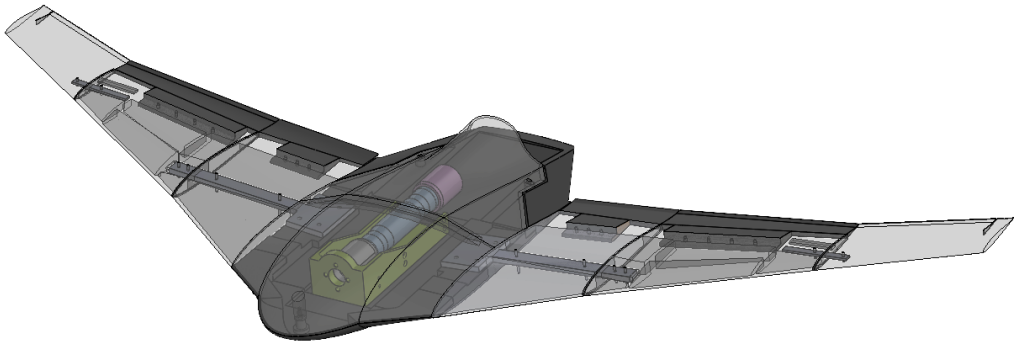

(a) Front view

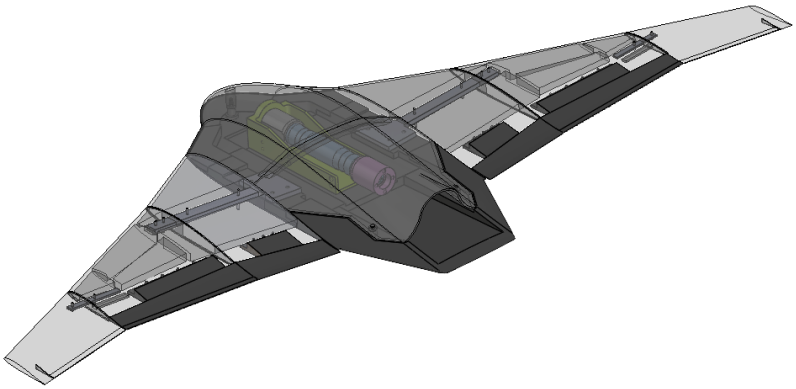

(b) Rear view

Figure 5.2: Green Raven model assembly

In figure 5.2, a detail of the CAD assembly of the Green Raven model is included. Thanks to the modular properties of the model different configurations were tested in order to explore the flying qualities of the UAV. Since the wing is segmented in three pieces, and each piece has a swappable control surface, many different configurations can be obtained. The nine different configurations tested in this campaign are summarized in table 5.2.

Configuration	Movable surfaces setup
0	Base configuration - All surfaces at 0°
1	Inboard flaps at 5°
2	Inboard flaps at 10°
3	Midboard flaps at 5°
4	Midboard flaps at 10°
5	Right winglet at 5°
6	Right winglet at 10°
7	Aileron at 5°
8	Aileron at 10°

Table 5.2: Configurations tested

5.2 Experimental setup

5.2.1 Wind tunnel

All the wind tunnel tests performed for this study were carried out at the L2000 wind tunnel at the Royal Institute of Technology - KTH in Stockholm. The L2000 is a closed test-section closed-circuit wind tunnel. The test section has an octagonal cross-section with 45° fillets, and the dimension are:

Length	$3.5\,m$
Width	$2\,m$
Height	$2\,m$
Cross section	$3.595\,m^2$

Table 5.3: Wind tunnel test section dimensions

The maximum speed that can be reached inside the tunnel is between 60 m/s and 70 m/s. The balance used in the experiments is mounted to an aluminum holder fixed to the bottom part of the central section of the model using eight screws. The mass balance is then mounted to a cylindrical sting that is then fixed to the support of the wind tunnel. Regarding the support where the model is mounted, it consists on a steel trellis frame linked to a moving mechanism, located below the wind tunnel test section, that allows the wind tunnel pilot to perform alpha and beta sweeps during testing.

Figure 5.3: Model mounted on the wind tunnel support - Configuration 0

5.2.2 Balance specifications

The mass balance is a FFAP I-697 and it's a multi-component strain-gauges balance, allowing to record measures of both the forces and moments acting on the UAV. The forces convention for the test setup used is illustrated in the following equation and is graphically represented in figure 5.4:

$$\begin{bmatrix} A_{x_b} \\ A_{y_b} \\ A_{z_b} \end{bmatrix} = \begin{bmatrix} -T \\ -Y_b \\ -N \end{bmatrix} and \begin{bmatrix} A_{x_w} \\ A_{y_w} \\ A_{z_w} \end{bmatrix} = \begin{bmatrix} -D \\ -Y_w \\ -L \end{bmatrix} \tag{5.1}$$

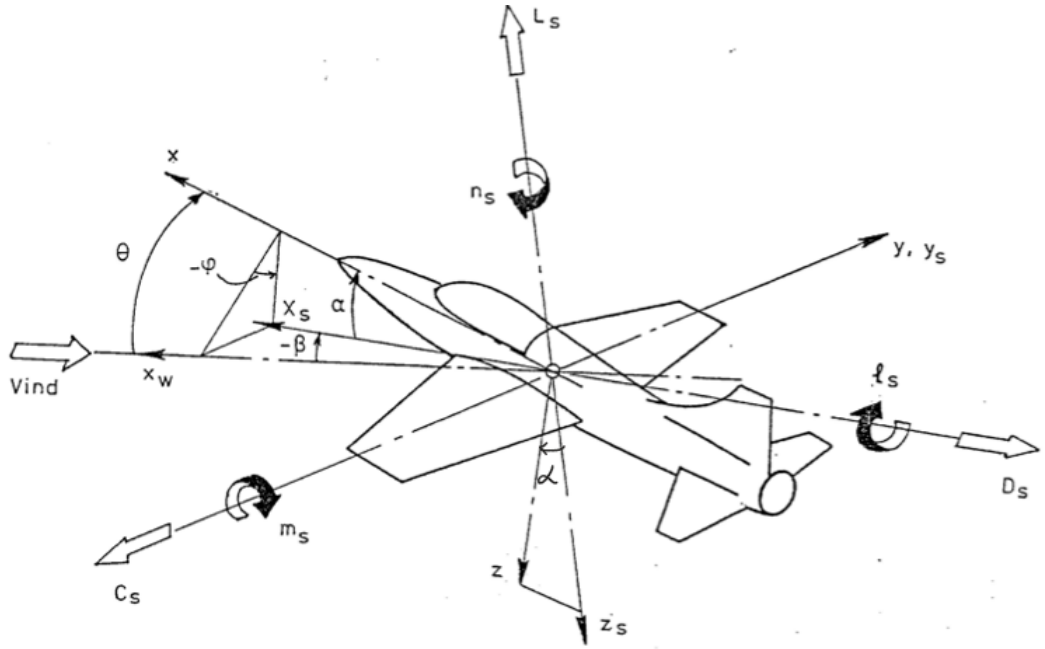

Figure 5.4: Wind axis reference system
[31]

The nominal value for the forces and moments that can be measured are summarized in table 5.4. Note that the side force is indicated by C in the figure, but in this work, it will be referred to as Y.

Forces	Capacity
N	2000 N
C	800 N
T	400 N
m	120 Nm
n	48 Nm
l	120 Nm

Table 5.4: Nominal forces and moments

Forces obtained from the wind tunnel are given in both body (N, Y_b, T) and wind (L, Y_w, D) reference since the acquisition software of the setup is programmed to perform the axis rotation for the forces, while the moments are given only in the body reference systems. Moment transfer calculations are needed in order to take into account the different positions of the balance reference and the model CG and they are performed using equation 5.2, where r_{12} is the distance between the balance reference and the model CG, later expanded in equation 5.3.

$$\boldsymbol{M_m} = \boldsymbol{M_b} - \boldsymbol{r_{12}} \times \boldsymbol{F_b} \tag{5.2}$$

$$\begin{bmatrix} l_m \\ m_m \\ n_m \end{bmatrix} = \begin{bmatrix} l_b \\ m_b \\ n_b \end{bmatrix} - \begin{bmatrix} 0 & -z & y \\ z & 0 & -x \\ -y & x & 0 \end{bmatrix} \begin{bmatrix} -T_b \\ -Y_b \\ -N_b \end{bmatrix} \tag{5.3}$$

5.3 Reynolds matching

Model size choice was influenced by both tunnel section dimension and Reynolds number matching. In a wind tunnel test setup, a proper matching between the Reynolds number of the full-scale aircraft and the reduced-scale model allows having a close resemblance of aerodynamic characteristics, regarding both stall behavior and aerodynamic coefficients. In figure 5.5 a comparison between the Reynolds number of the full-scale and the scaled-down model is included.

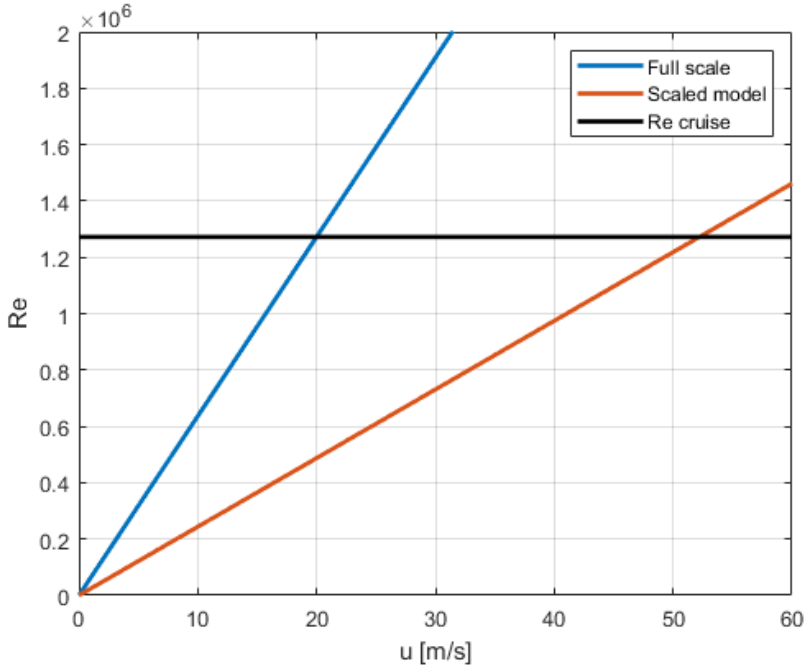

Figure 5.5: Reynolds number matching based on chord lenght

Proper matching for the wind tunnel model is obtained approximately at a speed of 52 m/s. While this speed could be easily accomplished in the wind tunnel, during the model's shake-down testing, the model's behavior at different speeds was studied, and at roughly 40 m/s, some obvious oscillation appeared, raising concerns about the model's structural integrity. As a result, the highest speed obtained throughout the data-gathering phase to avoid any damage to the model was 35 m/s, resulting a in Reynolds of approximately $Re = 8.5276 \cdot 10^5$.

5.4 Test Matrix

The table below provides a broad overview of the test matrix:

Configuration	Test details
0	- α sweep from $-5°$ to $10°$ at $\beta = 0°$ at different tunnel speeds u=20,25,30,40 m/s - α sweep from $-5°$ to $10°$ at $\beta = 0°, 5°, -5°, 10°$ at u=35 m/s - β sweep from $-15°$ to $15°$ at $\alpha = 0°, 5°, 7°$ at u=35 m/s
1	- α sweep from $-5°$ to $10°$ at $\beta = 0°, 5°, -5°, 10°$ at u=35 m/s - β sweep from $-15°$ to $15°$ at $\alpha = 0°, 5°, 7°$
2	- α sweep from $-5°$ to $10°$ at $\beta = 0°, 5°, -5°, 10°$ at u=35 m/s - β sweep from $-15°$ to $15°$ at $\alpha = 0°, 5°, 7°$
3	- α sweep from $-5°$ to $10°$ at $\beta = 0°, 5°, -5°, 10°$ at u=35 m/s - β sweep from $-15°$ to $15°$ at $\alpha = 0°, 5°, 7°$
4	- α sweep from $-5°$ to $10°$ at $\beta = 0°, 5°, -5°, 10°$ at u=35 m/s - β sweep from $-15°$ to $15°$ at $\alpha = 0°, 5°, 7°$
5	- α sweep from $-5°$ to $10°$ at $\beta = 0°, 5°, -5°, 10°$ at u=35 m/s - β sweep from $-10°$ to $10°$ at $\alpha = 0°, 5°, 7°$
6	- α sweep from $-5°$ to $10°$ at $\beta = 0°, 5°, -5°, 10°$ at u=35 m/s - β sweep from $-10°$ to $10°$ at $\alpha = 0°, 5°, 7°$
7	- α sweep from $-5°$ to $10°$ at $\beta = 0°, 5°, -5°, 10°$ at u=35 m/s - β sweep from $-10°$ to $10°$ at $\alpha = 0°, 5°, 7°$
8	- α sweep from $-5°$ to $10°$ at $\beta = 0°, 5°, -5°, 10°$ at u=35 m/s - β sweep from $-10°$ to $10°$ at $\alpha = 0°, 5°, 7°$

Table 5.5: Test condition matrix

Chapter 6

Data correction and stability performances

6.1 Raw data from wind tunnel

The first step of the data analysis consists of extracting the data from the wind tunnel output file using a MATLAB script. The output from the wind tunnel is a .txt file with a single column of numbers where the data needed is stored but unorganized. Starting from a script that was kindly provided by SAAB and with some accurate adjustments it was possible to get an organized output consisting of:

- Angle of attack (α), side-slip angle (β) and dynamic pressure (q).
- Forces and moments in body reference axis (N, T, Y_b, l, n, m).
- Forces in air reference axis (L, D, Y_w).
- Aerodynamic coefficient of forces and moments ($C_L, C_D, C_{Y_W}, C_l, C_m, C_n$).

From this data, a preliminary performance analysis can be performed by plotting the raw coefficient against either α or β based on the test that's being considered. An example of the curves obtained from the uncorrected, "raw", coefficients is depicted in figure 6.1 and 6.2. It's important to notice that during data acquisition both the upward and downward motion of the model and side-to-side motion, respectively for α and β sweep, are considered, in order to take into account possible hysteresis effects on the measures.

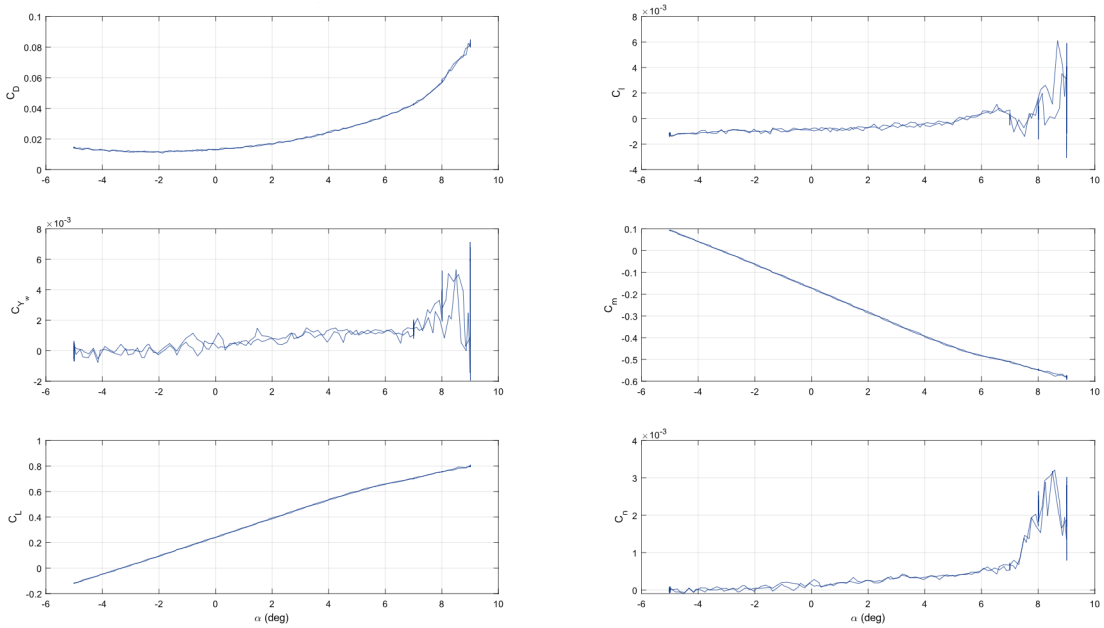

Figure 6.1: Aerodynamic coefficient vs α - Configuration 0 at u=35m/s

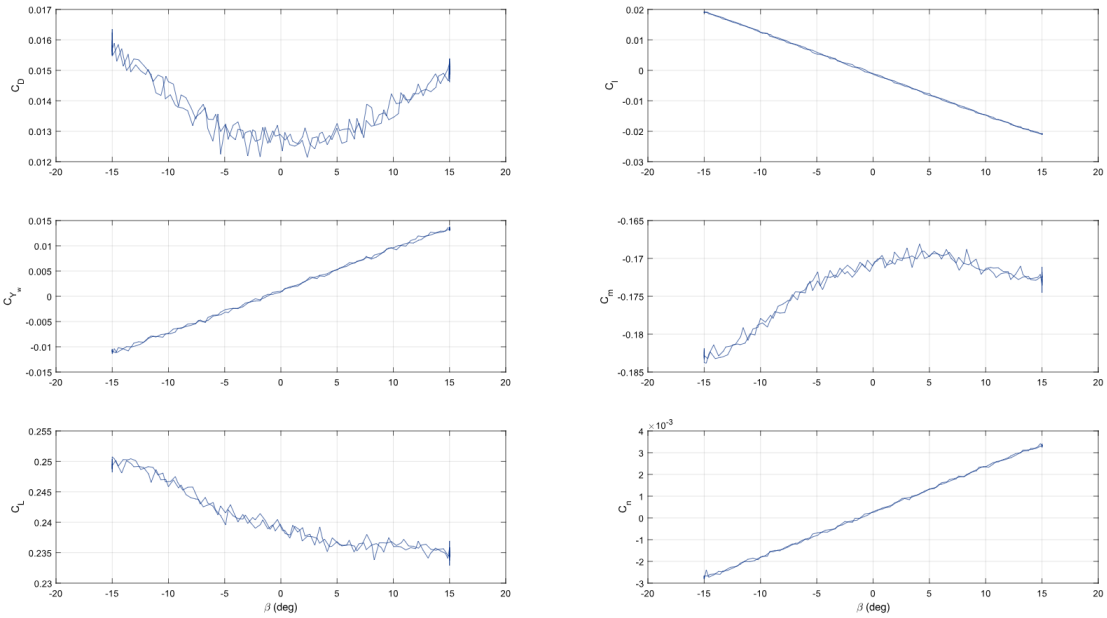

Figure 6.2: Aerodynamic coefficient vs β - Configuration 0 at u=35m/s

The data reduction process in which all the corrections will be applied is performed only in the ascending part of the data acquired.

6.2 Corrections coefficients

In the following section, the correction coefficients described in chapter 3 are calculated for the test setup used. The model is considered as a wing since it's a BWB, which is made up of many airfoil sections.

6.2.1 Blockage corrections

Given a test section, solid blockage is constant and it's unaffected by speed and angle of attack. It can be calculated by using equation 3.1 in which K_1 is estimated by averaging the thickness-to-chord ratio t/c throughout the span of the model, as illustrated in table 6.1.

Airfoil	t/c%	% of total span
MH104	15.28	20
MH61	10.24	80
weight averaged	11.26	100

Table 6.1: Average chord estimation

No specific data regarding K_1 for MH series airfoils is available, hence, table 3.2 with data regarding 4 digits NACA airfoils was used, resulting in $K_1 = 1.004$. The τ_1 value is obtained considering the span-to-tunnel-breadth ratio of 0.75, the ratio $B/H = 1$, hence, from figure 3.3, $\tau_1 = 0.85$. Wake blockage was calculated using equation 3.2, with the assumption that most of the flow stays attached, allowing the second part of the equation to be neglected and the wake blockage coefficient ε_{wb} to be constant during the test. In order to evaluate ε_{wb}, $C_{D,0}$ needed to be determined, and it was done by using Maskell's correction method [32] that consists on considering the minimum value of $C_{D,u}$ as $C_{D,0}$. Table 6.2 summarizes the parameters used to calculate the solid and wake blockage coefficients.

Parameter	Value
Tunnel cross-section area C	3.595 m^2
Model volume V	0.0116 m^3
Zero-lift drag coefficient $C_{D,0}$	0.0114
Shape factor K_1	1.004
Tunnel shape factor τ_1	0.85

Table 6.2: Parameter for solid and wake blockage evaluation

The total blockage coefficient can be calculated by summarizing solid and wake blockage coefficients as indicated in equation 3.2.2. Table 6.3 contains the values obtained for the solid and wake blockage. With the total blockage coefficient, the corrected value of the dynamic pressure q_c and the aerodynamic coefficients in equation 3.4 are obtained. Since the Green Raven UAV has no tail, no downwash effect on the tail can affect the pitching moment coefficient, hence its correct value can be determined as the other coefficients in equation 3.2.2. The angle of attack and drag coefficient need further corrections.

Solid blockage ε_{sb}	0.0015
Wake blockage ε_{wb}	0.00032
Total blockage ε_{tot}	0.0018

Table 6.3: Blockage coefficents

6.2.2 Downwash corrections

Downwash corrections are applied to both AOA and drag coefficient as an increment of α and C_D respectively. They are calculated with equations 3.5 and 3.9, in which only the value of the boundary correction factor δ needs to be determined. Following the procedure described in section 3.3, the values needed to calculate δ are listed in table 6.4

Parameter	Value
Vortex span ratio b_v/b	0.7
Effective vortex span b_e	1.275
Vortex span to tunnel width ratio k	0.6375
Boundary correction factor δ	0.113

Table 6.4: Parameters for δ evaluation

6.2.3 Flow angularity corrections

Details on the procedure followed to determine flow angularity corrections are illustrated in appendix A. AOA correction is calculated as an increment $\Delta\alpha_{ang}$ while the correction on the drag coefficient, expressed in equation A.12, is applied as an increment $\Delta C_{D,ang} = C_{L,c}\, tan\alpha$ using only the second term of equation A.12. Values of $\Delta\alpha_{ang}$ and $tan\alpha$ calculated at different air speeds are listed in table A.3 and A.4, respectively.

Air speed [m/s]	$\Delta\alpha_{ang}$ [deg]
10	0.287
15	0.381
20	0.421
25	0.493
30	0.473
35	0.426
40	0.498

Table 6.5: Average value of $\Delta\alpha$

Air speed [m/s]	$tan\,\alpha$
10	0.01
15	0.0117
20	0.0189
25	0.00923
30	0.009
35	0.0091
40	0.0097

Table 6.6: $tan\,\alpha$ values at different speeds

Since no data about the longitudinal pressure gradient of the wind tunnel, the buoyancy correction on the drag coefficient was not applied. In order to summarize, the corrected values of α and C_D are expressed in the following equations:

$$\alpha_c = \alpha_u + \Delta\alpha_{up} + \Delta\alpha_{ang} \tag{6.1}$$

$$C_{D,c} = C_{D,u} + \Delta C_{D,up} + \Delta C_{D,ang} \tag{6.2}$$

6.3 Uncorrected and corrected data comparison

In this section, a comparison between the corrected and uncorrected aerodynamic coefficients for configuration 0 (baseline configuration, all control surfaces at 0°) is given. From now on, the subscript $_c$ will indicate the corrected value while $_u$ will indicate uncorrected values. Figures 6.3, 6.4 and 6.5 show corrected and uncorrected values of C_L, C_D and C_m vs α, respectively. The curve of corrected values is plotted by using both the corrected value of the coefficient and the AOA. Thus, from the images, it's possible to see the overall result of these corrections. Regarding the lift coefficient, it can be seen that the curve is slightly shifted towards the right, meaning that for a given value of α the uncorrected value of C_L is higher than the corrected one. Also, the corrected curve has a smaller slope and, combining this with the shift of the curve, results in a greater difference between corrected and uncorrected values at high AOA.

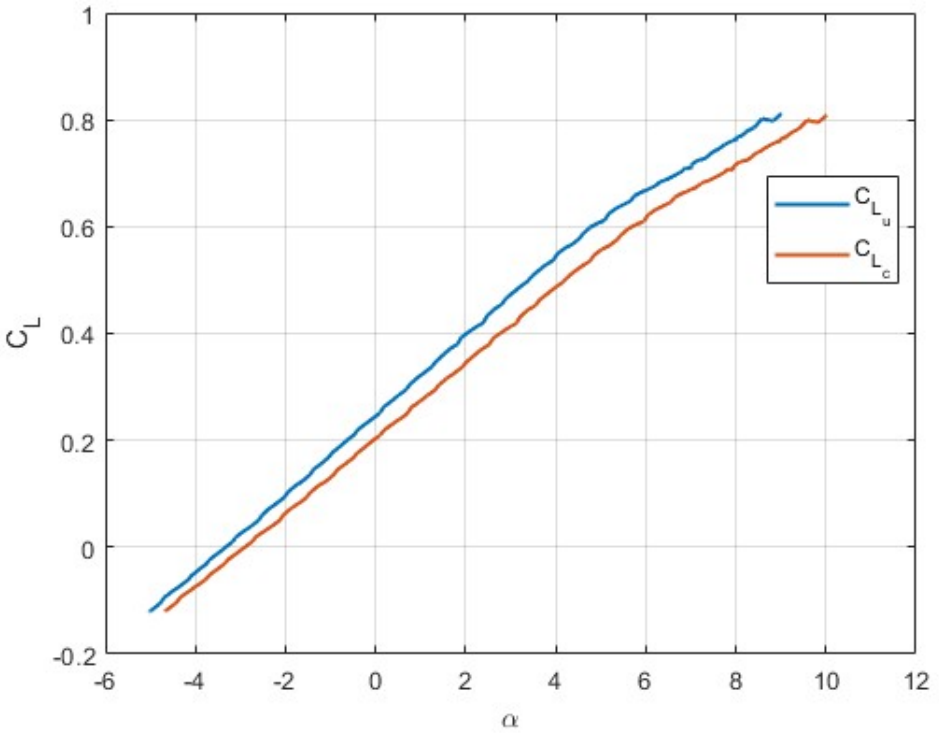

Figure 6.3: C_L vs α - Configuration 0 at u=35m/s

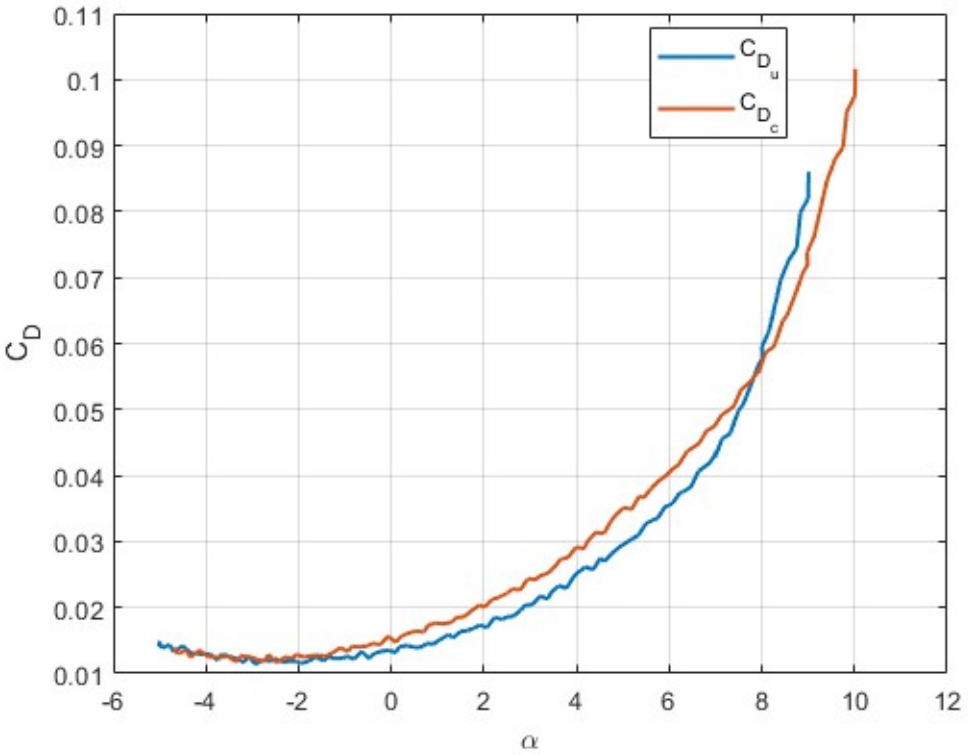

Figure 6.4: C_D vs α - Configuration 0 at u=35m/s

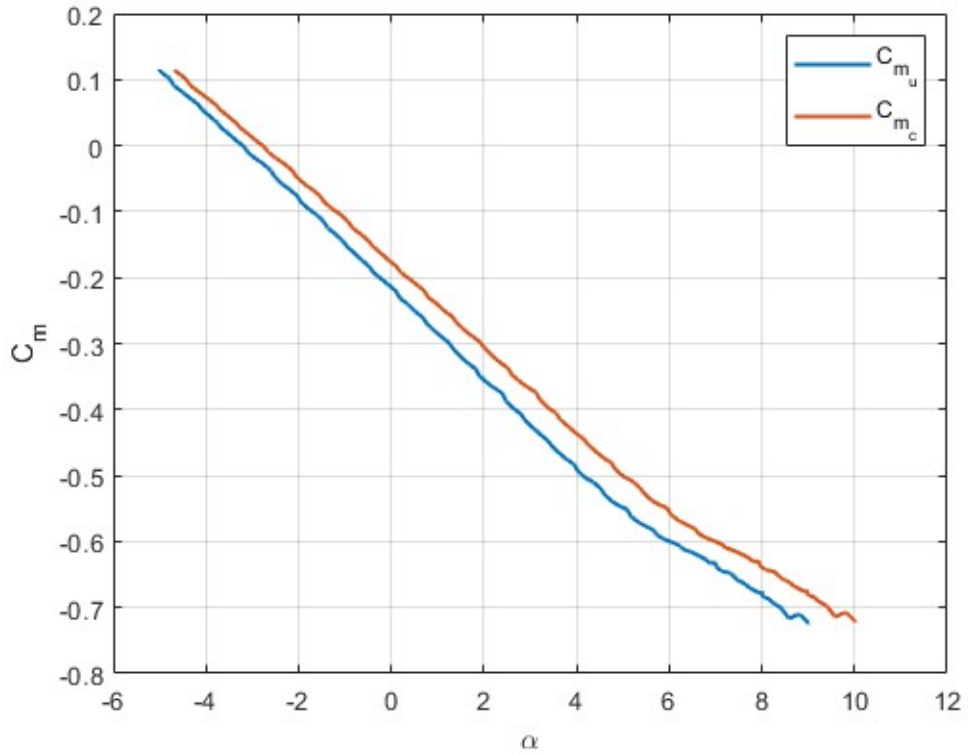

Figure 6.5: C_m vs α - Configuration 0 at u=35m/s

In terms of drag coefficient, from the graph of figure 6.4, it's possible to see that the curve's concavity changes since the corrected curve has a smaller concavity than the uncorrected one. Also, the corrected values curve is slightly shifted to the right. The result is that up to an AOA of 8°, corrected values of the drag coefficient are greater than the uncorrected one, while for bigger AOA are smaller.

Regarding the pitching moment coefficient, it can be seen that similarly to lift coefficient curves, the corrected values of C_m are slightly shifted towards the right and there's a small change in slope, the corrected curve having a smaller slope. The overall result is that, for a given value of α, the corrected pitching moment coefficient is greater than the uncorrected one, with the difference between the two being greater at higher AOA.

In figures 6.6, 6.7 and 6.8 corrected and uncorrected values of respectively C_l, C_n and C_{Y_w} vs β are illustrated. From these figures it's difficult to grasp the difference between the corrected and uncorrected values since they are quite close. For this reason in figure 6.9 the difference (Δ) between corrected and uncorrected values of C_l, C_n and C_{Y_w} vs β is indicated. From this figure, it's evident that the greater the yaw angle, both with positive and negative signs, the greater the difference between corrected and uncorrected values. Also, a slight asymmetry can be seen from figure 6.9as the minimum difference point isn't perfectly centered at $\beta = 0$, probably because of small setup misalignment.

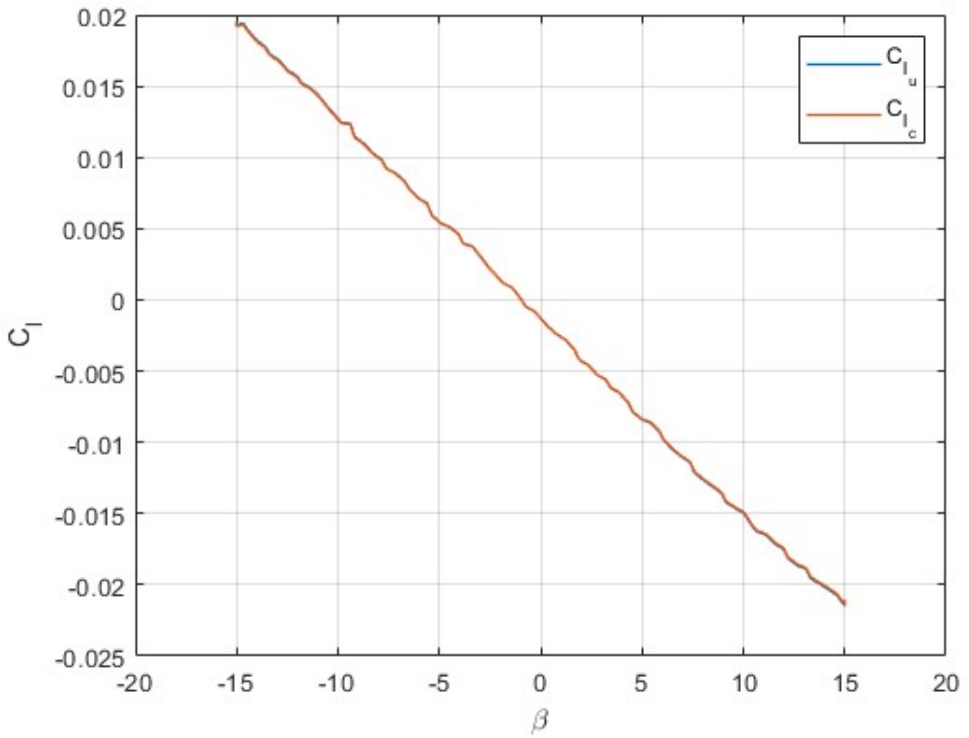

Figure 6.6: C_l vs β - Configuration 0 at u=35m/s

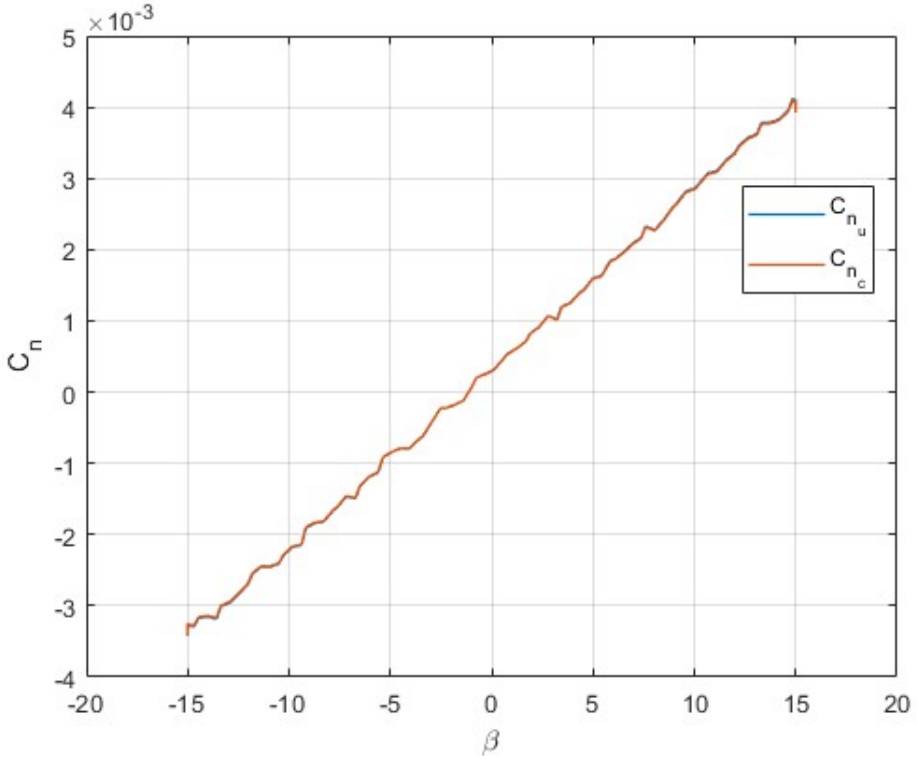

Figure 6.7: C_n vs β - Configuration 0 at u=35m/s

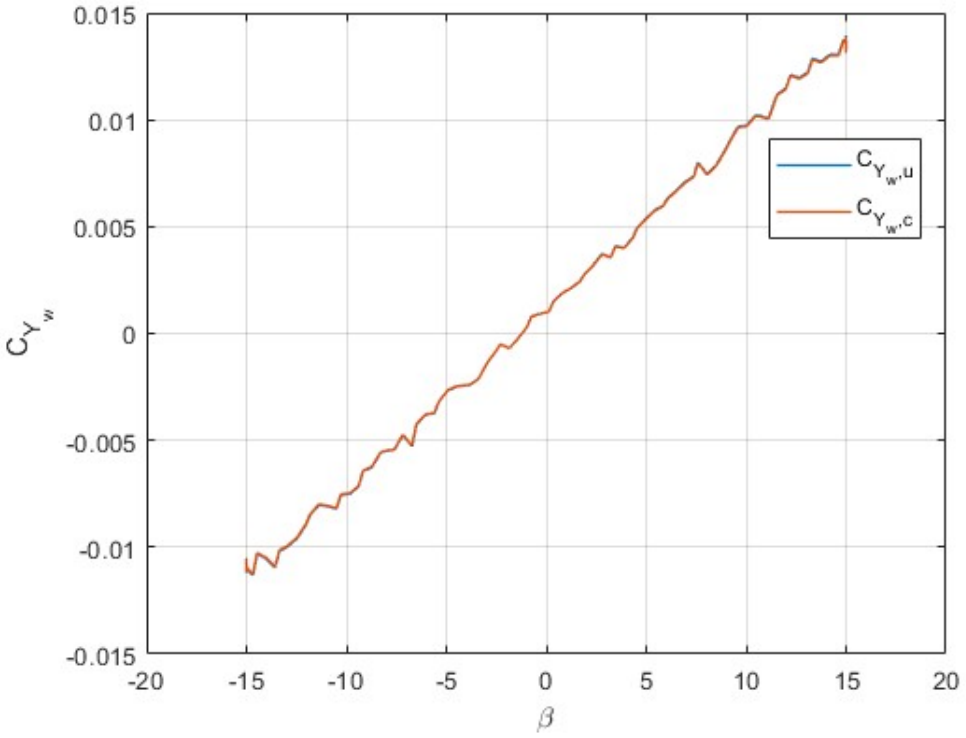

Figure 6.8: C_{Y_w} vs β - Configuration 0 at u=35m/s

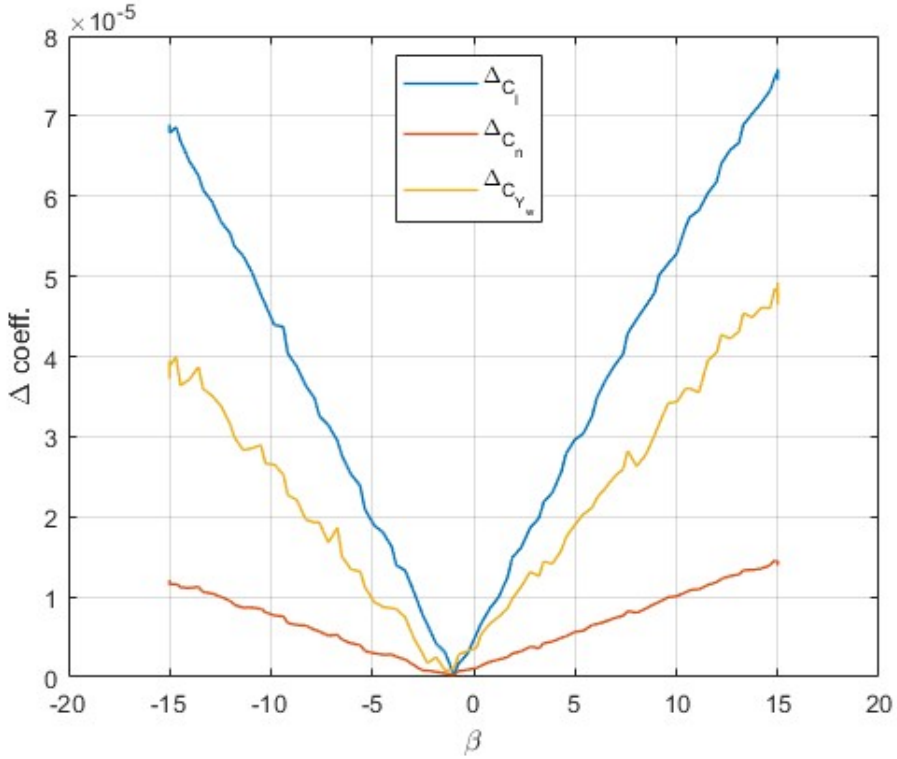

Figure 6.9: Difference between corrected and uncorrected values - Configuration 0 at u=35m/s

The magnitude of corrections on the lateral-dynamic coefficients (C_l, C_n, C_{Y_w}) is small as these values are only affected by the correction regarding blockage effects. The longitudinal-dynamic coefficients (C_L, C_D, C_m) instead, since they are influenced by flow-angularity, downwash, and blockage effects, show a greater difference between corrected and uncorrected values, resulting in a lower lift and higher resistance coefficient overall at a given AOA. This trend is maintained for configuration 0 at the different air speeds that it was tested and also for the other configurations tested at $u = 35m/s$.

In figure 6.10 the aerodynamic efficiency (L/D ratio) vs α is illustrated. The maximum value of E_c is 17.73 while $E_u = 23.86$ meaning that the uncorrected values over-predict the aerodynamic efficiency by 34.6%. Overall a general reduction of aerodynamic efficiency is obtained after applying the corrections.

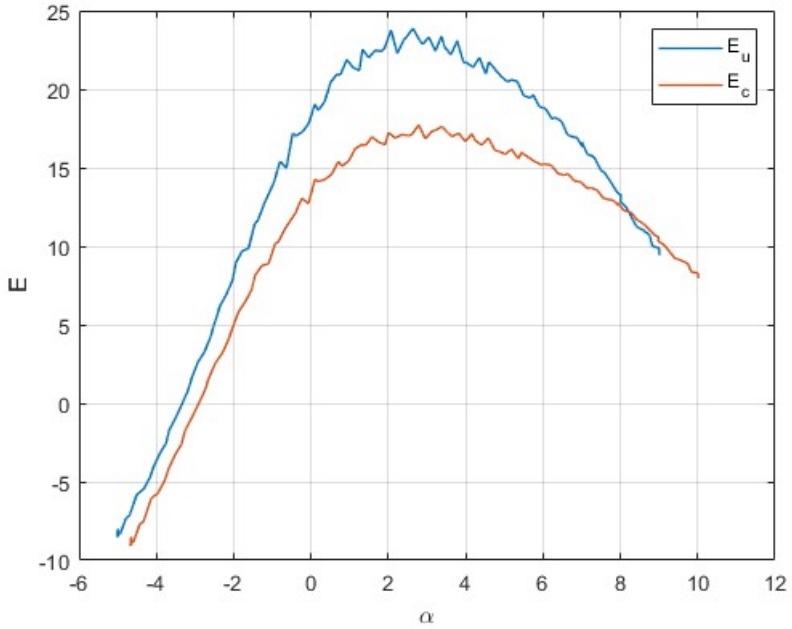

Figure 6.10: Aerodynamic efficiency vs α - Configuration 0 at u=35m/s

This trend of uncorrected wind tunnel values over-estimating the UAV aerodynamic performances is also highlighted in figure 6.11 by the C_L vs C_D, where most of the corrected curve is beneath the uncorrected one.

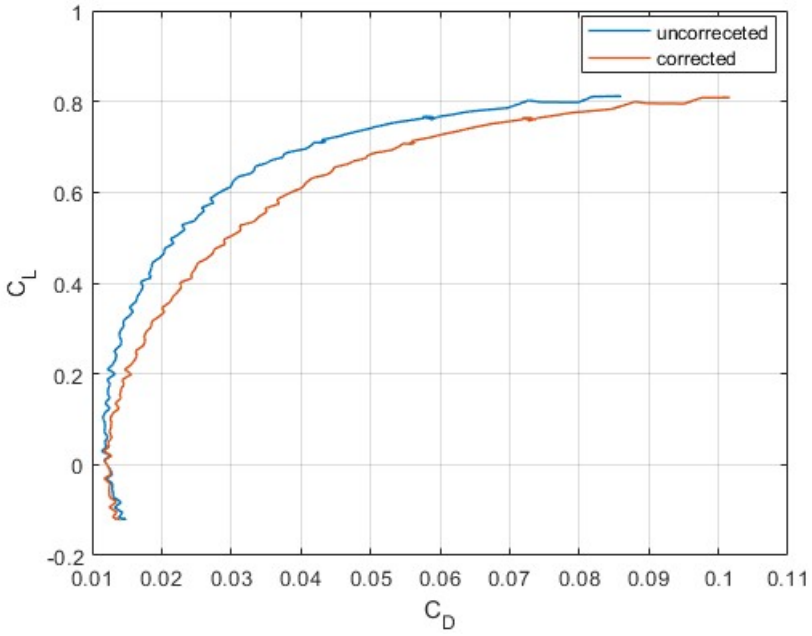

Figure 6.11: C_L vs C_D - Configuration 0 at u=35m/s

6.4 Aerodynamic coefficients analysis

In the following table, a resume of the aerodynamic coefficients of the Green Raven scaled model obtained from wind tunnel testing is included.

C_{L_0}	0.2
C_{L_α}	0.0651
C_{D_0}	0.0124
C_{D_α}	0.0019
C_{m_0}	-0.1721
C_{m_α}	-0.0587
$C_{Y_{w0}}$	0.0011
$C_{Y_{w\beta}}$	0.0008
$C_{Y_{w\delta_a}}$	-2.4028 $\cdot 10^{-4}$
C_{l_0}	-0.0011
C_{l_β}	-0.0014
$C_{l_{\delta_a}}$	0.0017
C_{n_0}	$0.5255 \cdot 10^{-3}$
C_{n_β}	$0.248 \cdot 10^{-3}$
$C_{n_{\delta_a}}$	-8.5512 $\cdot 10^{-5}$

Table 6.7: Green Raven aerodynamic coefficients - Scaled model

From the data gathered in this table, an overview of the stability performances of the UAV can be obtained. From the pitching moment coefficient, since both C_{m_0} and C_{m_α} are negative, longitudinal static stability is achieved without a stable flight at cruise AOA. With the exception of the C_{m_0}, all the other $_0$ coefficients have near zero values, meaning that a balanced flight at cruise speed can be achieved with a proper correction on the pitching moment. When considering lateral directional static stability, specific requirements come into play: a positive C_{n_β} and a negative C_{l_β} and $C_{Y_{w\beta}}$. A careful examination of the table reveals that the criteria for roll and yaw derivatives are met, whereas the one for the side force is not. In reality, due to the reference system employed in the wind tunnel setup, where the side force is treated as positive in the direction exiting the left wing, rather than the right (as illustrated in Figure 5.4), the requirement for $C_{Y_{w\beta}}$ in this particular case is to have a positive value, thus also being satisfied.

6.4.1 Effects of airspeed and yaw angle on configuration 0

In figures 6.12, 6.13, 6.14 and 6.15 a comparison between the data gathered at the different speed and yaw angles β for configuration 0 is shown. From these graphs, it's evident that the change in speed and yaw angle does not affect performances in a noticeable way. Since the maximum AOA achieved in these tests was $\alpha = 10°$, the effect of stall at different speeds couldn't be captured. This effect would require a higher AOA during the test or employing trip strips in order to anticipate the aerodynamic stall of the wing.

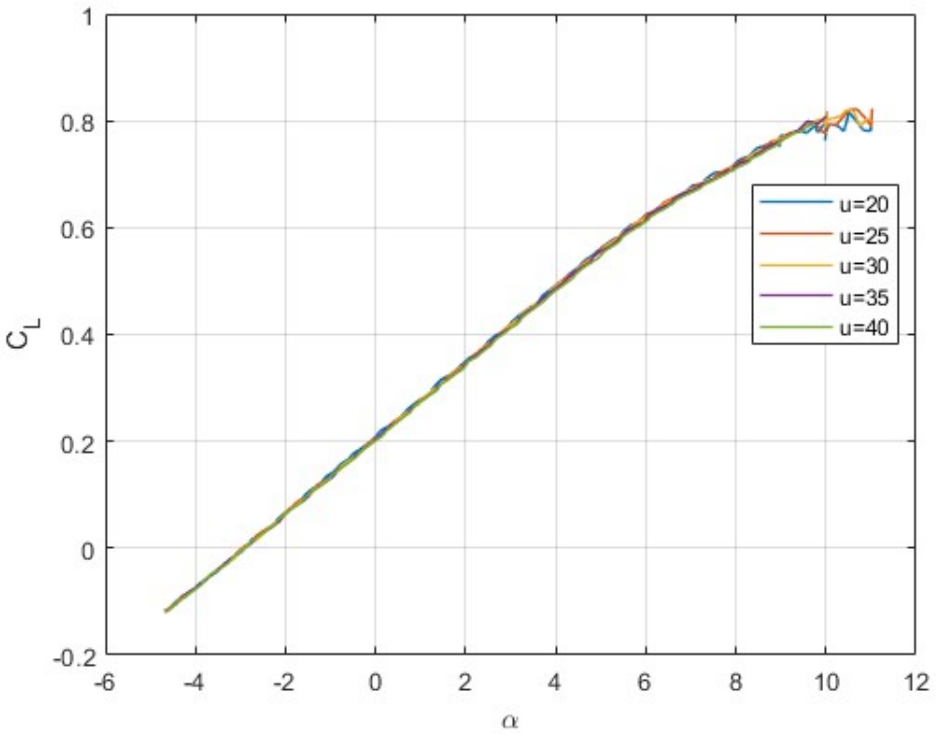

Figure 6.12: C_L vs α - Configuration 0 at different speeds

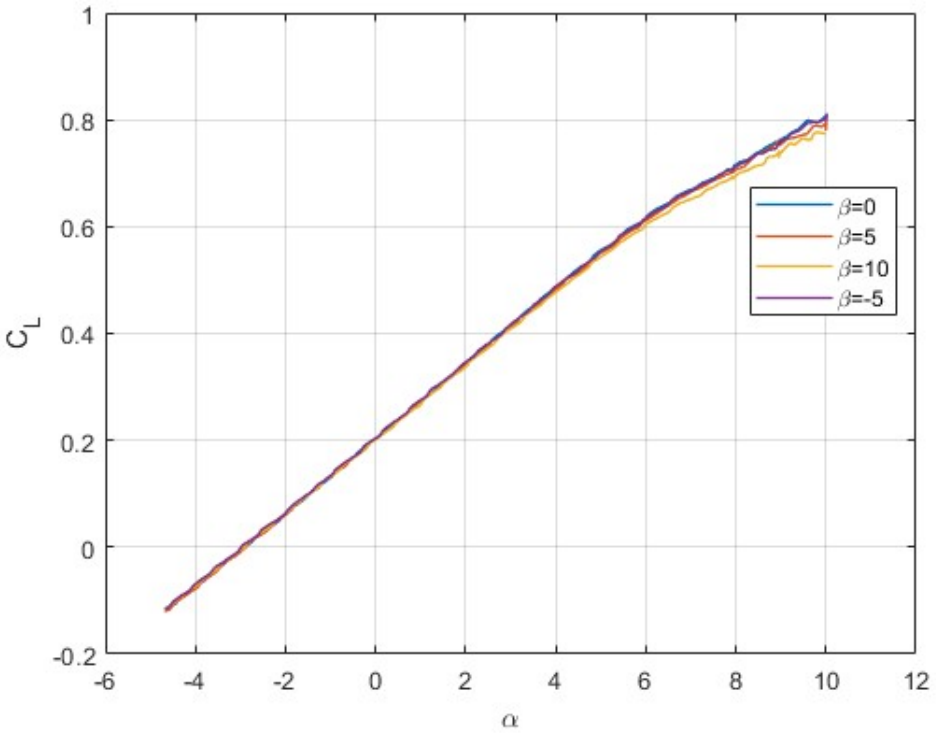

Figure 6.13: C_L vs α - Configuration 0 at different *beta*

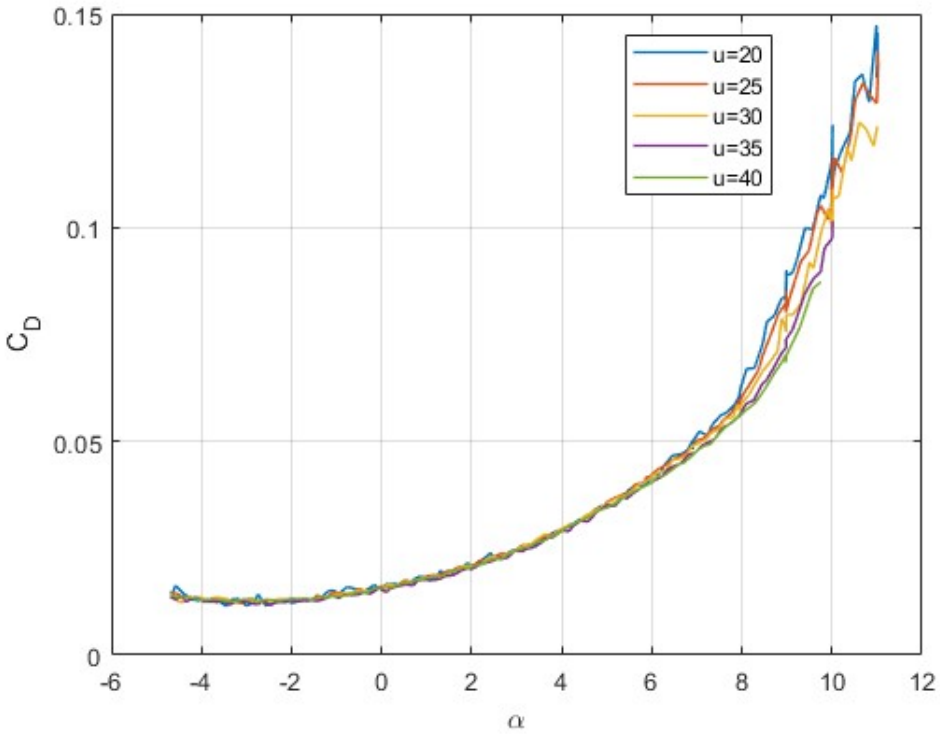

Figure 6.14: C_D vs α - Configuration 0 at different speeds

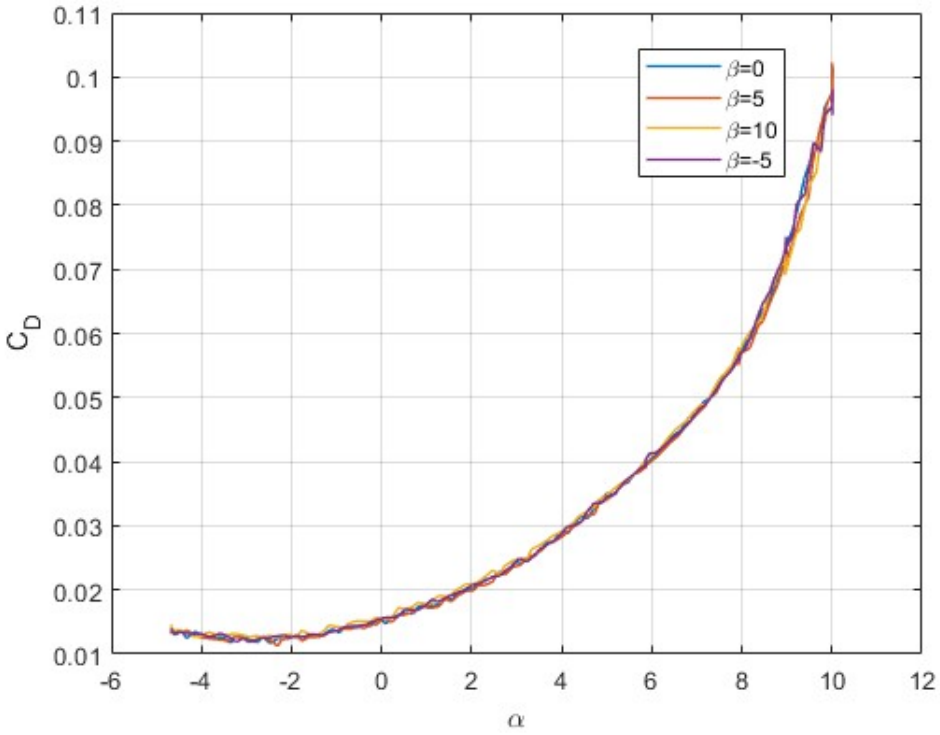

Figure 6.15: C_D vs α - Configuration 0 at different β

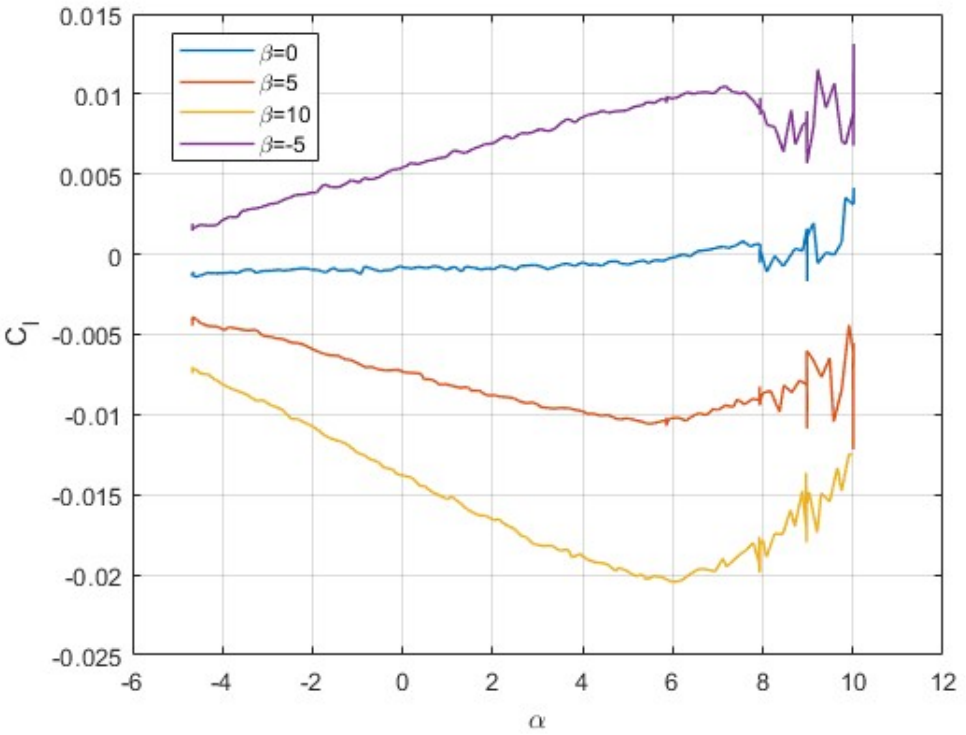

Figure 6.16: C_l vs α - Configuration 0 at u=35m/s

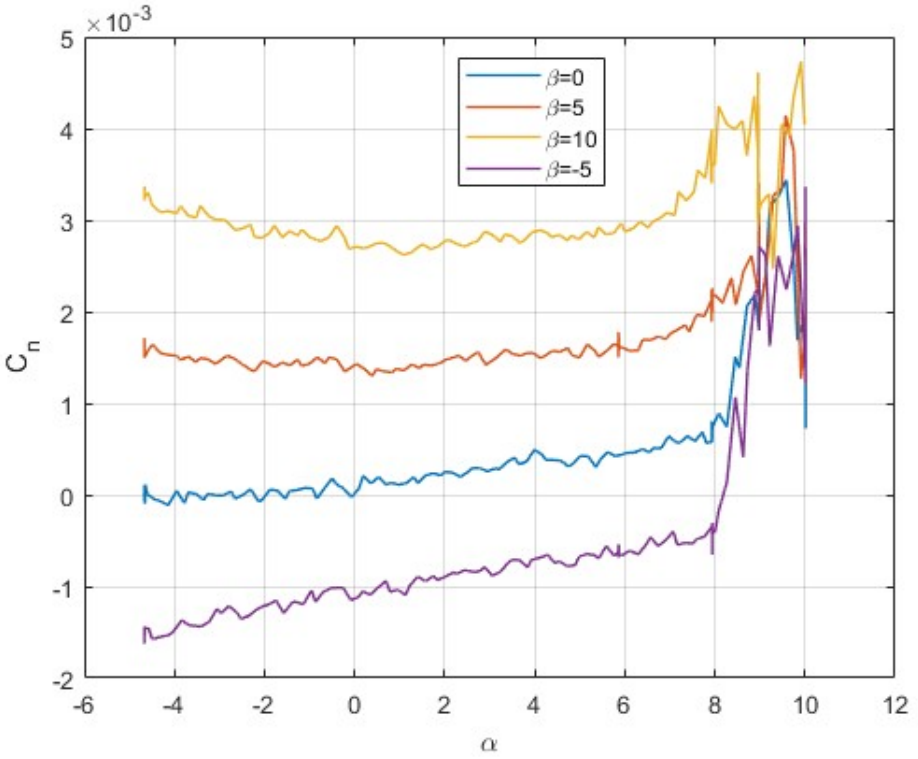

Figure 6.17: C_n vs α - Configuration 0 at u=35m/s

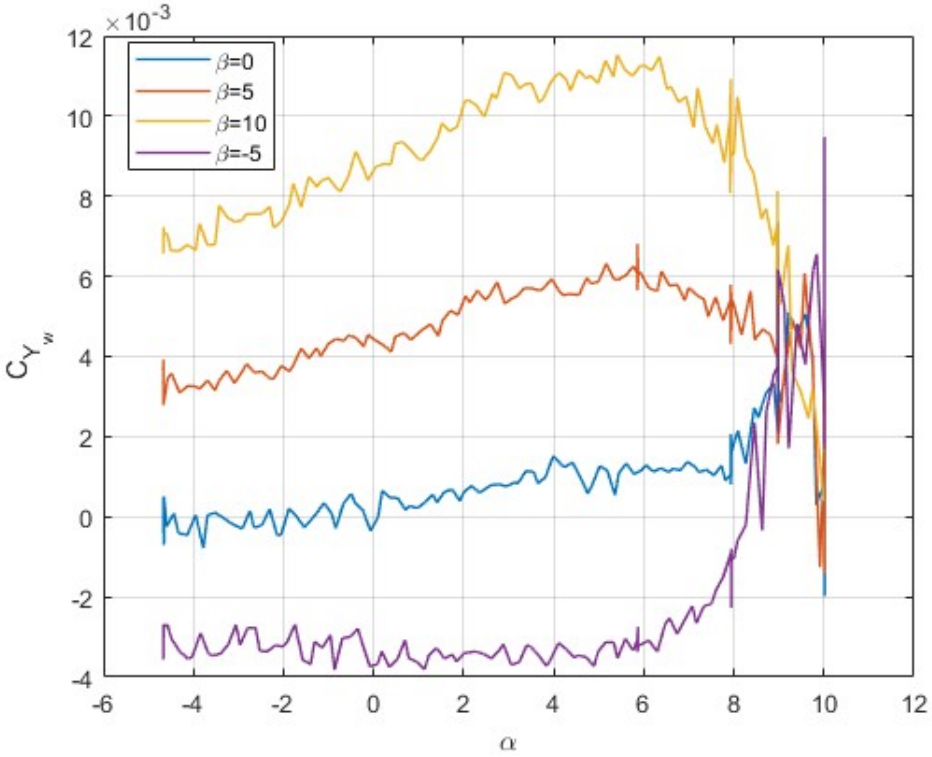

Figure 6.18: C_{Y_w} vs α - Configuration 0 at u=35m/s

In figures 6.16, 6.17 and 6.18 the rolling moment, the yawing moment, and the side-force coefficient vs α are illustrated for the different β angles tested. The effect of sideslip angle on lateral/directional forces and moments is highlighted. By comparing data from tests at $\beta = 5°$ and $\beta = -5°$ it's possible to see that a good degree of symmetry is present across the three different coefficients. For C_n and C_{Y_w} data at high angles of attack is affected by great fluctuations, since the forces are quite small, caused by vibrations of the model. It's also noticeable that for $\beta = 0°$ the coefficients maintain a near zero value up until the effect of vibration at high angles of attacks emerges.

In figures 6.20, 6.19 and 6.21 the rolling moment, the yawing moment, and the side-force coefficient vs β are illustrated for the different α angles tested. From figure 6.20 the discrepancy between the different angles of attack is clearly visible, a noticeable increase in slope can be observed between the $\alpha = 0°$ and $\alpha = 5°$ test while the $\alpha = 5°$ and $\alpha = 7°$ curves are quite similar, due to the fact the change in AOA is limited. Regarding the yawing moment and side force coefficient, the variation between each AOA tested is narrow.

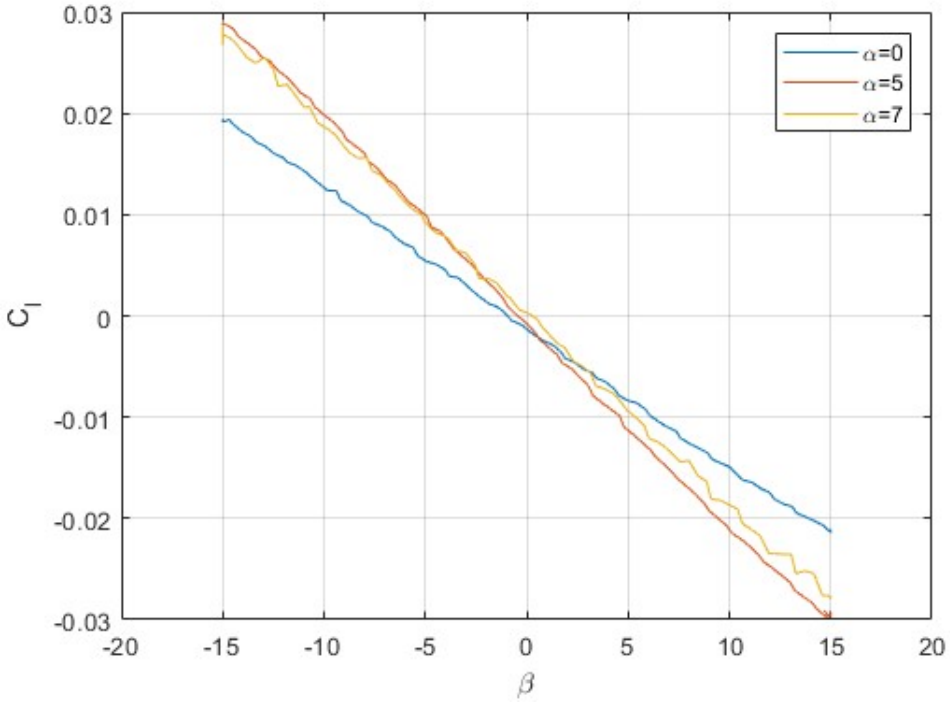

Figure 6.19: C_l vs β - Configuration 0 at u=35m/s

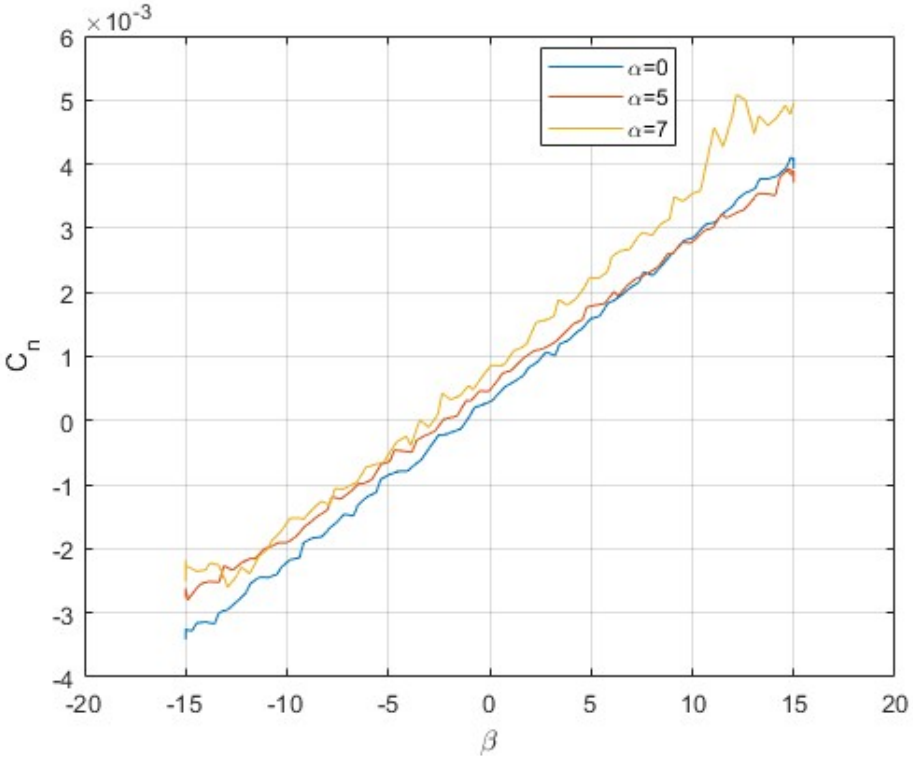

Figure 6.20: C_n vs β - Configuration 0 at u=35m/s

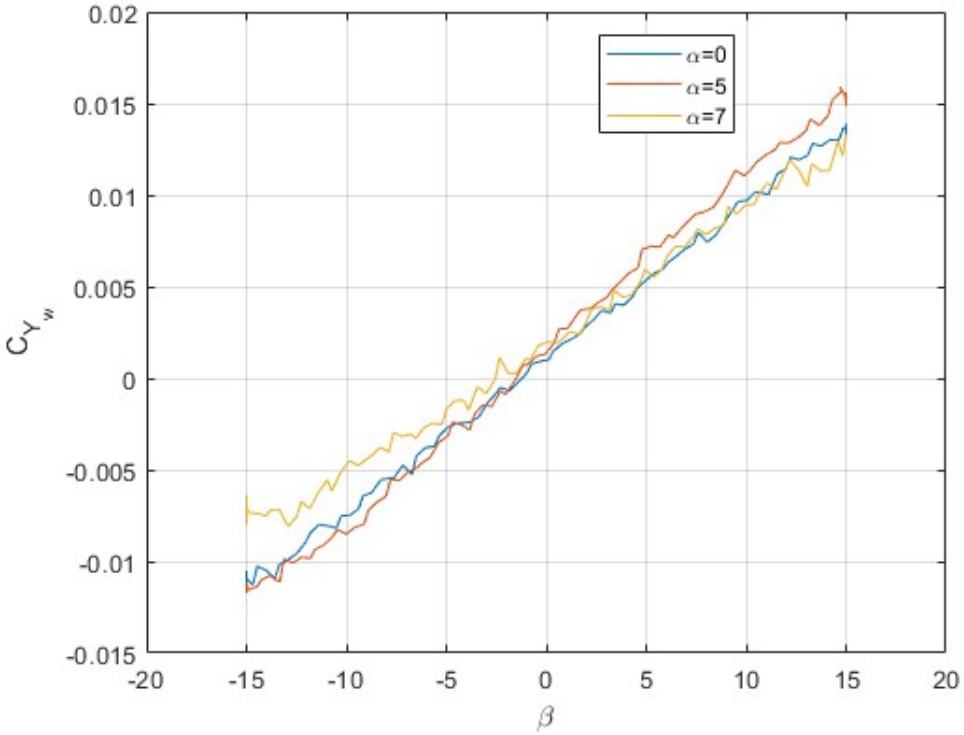

Figure 6.21: C_{Y_w} vs β - Configuration 0 at u=35m/s

6.4.2 Effects of flaps

In figure 6.22, 6.23, and 6.24 a comparison between configuration from 0 to 4 is carried out for the lift, drag, and pitching moment coefficient. As described in table 5.2 configuration 1 to 4 feature flap in either the inboard or midboard section of the wing at 5° or 10° angle. From figure 6.22 it's possible to see that all of the four configurations with flaps provide a higher lift coefficient overall compared to the baseline configuration (Configuration 0). At low AOA Configuration 1,2 and 3 present similar values of C_L while at higher AOA the configuration with flaps at 5° have close values of lift coefficient. This is also valid for flaps at 10°, configuration 2 and 4 have similar values of C_L at high AOA while for low AOA the lift coefficient of configuration 4 is significantly higher.

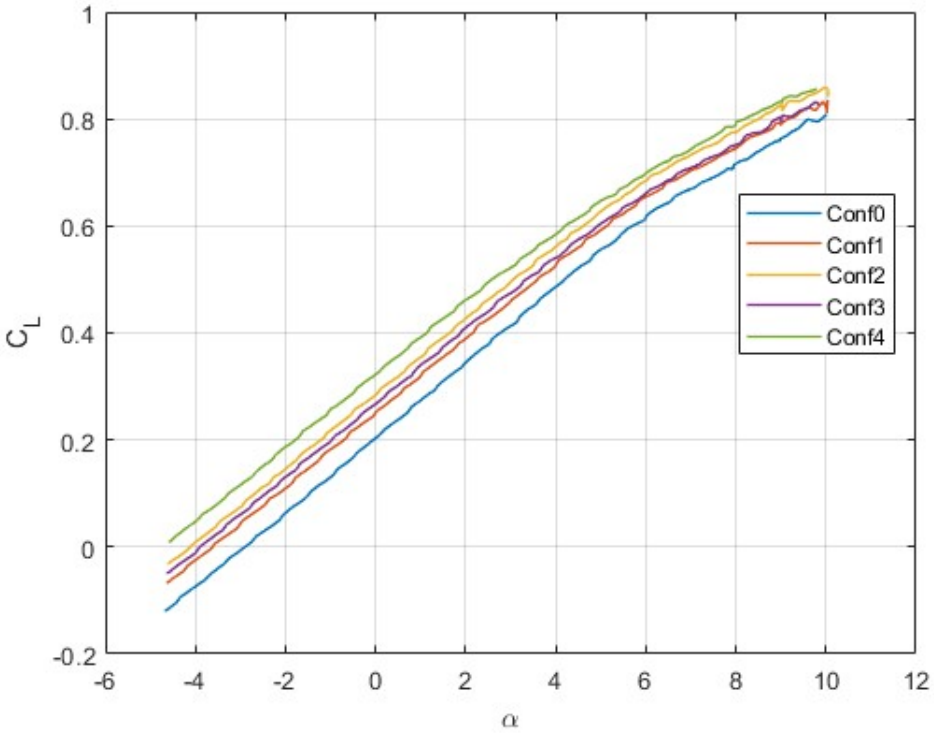

Figure 6.22: C_L vs α - Effect of flaps

Noticeable effects on the drag coefficient are also highlighted in figure 6.23, where it can be seen that all configurations display a higher drag at low AOA compared to the baseline configuration. Among the configuration featuring flaps, configuration 4 has the highest drag overall while configuration 1 has the lowest. Configurations 2 and 3 present a similar C_D in the range of AOA tested. Regarding the pitching moment coefficient, as shown in figure 6.24, it's possible to see that all the configurations feature a lower C_m overall compared to the baseline configuration, while the curves display no appreciable difference in slope.

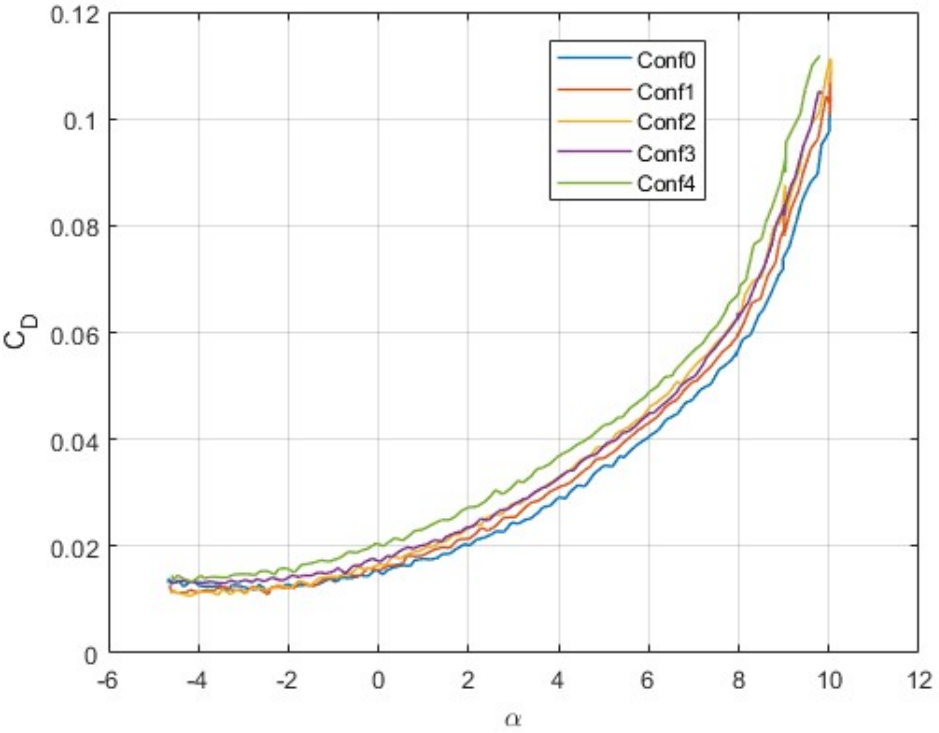

Figure 6.23: C_D vs α - Effect of flaps

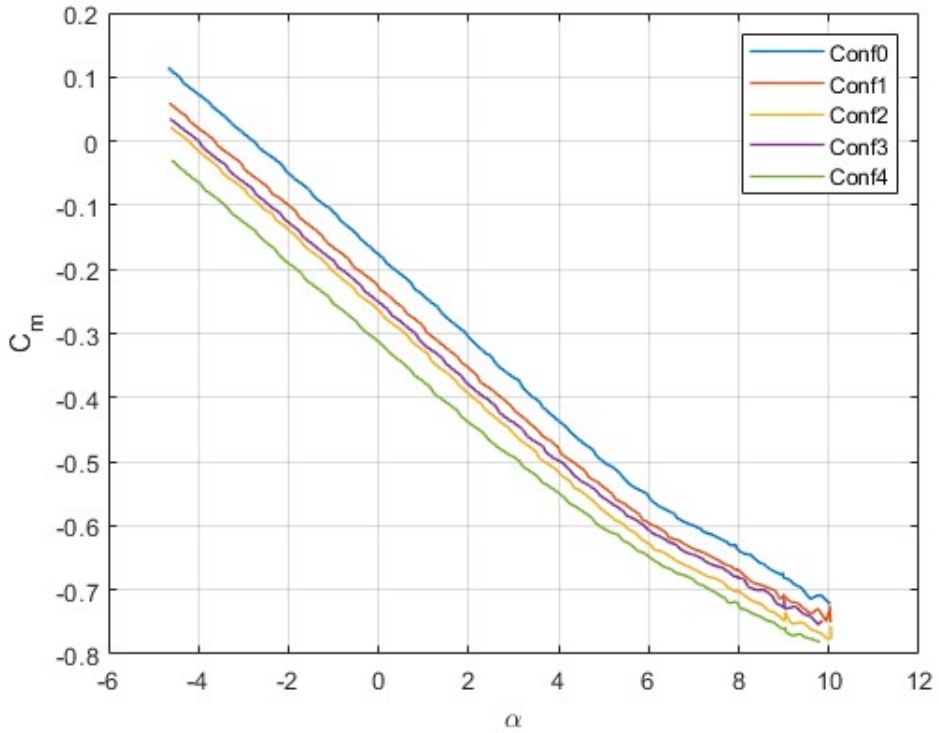

Figure 6.24: C_m vs α - Effect of flaps

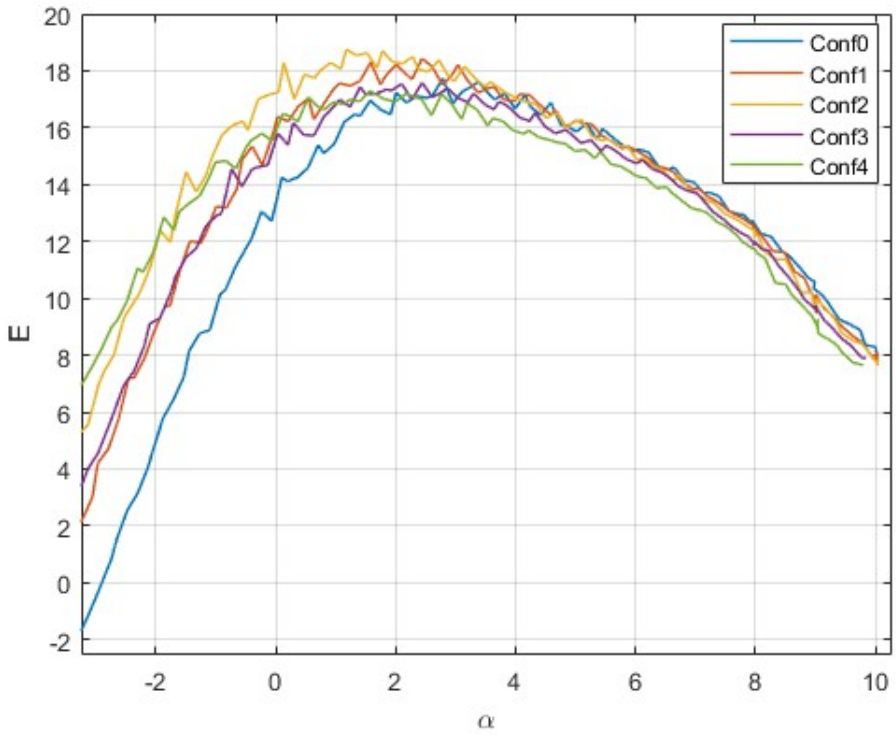

Figure 6.25: E vs α - Effect of flaps

Figure 6.25 shows a plot of the aerodynamic efficiency vs α for the different configurations featuring flaps. It's possible to see that configuration 2 presents the maximum efficiency for low AOA up to $\alpha = 4°$, while for higher AOA configuration 0 has the best overall efficiency. While configuration 4 generates the maximum lift, the efficiency gap between it and configuration 2 is significant at low AOA, but diminishes as AOA increases. Overall, at increasing AOA the difference in efficiency among the different configurations decreases. Based on these results, configuration 2 appears to be the most suited when there's a need to increase lift without a considerable increase of drag, while configuration 4 can be used for example at take-off or landing when maximum lift achievable is needed.

6.4.3 Effects of ailerons

In figure 6.26, 6.27, and 6.28 the effect of aileron angle on C_l, C_n, C_{Y_w} vs α respectively is shown. As mentioned previously, configurations 7 and 8 feature an aileron angle of 5° and 10° respectively, with the right side control surface moved upward and the left side downward. For this reason, a positive rolling moment (right wing down) is generated as can be seen from figure 6.26, from which is also evident that from an AOA of 4° the C_l decreases, especially in configuration 8, indicating that probably the outer section of the wing is starting to stall. At the same time, a negative yawing moment (nose left) called aileron adverse yaw is present, as can be seen from figure 6.27. Also, from figure 6.28 it's possible to see that for configuration 8 a slight side force is present, while for configuration 7 it's almost negligible.

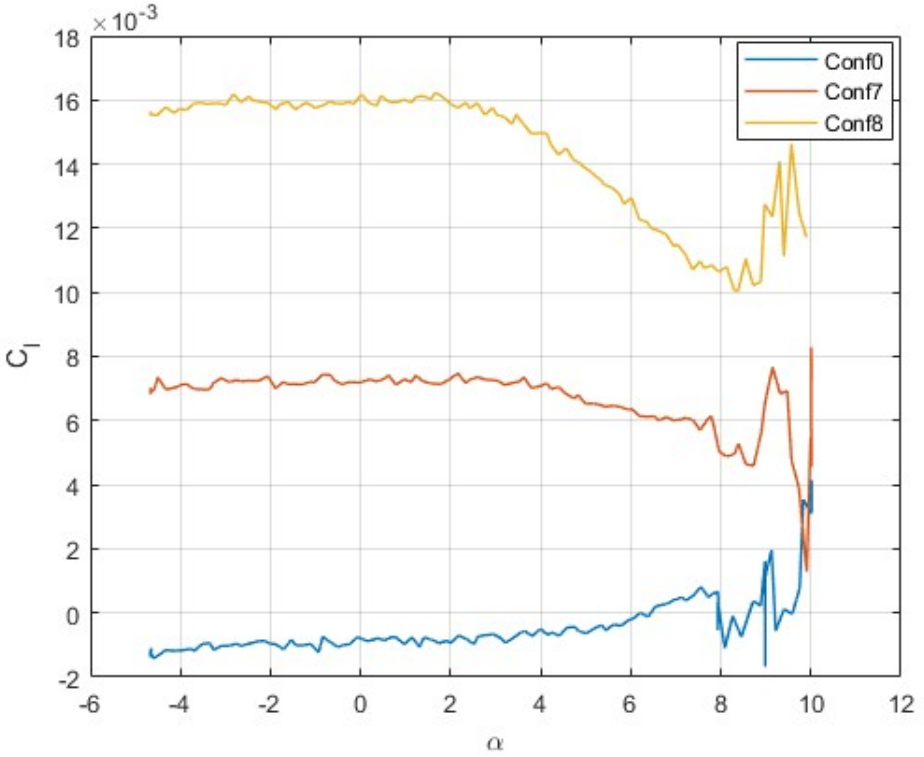

Figure 6.26: C_l vs α - Effect of aileron

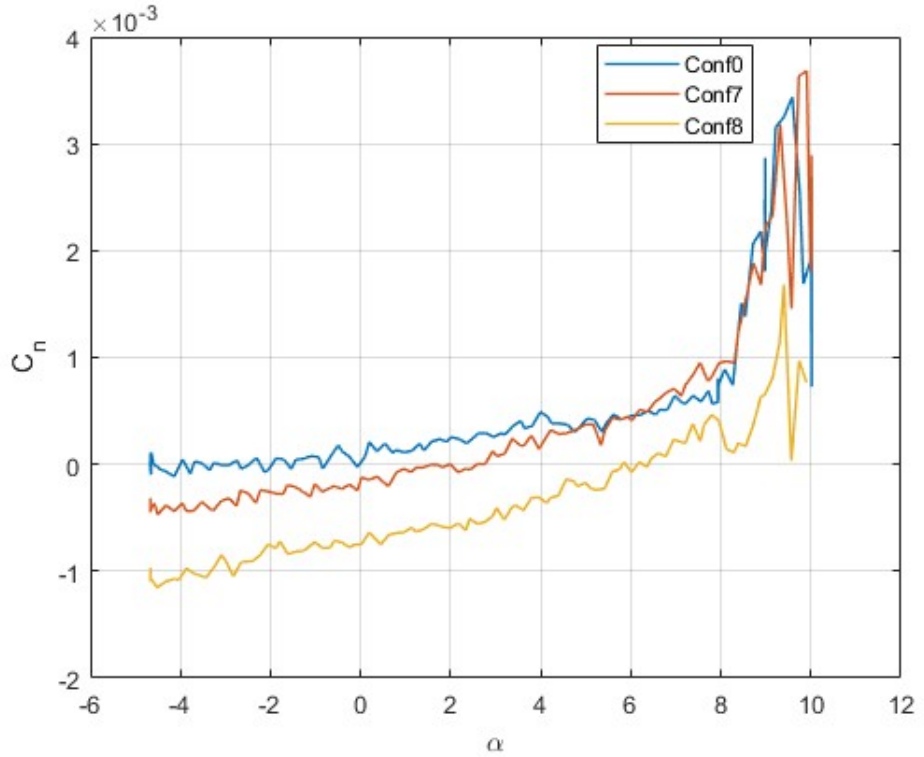

Figure 6.27: C_n vs α - Effect of aileron

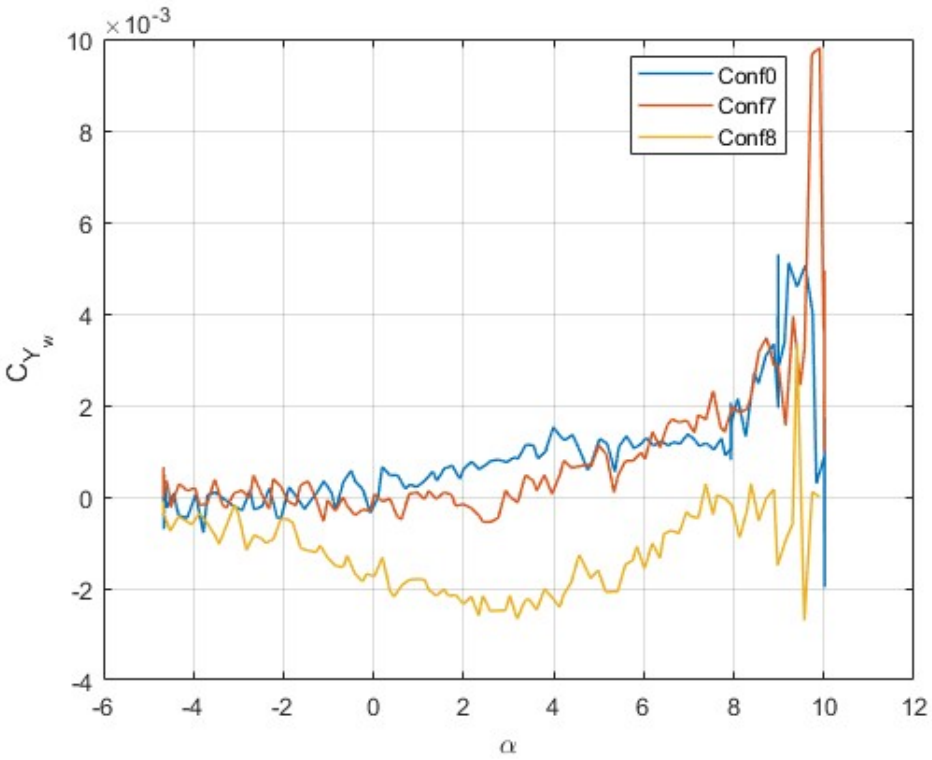

Figure 6.28: C_{Y_w} vs α - Effect of aileron

In both figures 6.27 and 6.28, since the values of the coefficient are quite small, high values of the coefficient caused by vibrations at high AOA are captured.

6.4.4 Effect of rudder/elevon

Configurations 5 and 6 feature only the right side aileron up, 5° and 10° degrees respectively, and these configurations were used to explore a possible use as a yaw control configurations since the Green Raven does not feature any rudder or other vertical control surface.

In figure 6.29 and 6.30, the rolling and yawing moment coefficients vs α at $\beta = 0°$ are illustrated. From these two images, it's possible to see that the rolling coefficient presents a considerable increment with respect to configuration 0 while the change in yawing moment for the different configurations is limited. At high AOA substantial fluctuations in the data are caused by the considerable amount of vibration of the model. In figure 6.31, 6.32 and 6.33 a comparison of the rolling, yawing, and side force coefficient vs β for configuration 0,5 and 6 at the different AOA tested is presented. Here, we can see that overall the values of the coefficient and the slope of the curves exhibit a modest variation.

From the data gathered it's evident that using a single horizontal control surface at the wing extremities to perform yaw control isn't a feasible solution for this UAV. The change in C_n is hardly detectable while the C_l presents a considerable variation, meaning that with configurations 5 and 6 we are generating a rolling motion instead of yaw control, hence completely missing the scope of the configuration. In chapter 7 an alternative to how the rudder function can be carried out is discussed.

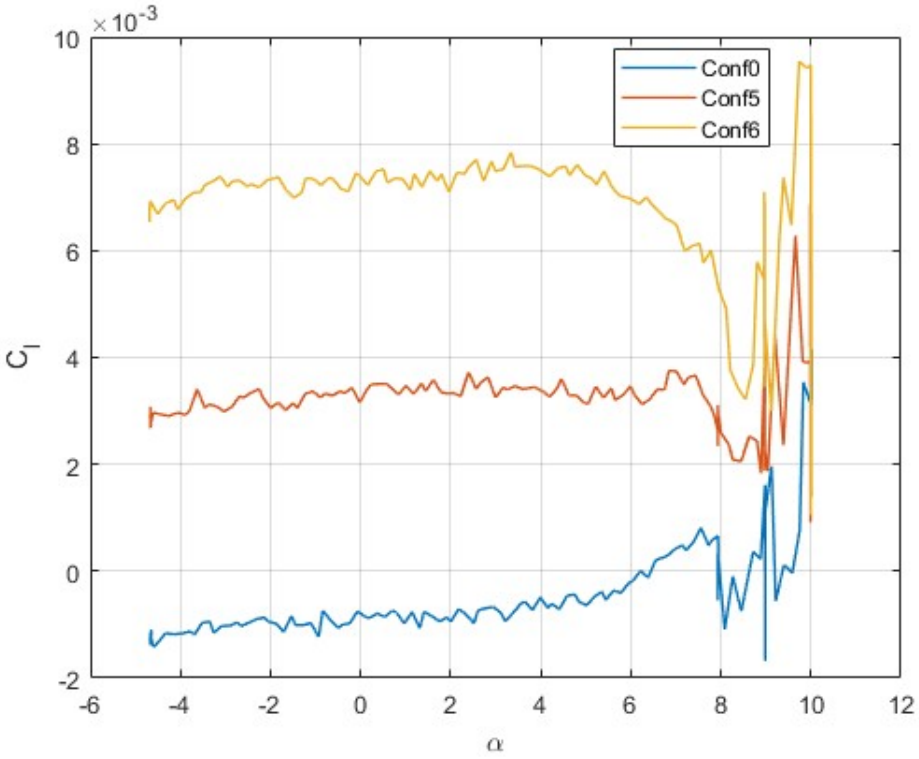

Figure 6.29: C_l vs α - Rudder effect $\beta = 0°$

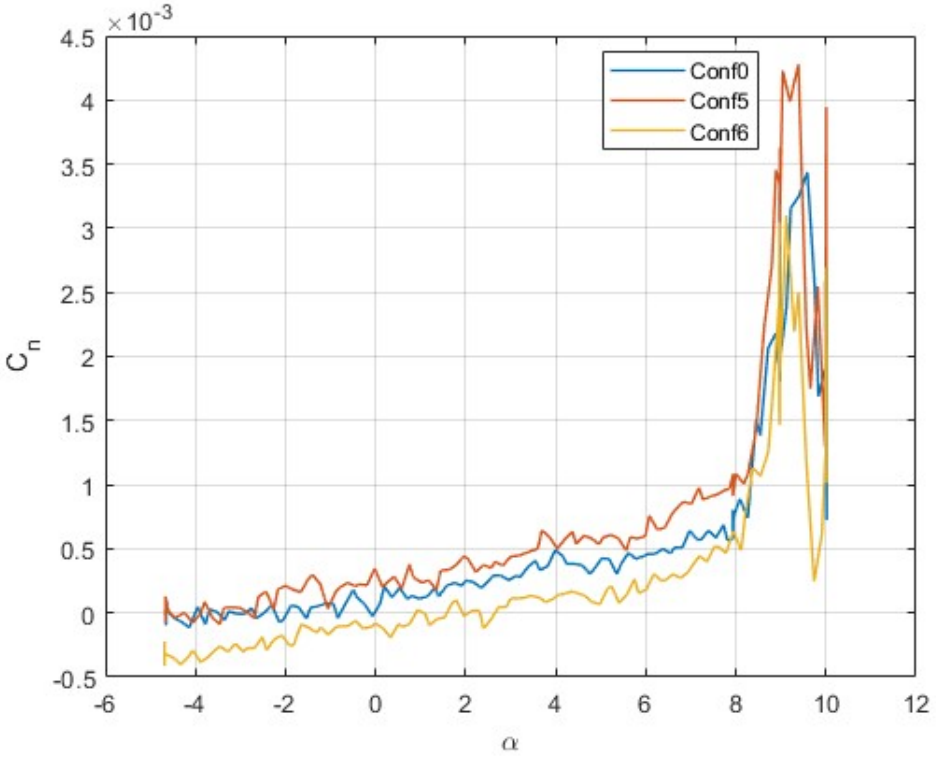

Figure 6.30: C_n vs α - Rudder effect $\beta = 0°$

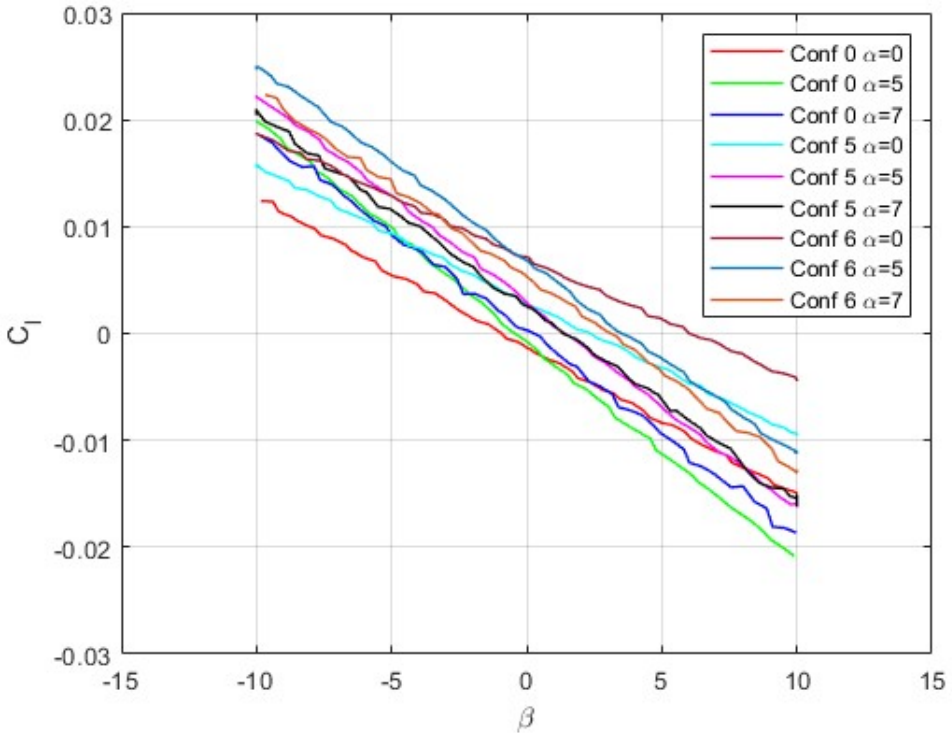

Figure 6.31: C_n vs β - Rudder effect

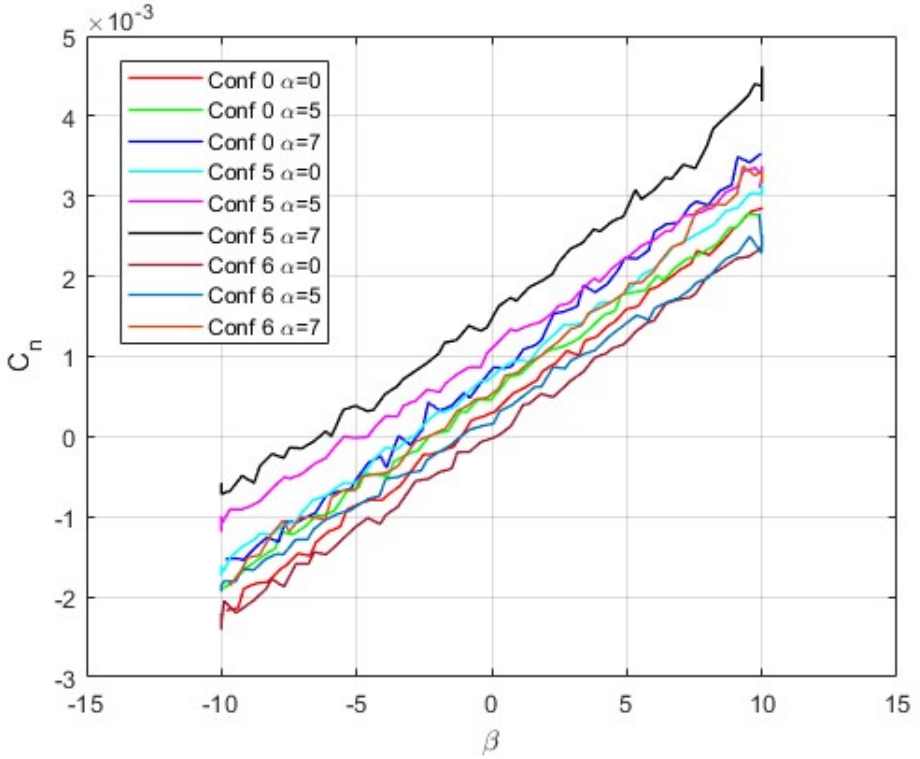

Figure 6.32: C_n vs β -Rudder effect

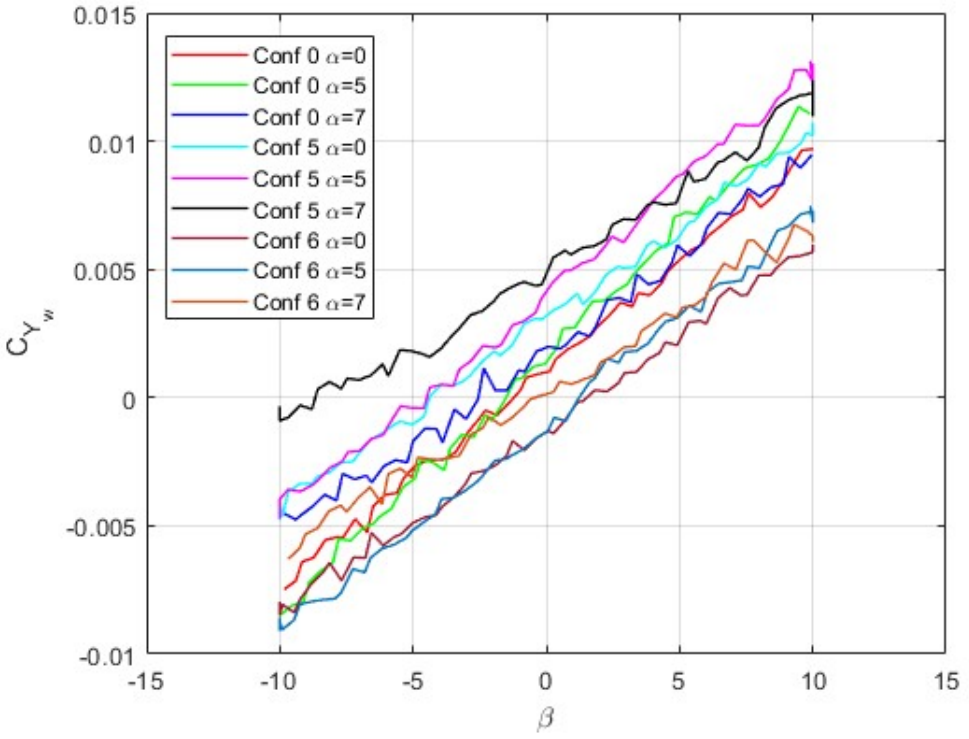

Figure 6.33: C_n vs β - Rudder effect

Chapter 7

Conclusions

Wind tunnel tests were performed to study the aerodynamic and stability characteristics of the Green Raven UAV. For this purpose, a 37.5% scaled model was designed and assembled using 3D-printed nylon and aluminum parts. A modular design with replaceable parts on the wings allowed us to perform tests in different configurations, while also being able to expand the test possibilities by developing new parts for the same model.

To properly evaluate the data collected via the wind tunnel tests, a study on the main wind tunnel correction methods has been carried out and correction factors for blockage, downwash, and flow angularity were calculated and used to improve the quality of the experimental data collected. Following this process, a comparison between the corrected and uncorrected data highlights the discrepancies and the change in the aerodynamic characteristics of the UAV.

Using the corrected data from the various configurations, a preliminary analysis of the aerodynamic and stability performances was carried out, focusing on obtaining the aerodynamic coefficients for the cruise configuration (configuration 0) and understanding the effects of the control surface chosen for the others. The conditions for obtaining lateral-directional static stability were met using the aerodynamic coefficient of the cruise configuration, while for longitudinal static stability, a negative C_{m_0} was obtained, resulting in an unbalanced flight at cruise AOA. Regarding the other configurations, tests on configurations 1,2,3 and 4 focused on evaluating the effect of different flap placements on the lift and drag, which resulted in configuration 2 (inboard flaps at 10°) being the best performing one when an increment of lift without sacrificing aerodynamic efficiency is needed, while configuration 4 (midboard flaps at 10°) is the best one when the maximum amount of lift is needed. Configurations 7 and 8 were utilized to investigate aileron effects and how they affect roll control. A comparison with configuration 0 allowed for the determination of their effectiveness and the amount of aileron adverse yaw generated, resulting in a noticeable amount of rolling moment generated with a slight amount of adverse yaw, most notably with configuration 8, as well as the effect of wing stall on the control surface. Configurations 5 and 6 were used to investigate their possible use as yaw control, but from the data extracted it resulted that using a single horizontal control surface at the wing extremities isn't a viable option.

7.1 Future developments and recommendation

Since with this test campaign only a preliminary analysis was completed, several areas can be further explored. Firstly, more tests with the baseline configuration are needed to properly investigate the stalling behavior of the model, either by using trip strips on the wings or by performing α sweeps till higher AOA, with the latter option needing a structural assessment of the model to be sure that the loads of tests at higher α angles can be withstood without issues by both the internal balance and the model itself. Another area to investigate is the possibility of using flaps as both lifting augmenting devices and elevators for pitch control. For this purpose new flap parts need to be designed to have a surface that can move both upwards and downward, and evaluate their impact with α sweeps using both surfaces in the inboard and midboard sections, to verify which one would be better for that specific use, and obtain δ_e aerodynamic derivatives. Flap effectiveness as lift augmenting devices can be further studied by testing configurations with both the inboard and midboard flaps engaged at different angles, to evaluate if their interaction can be useful as a more efficient way to generate lift instead of limiting their use as one surface at a time.

About the aerodynamic performances, one of the main topics that need to be addressed is the fact that a negative C_{m_0} is obtained, thus a balanced flight at cruise AOA isn't achieved. There can be various explanations, such as a mistake in the design phase that may require a slight redesign, but for this particular case, the most probable cause for the negative C_{m_0} is the impact of the model support on the accuracy of the data gathered in the wind tunnel. Horsten [17] extensively described the impact of support interference and methods to correct the results to consider support effects. Some key aspects to consider are the geometrical characteristics of the support, the positioning concerning the model as mentioned by Veldhuis [33], and the incoming flow conditions of support and model. Also, a wind tunnel test campaign was conducted by Mariani et al. [34] along with a CFD analysis in which the experimental setup was replicated to evaluate support interference effects. Results for the C_m vs α curves obtained from the CFD are comparable to those obtained in this work, with the same scale wind tunnel model, and when applying the support corrections, a positive value of C_{m_0} was obtained. Aside from the support correction that would need to be evaluated in the future, another factor that may influence the results obtained is the fact that the geometry of the WT model was changed to accommodate the rear sting connected to the balance by realizing a lid that covered the sting, hence changing how the flow interacts with the body with a possible repercussion of the pitching moment.

The second important topic that needs further investigation is how to perform yaw control since the solution tested couldn't provide satisfactory performance. Different alternatives are available, and the first distinction that can be made is whether to use vertical control surfaces or not. A vertical control surface could be positioned in different places on the aircraft, two approaches were previously highlighted in the literature review, as Vicroy et al. [25] tested a BWB model featuring two slightly inclined vertical tails with ruddervators positioned in the central part of the body, while Gryte et al. [26] performed tests on a model presenting vertical wing tips that could be equipped with moving control surfaces. The other approach

would be not to use any vertical control surface and only use horizontal ones, figuring out a combination of available or new control surfaces that can be moved together to generate a yawing moment. Sizing and placement of the eventual vertical tail or new horizontal control surface are key aspects since they are required to provide enough control on the UAV while also maintaining adequate aerodynamic efficiency, which is one of the core characteristics of a BWB architecture.

One more area that would benefit from improvement is the precision of the data gathered utilizing the wind tunnel. Measures of the longitudinal pressure gradient inside the tunnel and side-to-side angularity effects would provide additional data to perform sidewash and buoyancy corrections on the raw data collected. Also, with the correction method employed, as described in chapter 3, the procedure to obtain factors such as τ_1 and K_1 uses a pre-existing database generated for a traditional configuration aircraft, and for this study, it was adapted by considering the BWB model of the Green Raven as a wing. This procedure however is not ideal, since the flow develops differently around a blended-wing body, thus different values of correction factors may be used to improve the preciseness of corrections.

Appendix A

Flow angularity in L2000 wind tunnel

A.1 Test setup

As mentioned in section 3.7, additional tests can be made in order to evaluate the angularity of the flow inside the wind tunnel and the upwash or downwash effects on the aerodynamic coefficients. Following the procedure described by Pope et al. tests with a basic geometry aircraft model were carried out both in a regular and inverted flight configuration. The test setup is the exact same as the one described in chapter 5, with the only difference being the aircraft model used. The aircraft model features a standard configuration with a cylindrical fuselage and swept-back wings, with a conical nose and no tail section. It's made out of aluminum, and the wings feature a laminar airfoil. The basic geometry specification of the model is summarized in the following table:

Wing span	$1.5\,m$
Wing area	$0.198\,m^2$
Reference chord	$0.144\,m$

Table A.1: Geometry values

In figure A.1 the model used and the test setup is illustrated.

Figure A.1: Flow angularity test setup

In order to perform the inverted flight tests, both the model and the balance mounted inside it were rotated 180° and fixed to the same sting as the upright flight configuration.

A.2 Test matrix

To properly investigate the influence and amount of flow angularity and to develop a basic database, testing with the two configurations was performed at many different speeds, increasing air speed until overload difficulties on the mass balance or structural concerns on the model emerged. A critical detail that is highlighted by table A.2, is that for the inverted configuration, the angle had to be reversed since the mass balance inside the model is flipped with it, hence the measured angle of attack is the opposite as the one needed for the test.

Configuration	Test details
Upright	- α sweep from $-8°$ to $10°$ at $\beta = 0°$ at s u=10,15,20,25,30,35,40 m/s
Inverted	- α sweep from $8°$ to $-10°$ at $\beta = 0°$ at u=10,15,20,25,30,35,40 m/s

Table A.2: Test matrix - Flow angularity study

For this same reason, rotation of the forces and moments measured is needed in order to perform the comparison with the upright configuration and it's done by using the Euler angles equations.

A.3 Euler angle equations

Following the procedure described by Pope/barlow et al for a wind tunnel setup with roll angle ϕ at zero, considering θ and ψ respectively the pitch and yaw angle, the general relationship between body reference and wind reference forces is illustrated in equation A.1

$$\begin{bmatrix} A_{x_b} \\ A_{y_b} \\ A_{z_b} \end{bmatrix} = \begin{bmatrix} cos\theta\, cos\psi & sin\psi\, cos\theta & -sin\theta \\ sin\psi & cos\psi & 0 \\ sin\theta\, cos\psi & sin\theta\, sin\psi & cos\theta \end{bmatrix} \begin{bmatrix} A_{x_w} \\ A_{y_w} \\ A_{z_w} \end{bmatrix} \tag{A.1}$$

The forces convention for the test setup used is illustrated in the following equation:

$$\begin{bmatrix} A_{x_b} \\ A_{y_b} \\ A_{z_b} \end{bmatrix} = \begin{bmatrix} -T \\ -Y_b \\ -N \end{bmatrix} and \begin{bmatrix} A_{x_w} \\ A_{y_w} \\ A_{z_w} \end{bmatrix} = \begin{bmatrix} -D \\ -Y_w \\ -L \end{bmatrix} \tag{A.2}$$

Using A.2 in A.1 we obtain the equation used for converting body axis forces components to wind axis:

$$\begin{bmatrix} D \\ Y_w \\ L \end{bmatrix} = \begin{bmatrix} T\, cos\theta\, cos\psi\ +\ Y_b\, sin\psi\, cos\theta\ +\ N\, sin\theta\, cos\psi \\ T\, sin\psi cos\psi\ +\ Y_b cos\psi\ +\ N\, sin\theta\, sin\psi \\ -T\, sin\theta\ +\ cos\theta \end{bmatrix} \tag{A.3}$$

Considering the inverted configuration, since both the balance and the model are rotated 180°, the forces convention for the wind axis references changes as follows:

$$\begin{bmatrix} A_{x_w} \\ A_{y_w} \\ A_{z_w} \end{bmatrix} = \begin{bmatrix} -D \\ Y_w \\ L \end{bmatrix} \tag{A.4}$$

Thus the equation to obtain wind axis forces components from body forces is:

$$\begin{bmatrix} D \\ Y_w \\ L \end{bmatrix} = \begin{bmatrix} T\, cos\theta\, cos\psi\ +\ Y_b\, sin\psi\, cos\theta\ +\ N\, sin\theta\, cos\psi \\ -\,T\, sin\psi cos\psi\ C_b cos\psi\ -\ N\, sin\theta\, sin\psi \\ T\, sin\theta\ -\ cos\theta \end{bmatrix} \tag{A.5}$$

A.4 Corrections evaluation procedure

The misalignment correction, meaning correction values for both the angle of attack α and the drag coefficient, is usually obtained in the data reduction, as described in this section. Regarding the AOA correction values $\Delta\alpha$, it may be obtained by plotting inverted and upright values of C_L vs α, as shown in figure A.2

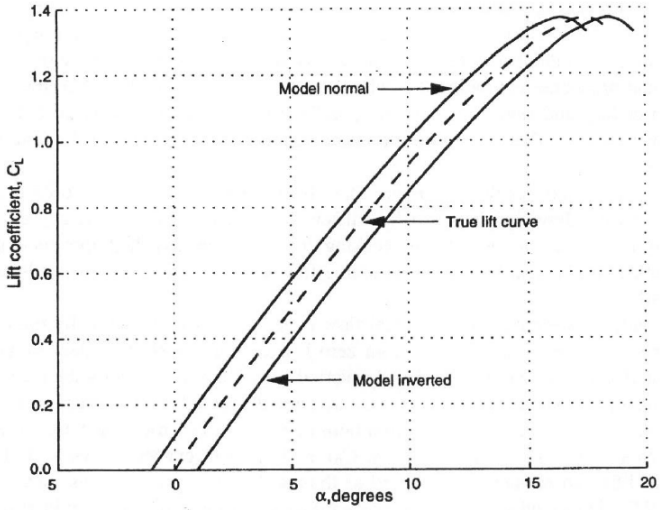

FIGURE 7.21 Upright and inverted C_L versus a curves.

Figure A.2: Upright and inverted C_L - α curves

for each value of C_L, $\Delta\alpha$ can be obtained as

$$\Delta\alpha = (\alpha_{inv} - \alpha_{up})/2 \tag{A.6}$$

Presuming that the polars of inverted and normal runs are similar to those illustrated in figure A.3, considering the wing in the upright position, the balance reading is:

$$C_{D,indicated} = C_{D,true} - C_{L,indicated}(tan\,\alpha_{up}) \tag{A.7}$$

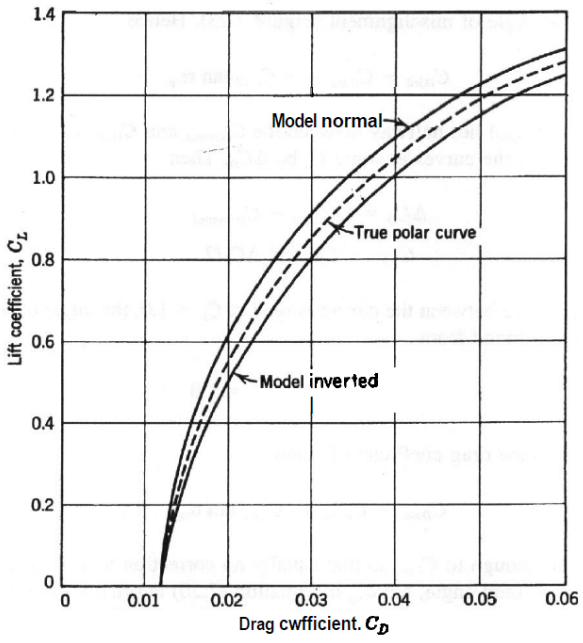

FIGURE 722 Drag polar, C_L versus C_D.

Figure A.3: Upright and inverted drag polar, C_L vs C_D

In which α_{up} is the misalignment angle. Thus, it's possible to write

$$C_{D,ind} - C_{D,true} = -C_{L,ind}(tan\,\alpha_{up}) \tag{A.8}$$

The correct value of $C_{D,true}$ is halfway between $C_{D,upright}$ and $C_{D,inverted}$ curves. Considering ΔC_D the difference between the curves at a given value of C_L, then we have:

$$\Delta C_D = C_{D,upright} - C_{D,inverted} \tag{A.9}$$

$$C_{D,ind} - C_{D,true} = \Delta C_D/2 \tag{A.10}$$

Supposing that the difference ΔC_D is read at $C_L = 1$, then the misalignment angle α_{up} can be obtained by

$$tan(\alpha_{up}) = (\Delta C_D/2)_{C_L} = 1 \tag{A.11}$$

The corrected value of C_D is then obtained as

$$C_{D,true} = C_{D,ind} + C_{L,ind}(tan\,\alpha_{up}) \tag{A.12}$$

Since the values of $C_{D,ind}$ and $C_{L,ind}$ depends o the model being tested, the parameter of interst that will be used to obtain the real value of the drag coefficient of the Green Raven model is $tan\,\alpha_{up}$. In the case of α being a small angle, then $tan\,\alpha$ in equation A.11 can be replaced with the value of the angle expressed in radians. Another approach to this problem is, instead of calculating $tan\,\alpha_{up}$ in A.7 at one single value of C_L such as 1, evaluate ΔC_D at several values of C_L and graph ΔC_D or $\Delta C_D/2$ against C_L and then use a linear curve or apply a linear regression to evaluate the slope, which is the desired $tan\,\alpha$. Based on the data available, this second approach was used, and correction values for the different speeds were obtained.

A.5 Results

Before applying the procedure described in the previous section, it's necessary to consider just the linear portion of the curves to collect reliable data. In figure A.4 the exiperimental data curves C_L vs α are illustrated, while in figure A.5 only the linear portion is considered.

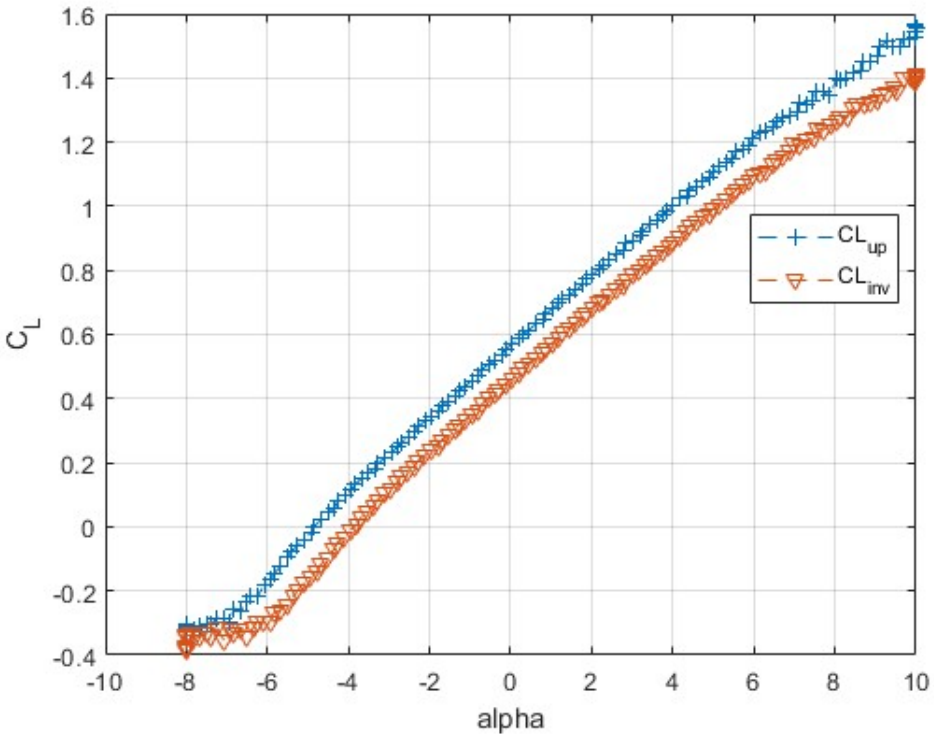

Figure A.4: Upright and inverted C_L - α experimental curves - u=35m/s

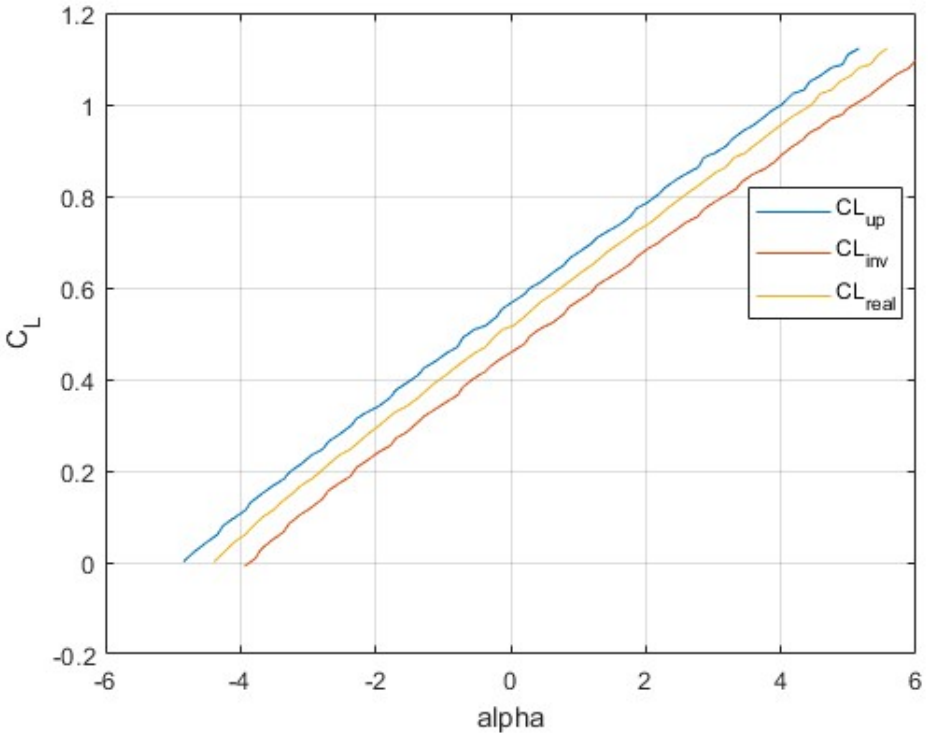

Figure A.5: C_L - α curves - linear portion only - u=35m/s

Using equation A.6 for each value of C_L and then taking the average value, a

certain $\Delta\alpha$ for each test speed is calculated. The results obtained are summarized in table A.3, while in figure A.5 the true C_L vs α curve is included.

Air speed [m/s]	$\Delta\alpha$ [deg]
10	0.287
15	0.381
20	0.421
25	0.493
30	0.473
35	0.426
40	0.498

Table A.3: Average value of $\Delta\alpha$

As for drag coefficient correction, following the second approach described in the previous section, the next plot of ΔC_D vs C_L is obtained:

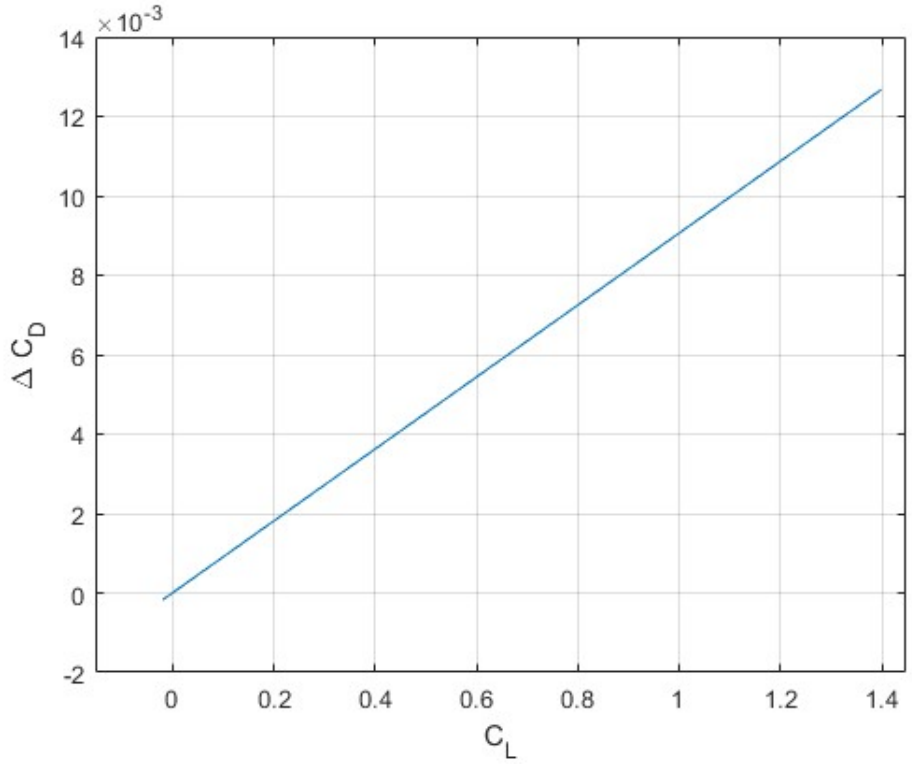

Figure A.6: ΔC_D - C_L curve - u=35m/s

The slope of the curve in figure is the desired value of $tan\,\alpha$, and in table A.4 the values calculated for the different air speeds are summarized

Air speed [m/s]	$tan\,\alpha$
10	0.01
15	0.0117
20	0.0189
25	0.00923
30	0.009
35	0.0091
40	0.0097

Table A.4: $tan\,\alpha$ values at different speeds

Bibliography

[1] W. Nicolas, “Aircraft”, September 1921

[2] C. Fetting, “THE EUROPEAN GREEN DEAL”,

[3] Gray Creech, “X-48 Research All good things must come to an end”, April 2013, Section: Armstrong Flight Research Center

[4] J. J. Berton and W. J. Haller, “A Noise and Emissions Assessment of the N3-X Transport”, National Harbor, MD, January 2014. NTRS Author Affiliations: NASA Glenn Research Center NTRS Report/Patent Number: E-18841-1 NTRS Document ID: 20150006703 NTRS Research Center: Glenn Research Center (GRC)

[5] H. Kim and M.-S. Liou, “Flow Simulation of N3-X Hybrid Wing-Body Configuration”, Grapevine, TX, January 2013. NTRS Author Affiliations: Science Applications International Corp., NASA Glenn Research Center NTRS Report/-Patent Number: AIAA Paper 2013-0221 NTRS Document ID: 20130003337 NTRS Research Center: Glenn Research Center (GRC)

[6] H. Kim and M.-S. Liou, “Optimal Shape Design of Mail-Slot Nacelle on N3-X Hybrid Wing Body Configuration”, 31st AIAA Applied Aerodynamics Conference, San Diego, CA, June 2013, DOI 10.2514/6.2013-2413

[7] M.-S. Liou, H. Kim, and M.-F. Liou, “Challenges and Progress in Aerodynamic Design of Hybrid Wingbody Aircraft with Embedded Engines”, Tech. Rep. E-18869, June 2016. NTRS Author Affiliations: NASA Glenn Research Center, Science Applications International Corp. NTRS Document ID: 20160007898 NTRS Research Center: Glenn Research Center (GRC)

[8] S. Suewatanakul, A. Porcarelli, A. Olsson, H. Grimler, A. Chiche, R. Mariani, and G. Lindbergh, “Conceptual Design of a Hybrid Hydrogen Fuel Cell/Battery Blended-Wing-Body Unmanned Aerial VehicleâAn Overview”, Aerospace, vol. 9, no. 5, 2022, p. 275. Publisher: MDPI

[9] Bernard Etkin and Lloyd Duff Reid, “Dynamics of Flight: Stability and Control”, 3rd edition ed., October 1995, ISBN: 978-0-471-03418-6

[10] W. T. Eckert, K. W. Mort, and J. Jope, “Aerodynamic design guidelines and computer program for estimation of subsonic wind tunnel performance”, tech. rep., 1976

[11] BRYAN, G.H., “Stability in aviation: an introduction to dynamic stability as applied to the motions of aeroplanes”, 1911

[12] Jewel B. Barlow, William H. Rae, Jr., and Alan Pope, “Low Speed Wind Tunnel Testing”, third edition ed.

[13] Patrick Ralph Ashill, Travis Binion, Kevin Russell Cooper, Roger Crites, Joel L. Everhart, Bernd F.R. Ewald, J. E. Hackett, Hartmut Holst, Alexander J. Krynytzky, Norman D. Malmuth, Miroslav Mokry, Perry A. Newman, William

L. Sickles, Frank William Steinle, Jr., Cyril Richard Taylor, and Nigel John Taylor, "Wind Tunnel Wall Corrections - AGARD AG-336", tech. rep., October 1998

[14] John Andreson, "Fundamentals of Aerodynamics", sixth edition ed., 2017, ISBN: 978-1-259-12991-9

[15] A. U. Haque, W. Asrar, A. A. Omar, E. Sulaeman, and M. J. Ali, "Comparison of data correction methods for blockage effects in semispan wing model testing", EPJ Web of Conferences, 2016, p. 02129

[16] H. Glauert, "Wind Tunnel Interference on0 Wings, Bodies and Airserews 0", 1933

[17] B.J.C. Horsten, "Low-Speed Model Support Interference", 2011, ISBN: 978-90-8891-294-8

[18] X. Vaucheret, "Vortex Lattice Code for Computation of any Wind-Tunnel and Support Effects on Models", RECHERCHE AEROSPATIALE, no. 2, 1991, pp. 39–51. Publisher: DUNOD 15 RUE GOSSIN, 92543 MONTROUGE CEDEX, FRANCE

[19] C. QuÃ©mard, "Phase II Report of Garteur Action Group AD(AG06): Model Support Interference in Large Low-Speed Wind Tunnels", Technical Report TP-052, ONERA and Aerospatiale, March 1989

[20] S. Mouton, "Numerical investigations of model support interference in subsonic and transonic wind tunnels", ODAS 2007-8th ONERA-DLR Aerospace Symposium, 2007

[21] R. Liebeck, M. Page, and B. Rawdon, "Blended-wing-body subsonic commercial transport", 36th AIAA Aerospace Sciences Meeting and Exhibit, Reno,NV,U.S.A., January 1998, DOI 10.2514/6.1998-438

[22] W. Wisnoe, W. Kuntjoro, F. Mohamad, R. E. M. Nasir, N. F. Reduan, and Z. Ali, "Experimental results analysis for UiTM BWB baseline-I and baseline-II UAV running at 0.1 mach number", International Journal of Mechanics, vol. 4, no. 2, 2010, pp. 23–32

[23] W. Wisnoe, M. A. Zurriati, M. Firdaus, R. N. Fazira, R. E. Nasir, and W. Kuntjoro, "Experimental investigation of center elevator deflection on aerodynamics of UiTM's Baseline-I Blended Wing Body (BWB) unmanned aerial vehicle (UAV)", 2010 International Conference on Science and Social Research (CSSR 2010), 2010, pp. 108–112

[24] W. Wisnoe, R. E. M. Nasir, W. Kuntjoro, and A. M. I. Mamat, "Wind tunnel experiments and CFD analysis of Blended Wing Body (BWB) Unmanned Aerial Vehicle (UAV) at mach 0.1 and mach 0.3", International conference on aerospace sciences and aviation technology, 2009, pp. 1–15. Issue: AEROSPACE SCIENCES & AVIATION TECHNOLOGY, ASAT-13, May 26â28, 2009

[25] D. D. Vicroy, E. D. Dickey, N. Princen, and M. Beyar, "Overview of Low-speed Aerodynamic Tests on a 5.75% Scale Blended-Wing-Body Twin Jet Configuration (Invited)", 54th AIAA Aerospace Sciences Meeting, San Diego, California, USA, January 2016, DOI 10.2514/6.2016-0009

[26] K. Gryte, R. Hann, M. Alam, J. RohÃ¡Ä, T. A. Johansen, and T. I. Fossen, "Aerodynamic modeling of the Skywalker X8 Fixed-Wing Unmanned Aerial Vehicle", 2018 International Conference on Unmanned Aircraft Systems (ICUAS), June 2018, pp. 826–835, DOI 10.1109/ICUAS.2018.8453370.

ISSN: 2575-7296

[27] D. Raymer, "Aircraft Design: A Conceptual Approach, Fifth Edition", American Institute of Aeronautics and Astronautics, Inc., August 2012, ISBN: 978-1-60086-911-2

[28] M. Drela, "XFOIL: An Analysis and Design System for Low Reynolds Number Airfoils", Low Reynolds Number Aerodynamics (C. A. Brebbia, S. A. Orszag, J. H. Seinfeld, P. Spanos, A. S. Cakmak, P. Silvester, C. S. Desai, G. Pinder, R. McCrory, S. Yip, F. A. Leckie, A. R. S. Ponter, K.-P. Holz, K.-J. Bathe, J. Connor, W. Wunderlich, J. Argyris, and T. J. Mueller, eds.), vol. 54, pp. 1–12, Berlin, Heidelberg: Springer Berlin Heidelberg, 1989, DOI 10.1007/978-3-642-84010-4_1. Series Title: Lecture Notes in Engineering

[29] R. A. McDonald and J. R. Gloudemans, "Open Vehicle Sketch Pad: An Open Source Parametric Geometry and Analysis Tool for Conceptual Aircraft Design", AIAA SCITECH 2022 Forum, San Diego, CA & Virtual, January 2022, DOI 10.2514/6.2022-0004

[30] "xflr5: http://www.xflr5.tech/xflr5.htm,"

[31] Aviation Technology Experimental Institute, "Wind tunnel Balance Manual", December 1986

[32] E. Maskell, "A theory of blockage effects on bluff bodies and stalled wings in a closed wind tunnel, Royal Aircraft Establishment, Paper No", 1963

[33] L. L. M. Veldhuis, "Support Interference Effects of a Ventral Sting on a Body of Revolution. A Brief Description of Phase 1", tech. rep., Technical Report LSW 89-2, Delft University of Technology, Department of â¦, 1988

[34] R. Mariani, S. Suewatanakul, S. Ghika, L. A. Penela, P. Wennhage, and B. Zang, "WIND TUNNEL TEST OF A BLENDED WING BODY UNMANNED AERIAL VEHICLE", 33rd Congress of the International Council of the Aeronautical Sciences, ICAS 2022, Stockholm, Sweden, Sep 4 2022-Sep 9 2022, 2022, pp. 2711–2721